מכון ויצמן למדע

WEIZMANN INSTITUTE OF SCIENCE

עבודת גמר (תזה) לתואר

דוקטור לפילוסופיה

מוגשת למועצה המדעית של
מכון ויצמן למדע
רחובות, ישראל

מאת

יהונתן דלאל

מנחה:

ד"ר רועי עוזרי

אדר ב', תשע"ד

Thesis for the degree

Doctor of Philosophy

Submitted to the Scientific Council of the
Weizmann Institute of Science
Rehovot, Israel

By

Yehonatan Dallal

Advisor:

Dr. Roee Ozeri

March 2014

ספקטרוסקופיה של אטומים קרים לכודים במלכודת קוואזי-אלקטרוסטטית

Spectroscopy of Quasi-Electrostatically Trapped Cold Atoms

תקציר

לימוד של תדרי המעברים בין רמות אנרגיה שונות של אלקטרונים באטום היווה כלי חשוב בפיסיקה אטומית, מאז שהוכר התחום כשדה מחקר נפרד. ניתן ללמוד רבות על מבנה האטום מתוך השוואה של תדרי מעבר כפי שנמדדו בניסוי, לערכם כפי שנובא על יד התיאוריה. באופן מסורתי, לצורך מדידה ספקטרוקופית של מעברים באטום, משתמשים בגז דליל של אטומים חופשיים, וזאת משום שבניגוד לאטומים לכודים, אלה אינם סובלים מהרחבה או הזזה של הקווים הספקטרלים כתוצאה מאינטראקציות בין האטומים, או כתופעת לוואי של המלכודת.

בחיבור זה אתאר את תכנונה ובנייתה של מערכת ניסיונית לקירורם ולכידתם של אטומי רובידיום וכיצד השתמשתי בה לצורך מדידות ספקרוסקופיות של אטומי רובידיום 87 קרים. ליצירת המלכודת השתמשתי בקרן ממוקדת של לייזר CO_2 אשר אורך גל שלו נמצא בתחום הקוואזי-אלקטרוסטטי ביחס למעברי הדיפול באטום. אסביר כיצד ניתן לבצע ספקטרוסקופיה מדוייקת של תדרי המעבר באטום, למרות ההרחבות האי-הומוגניות במלכודת ואיבוד הקוהרנטיות כתוצאה מכך. אמשיך בתאורה של מדידה ספקטרוסקופית מדוייקת, בשיטתו של רמזי, של הסחת תדר השעון ברובידיום הנובעת מהחלק הטנזורי של הקיטוביות הדיפרנציאלית בין המצבים ההיפר-עדינים של מצב היסוד של האטום, תופעה שגודלה $4x10^{-7}$ ביחס לתדר השעון, שהינו בתחום המיקרוגל, כ 6.8 גה"צ. בניסוי נפרד השתמשתי במעבר בתחום האופטי כדי למדוד את השפעתו של השדה החשמלי של הלייזר המשמש ללכידה על המעבר D2. לבסוף אציג שיטה ספקרוסקופית למדידה של שינויים איטיים בכיוונו של השדה המגנטי, תוך שימוש באטומים הלכודים עצמם כחיישנים. מדידה זו עושה שימוש במעבר שבאופן רגיל אינו רגיש לשינויים בשדות מגנטים וכך ניתן לבצע מדידה בקבועי-זמן איטיים, מבלי לאבד את הקוהרנטיות.

Abstract

Study of the transition frequencies between different energy levels of electrons in atoms has been an important tool of atomic physics ever since the advent of the field. Much can be learned about structure of atoms by comparing the measured transition frequencies to theoretical predictions. Traditionally, spectroscopy was performed on dilute samples of free atoms; a notable examples in the fountain atomic clock; since they do not exhibit inhomogeneous broadening of spectroscopic features arising from a trapping potential or their interactions.

In this work I describe the design and the construction of an apparatus to cool and quasi-electrostatically trap atoms, using the slowly varying electric field of a focused CO_2 laser beam, and how it was used to perform spectroscopic measurements on trapped samples of cold Rubidium 87 atoms. I demonstrate that it is possible to precisely measure the transition frequency even in the presence of inhomogeneous broadening and decoherence, caused by the trapping potential, and then concentrate on a precision measurement of the shift resulting from the tensor part of the of the hyperfine clock transition polarizability in the ground electronic state of the ^{87}Rb atom using Ramsey spectroscopy. This effect is on order $4\text{x}10^{-7}$ compared with the micro-wave clock transition frequency of approximately 6.8GHz. In a separate experiment I utilized an optical transition to measure the effect of the trapping field on the D2 line. Finally, a spectroscopic method to measure slow drifts in the magnetic field, using the trapped atoms as sensitive probes, is presented. This method makes use of a magnetic insensitive transition and thus measurements in slow time scales can be made, without loss of coherence.

Gali, my love, this work is dedicated to you.

Without your love, support and encouragement I could never have done this.

Thank you.

Acknowledgments

The five years I have devoted to this project, and altogether more than seven years spent in the Weizmann Institute of Science, have been the most significant in my life. The Institute, or simply "Weizmann", as it is called by all, is truly a wonderful place. The serene surroundings on one hand, and the lively discussions with faculty and students on the other, makes for a truly spacial environment to do science in. During my time here, many advances has taken place, both in my professional and scientific life, and much more importantly, in my personal life. My three wonderful children, six, four and a year and a half old, were all born during this time. Professionally, this Ph.D project was a great experience. By confronting the many technological and conceptual challenges that are an indivisible part of constructing such a complicated experimental apparatus, I learned a lot about myself and my abilities. Indeed, in doing a Ph.D, you find yourself in the unique position of being both the person setting the goals, and the one in charge of achieving them. Really, there isn't a boss more strict than oneself.

I would like to acknowledge the support I got from many friends and colleagues during my PhD year, both directly in helping with their knowledge and expertise, or morally, in the more frustrating moments during the "great vacuum overhaul", as this dark period will be known in written history.

I have first met Dr. Roee Ozeri, my Ph.D. supervisor, almost seven years ago and was immediately taken by his enthusiasm, his sense of purpose and his vision. Roee, a true optimist, has guided me throughout this project by good advice and encouragement, always hearing my side and never withholding his thoughts. I would also like to thank the members of my Ph.D. committee, Prof. Nir Davidson and Dr. Edvardas Narevicius who provided with invaluable counseling. I would like to thank Nir for the many hours he devoted to discussing with me various aspects of the project from the design of the vacuum system and choice of trapping laser, to the more obscure properties of the polarizability tensor.

I also want to thank my colleagues, Ziv Meir, Nitzan Akerman, Shlomi Kotler,Yinnon Glickman and Ido Almog for their helping hand in times of need. Thanks to Oren Raz for not being afraid of tensors, You helped me put it all in order. Thank you, my many

friends in the "corridor", you have made those coffee breaks longer and more numerous than they should have been! Many ideas that have sprouted over a cup of coffee, later found their way into the lab.

In the course of my work I was greatly assisted by the wonderful people of the Weizmann Institute, each expert in his own field. My vacuum work was immensely helped by Yigal Shachar, Dr. Michael Rappaport and most importantly, Dr. Rostyslav Baron, whose helping hand was generously offered, and accepted, many times. I am grateful to Yeruham Shimoni, for helping with the electronics, to Yossi Drier for making it possible to work by keeping the computers alive, and for Yossi Shopen, David Leibovitz, Gershon Elazar, Benjamin Sharon and Guy Hun from the mechanics workshop for helping my ideas become solid objects. Thanks go also to our department administrative stuff, Israel Gonen, Rachel Goldman and Perla Zalcberg for their hard workings in the background, without which the normal ongoing in the department would have gone to a complete standstill.

Finally, I would like to thank my family, my parents Galia and Eli, my sisters Orly and Livnat and above all my wife Gali and my children. Thank you for believing in me, for supporting me in the good and hard times, and for the sacrifices you have made to allow me to devote myself to this work. Thank you.

Contents

1 Ph.D. chronicles

This project has started with the goal of creating an experimental system in which the interactions between ultracold Rubidium atoms and cold ions, trapped together in the same volume, can be studied. Few experiments with similar goals exist, with the most notable progress in this field achieved by groups led by Johannes Denschlag in Ulm [41, 42] and Michel Köhl in Bonn [52, 53]. At an early enough stage we have realized that the best way to advance this project is to divide the building of the system into two parts - a "neutral" chamber designed to trap and cool Rubidium (and Strontium, at a later stage) atoms and an "ion" chamber that will include an RF Paul trap for the trapping and cooling of ions. Up until the point when the two chambers were to be connected, and an "hybrid" system created, the two parts were to be treated as two separate experiments, each capable of producing meaningful data, with the limitation that the design of each system cannot be individually optimized, but rather the restrictions and constraints forced by a future integrated system must be taken into account.

The neutral system was designed as a fairly standard single chamber cold atoms machine, relying on fast evaporation in a CO_2 laser quasi electrostatic trap [6, 8, 14]. The CO_2 laser operates at a wavelength of 10.6μm, long compared with commonly used trap lasers that operate close to 1μm. Thanks to this relatively large wavelength, a single, tightly focused beam is enough to create a true three dimensional trap, in contrast with comparable setups that use shorter wavelength trapping lasers (e.g. NdYAG with its 1.06μm wavelength) that usually require a crossed beam geometry for tight 3D confinement. This choice was made with the hope that the system would be simple and robust to operate (hopes that were indeed realized), but at the cost of more complex vacuum design, necessitating the use of a large, stainless steel vacuum cell and the incorporation of ZnSe viewports transparent to 10μm radiation. The original vacuum system, first operational in June 2010, was cursed with low trap lifetimes due to bad vacuum conditions. After about a year of trying to get the most out of the system we decided to take it down for maintenance. Several viewports and the two flexible intra-vacuum lens mounts were discovered to be leaky, a very high failure rate indeed, the reason for it remains unknown. During this down time the system was redesigned and many components were replaced. The vacuum

pump was replaced by a larger one and vacuum conductance to the main chamber was improved. The system returned to operation during April 2012, finally with good vacuum performance: a Bayerd-Alpert vacuum gauge gave a reading close to 10^{-10}torr and atoms trapped in the QUEST have over 30s of lifetime. A short time after the resurrection of the "neutral" system, the "ion" setup came to life by the hard work of Ziv Meir, a fellow PhD student. He has designed and built a separate vacuum system, managed to capture and cool $^{88}Sr^{+}$ ions and performed some independent experiments with his trapped ions. On December 2013 we have finally reached a common goal and connected the two experimental vacuum systems together. After a successful bakeout we plan to begin the joint operations, starting with implementing an optical escalator beam to transport the cold atoms from the neutral part of the system to the science chamber containing the ion trap. We hope that soon we will be the first to observe interactions between cold ^{87}Rb atoms and trapped $^{88}Sr^{+}$.

Realizing that an operational integrated system could not be realized within the remaining time of my PhD, I had to make a tough decision and concentrate on measurements that can be done using the neutral system alone. Having experimented briefly with microwave spectroscopy of my trapped atoms, I noticed that the clock transition at 6,834,682,610.904290 Hz, was shifted to the red by an amount proportional to the trap power. This shift could not be solely related to the slightly different detuning of the trapping laser from the F=1 and F=2 electronic ground states, in contrast with the situation for atoms trapped by a closer to resonance laser e.g. a NdYAG with its 1μm wavelength [26]. With the trapping laser frequency being only $1/13$ of the frequency of the closest transition at 795nm, the laser field can be treated as a DC field and the potential arises from the DC polarizability of the ground state of the Rb atoms. To zeroth order the polarizability of the two hyperfine states of the $l = 0$ ground state should be the same since the electronic configuration is the same. However, the slightly different spatial wavefuntions of the F=1 and F=2 ground states (arising from the hyperfine interaction) gives rise to a well known *differential* polarizability between the two states [4]. This differential polarizability can in principle be measured by measuring the shift of the clock transition in a known electric field. In addition, there is another effect, two orders of magnitude smaller than the "scalar differential polarizability" discussed above called the "tensor differential

polarizability" [37, 11]. This effect has to do with the relative direction of the electric and magnetic fields on the atom. Both of these properties of the ^{87}Rb atom can be measured using the strong electric fields applied at the focus of our trapping laser.

This is the first time, to the best of our knowledge, that the scalar and tensor differential polarizability of an alkali atom have been measured by using trapped atoms, rather than atomic beam or fountain methods. Moreover, this is the first time that the ratio of tensor to scalar shifts of the clock transition has been measured for Rubidium. The dual use of a QUEST, both as a means to trap the atoms and as a method to apply large electric fields that induces the shift to be measured is also novel.

The thesis is organized as follows, in section 2 an overview containing most of the theory related to the operation of the experimental system and the experiments that follows, is given. Section 3 describes the experimental setup that was designed and built as part of this work, and also experimental methods that were developed and used in our experiments. Section 4 describes in details the measurement of the tensor part of the ground state differential polarizability. Section 5 deals with laser spectroscopy of the light shift of the S-P transition, experienced by atoms trapped in our quasi-electrostatic trap. In section 6 discuss and demonstrate the effect of changing the quantization axis during a spectroscopic measurement. We continue by describing the possibility of using microwave (MW) spectroscopy on the magnetic insensitive clock transition of optically trapped ^{87}Rb atoms, for measuring slowly evolving magnetic fields. Section 7 is dedicated to conclusions and insights arising from this work, and some future prospects are suggested.

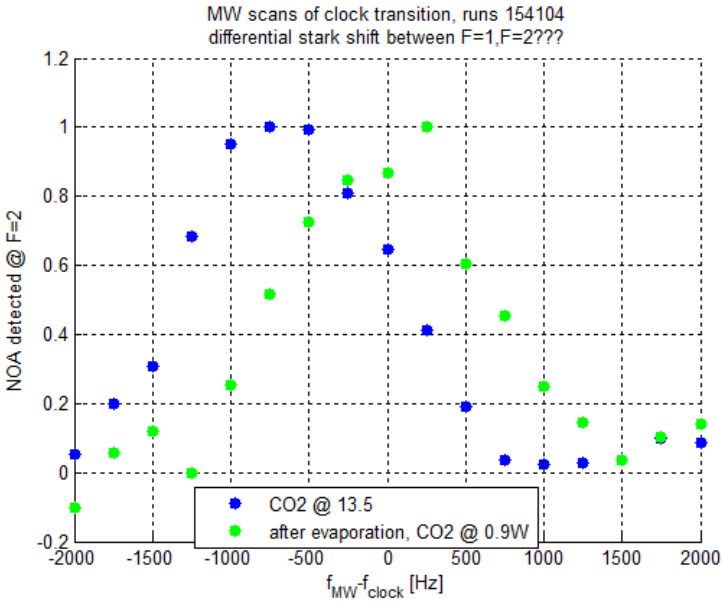

Figure 1: first appearance of the diff pol

2 Overview

This thesis touches upon several aspects of the polarizability of the Rubidium atom. Firstly, it is the polarizability of the ground state of the atoms that enables them to be trapped by the local high-intensity field of a focused CO_2 laser beam, and by measuring some properties of the trap we can deduce the polarizability. Secondly, it is the difference between the polarizabilities of the excited and ground states that causes a shift of the trapped atoms optical transitions. This shift was measured by a spin relaxation method and was also used to enhance the loading of the trap by optically-pumping trapped atoms into a hyperfine state that is out of resonance with the cooling light resulting in a reduction of light-assisted lossy collisions. Thirdly, the polarizability of the two hyperfine states belonging to the ground-state manifold is different, causing a frequency shift and a broadening of the microwave transition between the hyperfine states. We performed Rabi and Ramsey spectroscopy on the hyperfine clock transition and were able to measure this shift with a resolution of below 1Hz. Finally, the differential polarizability of the ground state has a tensorial part and this causes the transition frequency to depend on the rela-

tive directions of the electric field and the quantizing magnetic field. We have measured the *ratio* between the scalar and tensor parts of the ground state polarizability with a precision of 10%.

This section serves to bring the different subjects mentioned above into the context of this work. I introduce the leading actor, the Rubidium atom, and briefly discuss the trapping mechanism and energy distributions of trapped atoms, that will become relevant later in interpreting the results from various spectroscopic measurements that were performed. I discuss the concept of microwave spectroscopy utilizing the hyperfine transition and mention two important experimental methods, that of Isidor Isaac Rabi and of Norman Ramsey. I finish by discussing the subject of polarizability in more detail, discussing some of its subtleties.

2.1 The rubidium atom

Rubidium is an alkali metal, found in the first column of the periodic table. With an atomic number of 37 it has one valance electron that determines its chemical properties. Rubidium has two naturally occurring isotopes, ^{87}Rb and ^{85}Rb, both of which are bosons, with abundances 28% and 72%. While both isotopes are widely used in cold atoms and other atomic physics experiments (maybe owing to the accessibility of its 780nm cooling transition using cheap diode lasers), ^{87}Rb has a special role as the secondary atomic clock standard and thus many of its properties, such as the frequency of its hyperfine transition or its polarizability, have been thoroughly studied and tabulated [47].

The electronic ground state of ^{87}Rb is $5\mathrm{S}_{\frac{1}{2}}$ ($|n, L, J\rangle = \left|5, 1, \frac{1}{2}\right\rangle$). Owing to the fine-structure interaction, the P orbital ($L = 1$) is split to $P_{\frac{1}{2}}$ and $P_{\frac{3}{2}}$ and the D line of the $S \to P$ transition is split to $D1$ and $D2$ lines, at 795nm and 780nm respectively. ^{87}Rb also has a non-zero nuclear magnetic moment $I = \frac{3}{2}$, resulting in hyperfine interaction and splitting of each of the levels such that the total angular momentum $\mathbf{F} = \mathbf{I} + \mathbf{J}$ can take any of the values in the range $|I - J| \leq F \leq |I + J|$. The ground state is therefore split to $F = 1$ and $F = 2$ hyperfine states with energy difference of $\Delta E_{HF} \approx h \times$ 6.834GHz (the "clock" transition frequency). The $P_{\frac{3}{2}}$ excited state is split to $F' = 0, 1, 2, 3$. The D2 line is used for laser cooling thanks to the availability of its, closed transition;

$F = 2 \rightarrow F' = 3$. The degeneracy of $2F + 1$ levels in each hyperfine manifold may be lifted by an application of a magnetic field, and to lowest order the Zeeman splitting is $\Delta E_{F,m_F} = \mu_B g_F m_F B_z$, a splitting of 700kHz/G for the ground states. The magnetic insensitive transition $|F = 1, m = 0\rangle \rightarrow |F = 2, m = 0\rangle$ is sometimes referred to as the "clock" transition, similarly to the respective transition in Cs (on which the SI second is defined). While the clock transition is insensitive to magnetic fields to first order, there is a small (compared to the first order Zeeman shift of the $m \neq 0$ states) second order Zeeman shift (Breit-Rabi shift) of $575.15\text{Hz}/G^2$ so a deviation of 1Hz in the clock transition frequency is caused by a relatively large field of ≈ 42mG, allowing for an accurate clock even when operating in a noisy magnetic field environment. While the primary atomic clock standard (and hence the definition of the second) utilizes the Cs atom, the ^{87}Rb atom is widely used as a secondary standard. Due to a coincidence between the ^{85}Rb and ^{87}Rb D1 lines at 795nm, ^{87}Rb clocks allow for a simple implementation and relatively compact and inexpensive clocks, making them quite popular. In the simplest implementation light emitted from a rubidium discharge lamp is first filtered by a vapor of ^{85}Rb and then used to optically pump ^{87}Rb to the F=2 ground state. A microwave field at the clock transition frequency will repopulate the F=1 ground state and cause a decrease in the transmission of the optical pumping light through the cell. This is used as a signal to correct the frequency of the MW generator. The ^{87}Rb clock can be found in many applications, a short list of these includes GPS satellites and cellular communication base-stations. In a cold-atom implementation of an atomic clock (e.g. a fountain clock) ^{87}Rb has some advantage compared to Cs, as its density shift is some 20 times lower, allowing for an increase in signal quality by use of denser clouds of atoms without a compromise in clock accuracy, and smaller fluctuations in clock frequency due to density fluctuations **[17, 19, 12]**, these being limiting factors for current day Cesium fountain clocks.

2.2 Alkali atoms in static and quasi-static electric fields

When placing an atom in a weak electric field (such that its response is in the linear regime) the initially symmetric electron charge distribution is perturbed by the field. For an alkali atom we can get an order of magnitude estimation for the polarizability as there

is only one valance electron to consider and a naive treatment may still give some intuition. Treating the system of nucleus-electron simply as a bound particle, we can approximate the system as an harmonic oscillator, given that the perturbation from the equilibrium is small: the returning force is proportional to the displacement $\mathbf{r}$ by a spring constant k: $\mathbf{F} = -k\mathbf{r}$. The addition of an external force $-e\mathbf{E}$ shifts the equilibrium position by $\mathbf{r} = -\frac{e}{k}\mathbf{E}$. A dipole

$$\mathbf{d} = -e\mathbf{r} = \frac{e^2}{k}\mathbf{E} \equiv \alpha\mathbf{E}$$

is induced by the field. The interaction energy of a dipole with a the field is $U = -\mathbf{d}\cdot\mathbf{E}$, however, this is an induced dipole, not a permanent one and the energy is given by the work done to create the dipole, completely analogous to the energy stored in a spring

$$U = -\alpha\int_0^E E'dE' = -\frac{1}{2}\alpha E^2. \tag{1}$$

For an alkali atom, its simple electronic structure allows the spring constant to be related to the the oscillation frequency of the S-P transition (D1 line) by $k = m_e\omega_0^2$, and we can get the simple expression for the polarizability $\alpha = \frac{e^2}{m_e\omega_0^2}$. For the Rubidium atoms, the numerical value of this expression is surprisingly close (within 10%) to the empirically measured polarizability. The form of the interaction potential (1) suggests a possibility for trapping - the energy will have a local minimum where the electric field $|E|$ is at a maximum. However, by Ernshaw's theorem, no such maximum exists for static fields in a charge free region of space. It is nevertheless possible to create a region where the amplitude of an oscillating field is maximal, e.g. a focused beam of laser radiation. It is therefore interesting to consider the response to a sinusoidally varying field.

The equation of motion for a damped harmonic oscillator

$$\ddot{x} + \Gamma_\omega\dot{x} + \omega_0^2 x = -eE(t)/m_e$$

where $\Gamma_\omega = \frac{e^2\omega^2}{6\pi\epsilon_0 c^3 m_e} = \frac{\omega^2}{\omega_0^2}\Gamma$ is the classical damping rate due to radiative decay, a good approximation for alkali atoms **[16]**, and Γ corresponds to the finite excited state lifetime. Finding the response to a complex oscillating field $E(t) = \varepsilon e^{-i\omega t}$ is equivalent to Fourier

transforming the equation of motion we obtain $-\omega^2\hat{x} - i\omega\Gamma_\omega\hat{x} + \omega_0^2\hat{x} = -e\varepsilon/m_e$ then $\hat{d}(\omega) = -e\hat{x}(\omega) = \frac{e^2}{m_e\omega_0^2}\frac{\omega_0^2}{\omega_0^2-\omega^2-i\Gamma\omega}\varepsilon$. We identify the frequency dependent polarizability

$$\alpha(\omega) = \alpha_{static}\frac{\omega_0^2}{\omega_0^2 - \omega^2 - i\omega\Gamma_\omega} = \alpha_{static}A(\omega)e^{i\phi(\omega)}.$$

The field in the lab is of course real $E(t) = \varepsilon e^{-i\omega t} + \varepsilon^* e^{i\omega t}$ and the real dipole is

$$d(t) = \alpha\varepsilon e^{-i\omega t} + \alpha^*\varepsilon^* e^{i\omega t} = \alpha_{static}A(\omega)\left(\varepsilon e^{-i(\omega t-\phi(\omega))} + \varepsilon^* e^{-i(\omega t-\phi(\omega))}\right).$$

For low enough drive frequencies, $\omega \ll \omega_0$, the relative phase between the driving field and the induced dipole, $\phi(\omega) \approx \arctan\frac{\omega\Gamma_\omega}{\omega_0^2}$, is very small ($\approx 10^{-9}$rad for CO_2 and ^{87}Rb) meaning that the induced dipole does not significantly lag behind the driving field. For the frequency of a CO_2 laser operating at 10.6μm the ratio $\frac{\omega_0}{\omega} \approx 13$ and the polarizability approaches its static value making it an extremely good approximation to treat the field as static, hence such optical traps are commonly referred to as as quasi-electrostatic traps or in short, QUEST. More generally, the dipole potential is related to the real part of the polarizability $U_{dip} = -\frac{1}{2}\Re\{\alpha\}E^2$, while the imaginary part (of negligible magnitude for $\omega \ll \omega_0$) results in dissipation, or spontaneous photon scattering, the rate of which is negligible for all practical purposes, at this drive frequency. A somewhat fuller treatment can be found in **[16, 49]**.

2.3 the CO_2 laser trap

The potential induced by the laser is proportional to the intensity $U(\mathbf{r}) \propto -I(\mathbf{r}) \propto -E^2$ and for a purely Gaussian trapping beam, and neglecting gravity is given by [7]

$$U = -\frac{U_0}{1+\left(\frac{z}{z_r}\right)^2}\exp\left(-2\frac{r^2}{w_0^2\left(1+\left(\frac{z}{z_r}\right)^2\right)}\right)$$

where z is along the beam k vector, r is the transverse direction in cylindrical coordinates, w_0 is the waist at the focus, $z_r = \pi\frac{w_0^2}{\lambda}$ is the Rayleigh range for the Gaussian beam.

$$U_0 = -\frac{1}{2}\alpha_s E_{rms}^2 = -\frac{1}{2}\alpha_s \frac{I_0}{\epsilon_0 c}$$

is the trap depth, where α_s is the electrostatic polarizability of the ground state of Rb, ϵ_0 is the vacuum permittivity and c the speed of light, E_{rms} is the square root time averaged electric field of the laser field and $I_0 = \frac{2P}{\pi w_0^2}$ is the laser intensity at the center, assuming a Gaussian beam of total power P and waist w_0. The trap frequencies can be obtained by expanding the potential to second order around its minimum:

$$\begin{aligned} U(r,z) &\approx -U_0\left(1-\left(\frac{z^2}{z_r^2}\right)\right)\left(1-\left(2\frac{r^2}{w_0^2}\right)\right) \approx -U_0 + \frac{U_0}{z_r^2}z^2 + \frac{2U_0}{w_0^2}r^2 \\ &\approx -U_0 + \frac{U_0}{z_r^2}z^2 + \frac{2U_0}{w_0^2}r^2 = -U_0 + \frac{1}{2}m\omega_z^2 z^2 + \frac{1}{2}m\omega_r^2 r^2. \end{aligned}$$

For a trap formed using a single Gaussian beam we therefore arrive at:

$$\omega_r = \sqrt{\frac{4U_0}{mw_0^2}} = 2\frac{1}{w_0^2}\sqrt{\frac{\alpha_s P}{\pi m\epsilon_0 c}} \propto \frac{\sqrt{P}}{w_0^2}$$

for oscillations in the radial directions and

$$\omega_z = \sqrt{\frac{2U_0}{mz_r^2}} = \frac{\lambda}{\pi w_0^3}\sqrt{\frac{2\alpha_s P}{\pi m\epsilon_0 c}} \propto \frac{\sqrt{P}}{w_0^3}$$

for the axial oscillation frequency. From the relation between the Rayleigh range and the waist $z_r = \pi\frac{w_0^2}{\lambda}$ we can get a simple relation connecting the radial and axial trapping frequencies and the asymptotic angle of divergence θ :

$$\frac{\omega_r}{\omega_z} = \sqrt{2}\frac{z_r}{w_0} = \sqrt{2}\pi\frac{w_0}{\lambda} = \frac{\sqrt{2}}{\theta}. \tag{2}$$

For a $10\,\mu$m laser it is therefore possible to get both a large trapping region and three dimensional trapping, using only a single focused beam: focusing to $w_0 = 30\mu$m the ratio

between the two oscillation frequencies is $\frac{\omega_r}{\omega_z} \approx 12$, as compared to an anisotropy factor of 120 for the same waist with a 1μm laser, meaning that for the shorter wavelength laser there is practically no axial trapping at the same value of w_0, moreover, to obtain similar proportions between the axial and radial trapping a 1μm trapping laser will have to be focused to a mere 3μm waist, severely reducing the trap volume. Of-course, larger traps can be obtained with 1μm lasers, but this usually requires two or more beams intersecting at their waist, thus complicating the experimental setup.

2.3.1 Derived quantities: collision rate, phase space density

Assuming the temperature of the trapped atoms is much lower than the depth, $kT \ll U_o$, the atoms are confined to the bottom of the trap, which may then be approximated as harmonic. The Hamiltonian for a non-interacting gas in a harmonic trap is

$$\mathcal{H} = \frac{\mathbf{p}^2}{2m} + \frac{1}{2}m\omega_x^2 x^2 + \frac{1}{2}m\omega_y^2 y^2 + \frac{1}{2}m\omega_z^2 z^2.$$

The (unnormalized) distribution of momentum and position in phase space is $f(\vec{p},\vec{r}) = exp\left(-\frac{1}{kT}\mathcal{H}(\vec{p},\vec{r})\right)$. The partition function is given by

$$\mathcal{Z} = h^{-3}\int d^3p d^3r\, f(\vec{p},\vec{r}) = \frac{(2\pi kT)^3}{h^3\omega_x\omega_y\omega_z} = \left(\frac{kT}{\hbar\bar{\omega}}\right)^3$$

and the probability to find a particle at a point $(\vec{p},\vec{r})$ in phase space is given by

$$P(\vec{p},\vec{r}) = \frac{f(\vec{p},\vec{r})}{\mathcal{Z}} d^3p d^3r.$$

The probability to find a particle at point $\vec{r}$ is obtained by integrating out the all momenta and is equal to

$$P(\vec{r}) = \left(\frac{m\bar{\omega}^2}{2\pi kT}\right)^{3/2} e^{-\frac{1}{2kT}m\left(\sum\omega_i^2 x_i^2\right)} d^3r.$$

hence a cloud of harmonically trapped thermal atoms has a Gaussian shape.

Before continuing, the validity of the harmonic approximation should be checked. We compare the extent of the thermal cloud in the radial and axial directions to the beam waist w_0 and Rayleigh range z_r. We have for the rms widths of the cloud $\sigma_{r,z}^2 = \frac{kT}{m\omega_{r,z}^2}$. Plugging in the oscillation frequencies from above we get $\sigma_r^2 = \frac{kT}{4U_0}w_0^2$ and $\sigma_z^2 = \frac{kT}{2U_0}z_r^2$, so a cold cloud with $kT \ll U_0$ is limited to a region much smaller than the beam waist or Rayleigh range. For a typical $\frac{kT}{U_0} \approx 10$ (typical values are $T \approx 30\mu$K and potential depth $U_0 \approx 300\mu$K) we find that $\sigma_r \approx 0.16 w_o$. At this typical distance from the beam focus (trap minimum), the softening of the spring constant ($F_{HO} = -\frac{d}{dx}U(x) = -\frac{4U_0}{w_0^2}xe^{-2x^2/w_0^2} = (-kx)\,e^{-2x^2/w_0^2}$), compared with the harmonic potential at the trap bottom, is only about 5%, making the harmonic approximation excellent at this temperature range.

The local density $n(\vec{r})$ may be defined by $N = \int d\vec{r} n(\vec{r})$ where N is the number of trapped atoms. This implies simply $n(\vec{r}) = NP(\vec{r})$. The average density is $\bar{n} = \int d\vec{r} P(\vec{r}) n(\vec{r}) = 2^{-3/2} n_0$ where

$$n_0 = N\left(\frac{m\bar{\omega}^2}{2\pi kT}\right)^{3/2}$$

is the peak density at the center of the trap. An effective volume for the trapped cloud may be defined as $V = {}^{N}/_{\bar{n}} = 2^{3/2}\left(\frac{2\pi kT}{m\bar{\omega}^2}\right)^{3/2}$.

The phase space density (PSD) is defined as $\rho_{PSD} = \lambda_{dB}^3 n$ where $\lambda_{dB} = \frac{h}{\sqrt{2\pi mkT}}$ is the thermal de-Broglie wavelength. Plugging in the relevant expressions we get

$$\rho_{PSD} = N\left(\frac{\hbar\bar{\omega}}{kT}\right)^3 = \frac{N}{\mathcal{Z}}$$

at the trap center.

The rate of collisions between the trapped atoms is given by $\Gamma_{col} = (\frac{4}{\sqrt{3\pi}})\sigma_s \bar{n} v_{th}$ where $\sigma_s \approx 5.4 \times 10^{-12}\,\mathrm{cm}^2$ [31] is the s-wave scattering cross section for elastic collisions between Rb atoms and $v_{th} = \sqrt{\frac{3kT}{m}}$ is the thermal velocity. The numerical factor $\frac{4}{\sqrt{3\pi}}$ is due to the fact that it is the relative average thermal velocity that is relevant here **[29]**. Plugging in the expressions for v_{th} and n we arrive at $\Gamma_{col} = (\frac{\sqrt{2}}{\pi^2})N\sigma_s m\frac{\omega^3}{kT}$, the collision rate is inversely proportional to the temperature and proportional to the trap frequency cubed. Typical numbers for a trap with oscillation frequencies $\omega_r = 2\pi \times 1400$Hz, $\omega_z = 2\pi \times 110$Hz holding $100,000$ atoms at 30μK, are $\rho_{PSD} \approx 10^{-4}$, $n_0 \approx 2 \times 10^{12}\mathrm{cm}^{-3}$ and $\Gamma_{col} \approx 130\mathrm{s}^{-1}$,

at the trap center.

2.4 Energy distributions in a harmonic trap

It is generally true that different levels experience different shifts when an electric field is applied. When the transition frequency between two such levels is interrogated, a shift of the transition frequency is observed when compared with the transition frequency of free atoms, unaffected by the fields. In an optical trap it is the local variation of the electric shift that is responsible to the trapping, and so different atoms, that sample the trap differently, will also experience different shifts, that are directly related to their potential energy in the trap. The distribution of potential energies is therefore mapped onto a distribution of shifts in the different transitions we measure. In this section we arrive at simple expressions for the distribution of instantaneous potential energies and of the average potential energy of non interacting atoms in an harmonic trap.

When the temperature of the trapped atoms is low compared with the trap depth, the atoms only sample the bottom of the trap and the trapping potential may be approximated as harmonic. For a dilute enough gas the interactions are negligible and simple expressions can be derived for the energy distribution of the trapped atoms. We begin with a 1D harmonic oscillator (HO) with the Hamiltonian $H = \frac{p^2}{2m} + \frac{1}{2}m\omega^2 x^2$. For a HO with total energy E, $E = \frac{p^2}{2m} + \frac{1}{2}m\omega^2 x^2 \Rightarrow 1 = \frac{p^2}{2mE} + \frac{m\omega^2 x^2}{2E}$. This is just the equation of an ellipse in phase space $(\frac{x}{a})^2 + (\frac{y}{b})^2 = 1$ and the area is $A = \pi ab$, where $a = \sqrt{2mE}$ and $b = \sqrt{\frac{2E}{m\omega^2}}$ so $A = 2\pi\frac{E}{\omega}$. The number of states upto energy E is $N = A/h = \frac{E}{\hbar\omega}$, as could be obtained directly. For a three dimensional HO, $N = \left(\frac{E}{\hbar\bar{\omega}}\right)^3$ where $\bar{\omega} = \sqrt[3]{\omega_x\omega_y\omega_z}$. The density of states is therefore given by,

$$\mathcal{D}(E) = \frac{3E^2}{\hbar^3\bar{\omega}^3} \sim E^2,$$

a well known result. We want to calculate the energy distribution for trapped atoms at a

temperature T. The partition function is

$$\begin{aligned}\mathcal{Z} &= \int_0^\infty dE\mathcal{D}(E)e^{-\frac{E}{k_BT}} = \frac{3}{\hbar^3\bar{\omega}^3}\int_0^\infty dEE^2e^{-\frac{E}{k_BT}} = \\ &= \frac{3}{\hbar^3\bar{\omega}^3}\frac{d^2}{d\beta^2}\int_0^\infty dEe^{-\beta E} = \frac{3}{\hbar^3\bar{\omega}^3}\frac{d^2}{d\beta^2}\frac{1}{\beta} = 6\left(\frac{k_BT}{\hbar\bar{\omega}}\right)^3.\end{aligned}$$

The probability density to find an atom with an energy E is given by **[26]**

$$\rho(E) = \frac{1}{\mathcal{Z}}\mathcal{D}(E)e^{-\frac{E}{k_BT}} = \frac{1}{2}\frac{1}{k_B^3T^3}E^2e^{-\frac{E}{k_BT}}. \tag{3}$$

For a harmonic trap the virial theorem holds for the time averages of the kinetic and potential energies: $\langle E_k\rangle = \langle V\rangle$ and consequently $\langle V\rangle = \frac{1}{2}E$, leading to a distribution of *time average* potential energies of the trapped atoms, a relation that will be useful for the treatment of Ramsey spectroscopy later on:

$$\rho(\langle V\rangle) = \frac{2}{k_B^3T^3}\langle V\rangle^2 e^{-2\frac{\langle V\rangle}{k_BT}} \tag{4}$$

For the distribution of the instantaneous potential energies we again begin with the (classical) Hamiltonian for atoms trapped in a harmonic trap $\mathcal{H} = \frac{p_x^2}{2m} + \frac{p_y^2}{2m} + \frac{p_z^2}{2m} + \frac{1}{2}m\omega_x^2x^2 + \frac{1}{2}m\omega_z^2y^2 + \frac{1}{2}m\omega_z^2z^2$. The unnormalized distribution in phase space (The Boltzman factor) is $f(\mathbf{p},\mathbf{r}) = e^{-\frac{1}{k_BT}H(\mathbf{p},\mathbf{r})}$. For an harmonic potential the partition function is obtained by a simple Gaussian integration $\mathcal{Z} = \frac{1}{h^3}\int d^3p\int d^3xe^{-\frac{1}{k_BT}H(\mathbf{p},\mathbf{r})} = \frac{(k_BT/\hbar)^3}{\omega_x\omega_y\omega_z}$ and the normalized distribution is $p(\mathbf{p},\mathbf{r}) = \frac{1}{\mathcal{Z}}e^{-\frac{1}{k_BT}\mathcal{H}(\mathbf{p},\mathbf{r})}$. The distribution in space is obtained by integrating $\mathbf{p}$ out: the probability to find an atom in a region $dv = dxdydz$ around a coordinate (x,y,z) is $p(\mathbf{r}) = (\frac{m}{2\pi k_BT})^{3/2}\omega_x\omega_y\omega_z e^{-\frac{m}{2k_BT}(\omega_x^2x^2+\omega_y^2y^2+\omega_z^2z^2)}dxdydz$. To continue, we need the probability to find the atom with the potential in the interval $[0,V]$. It is the same as the probability to find the atoms inside the volume of an ellipsoid given by the implicit relation $V = \frac{1}{2}m\omega_x^2x^2 + \frac{1}{2}m\omega_z^2y^2 + \frac{1}{2}m\omega_z^2z^2$. The derivation can be made simpler by the transformation $\omega = \omega_x^{\frac{1}{3}}\omega_y^{\frac{1}{3}}\omega_z^{\frac{1}{3}}$, $\omega x' = \omega_x x$, $\omega y' = \omega_y y$, $\omega z' = \omega_z z$. Then $\omega^3dx'dy'dz' = \omega_x\omega_y\omega_z dxdydz$ and $V(\mathbf{r}') = \frac{1}{2}m\omega^2\mathbf{r'^2}$. The distribution becomes $p(\mathbf{r}')d^3r' = \left(\frac{m\omega^2}{2\pi k_BT}\right)^{3/2}e^{-\frac{m}{2k_BT}\omega^2\mathbf{r'^2}}4\pi r'^2dr'$, i.e. the probability for an atom to be found in

a region in space in which $V < V'$ is the same as the probability for it to be found with $r' < a' = \sqrt{\frac{2V'}{m\omega^2}}$:

$$P(V < V') = P(r' < a') = 4\pi \left(\frac{m\omega^2}{2\pi k_B T}\right)^{3/2} \int_0^{a'} e^{-\frac{m}{2k_B T}\omega^2 \mathbf{r'^2}} r'^2 dr' \tag{5}$$

the probability density function is obtained from this cumulative probability by differentiation $p(V) = \frac{d}{dV'}P(V < V') = \frac{da'}{dV'}\frac{d}{da'}P(r' < a')$. By the fundamental theorem of calculus $\frac{d}{dx}\int^x f(x')dx' = f(x)$. We also have $\frac{da'}{dV'} = \sqrt{\frac{1}{2m\omega^2 V'}}$ and wrapping everything up we get

$$p(V) = 2\pi^{-\frac{1}{2}}(k_B T)^{-3/2}\sqrt{V}e^{-\frac{V}{k_B T}}. \tag{6}$$

It is nice to observe that since the Hamiltonian is quadratic in both momentum and space, i.e. the kinetic energy $E_k = \frac{p^2}{2m}$ and the potential energy $V = \frac{1}{2}m\omega r^2$ has the exact same form, the distribution of kinetic energies in the trap is exactly the same

$$p(E_k) = 2\pi^{-\frac{1}{2}}(k_B T)^{-3/2}\sqrt{E_k}e^{-\frac{E_k}{k_B T}}.$$

Treating the kinetic and potential energies as independent random variables (true if the total energy is not constrained, and follows from the independence of $\mathbf{r}$ and $\mathbf{p}$) we can write the distribution of the total energy $E = E_k + V$. Using $p(E) = \int_0^E p(E_k = E - V)p(V)dV$ and the distributions for the kinetic and potential energies from above, we can write

$$\begin{aligned} p(E) &= 4\pi^{-1}(k_B T)^{-3}\int_0^E dV\sqrt{V}\sqrt{E-V}e^{-\frac{V}{k_B T}}e^{-\frac{E-V}{k_B T}} \\ &= 4\pi^{-1}(k_B T)^{-3}e^{-\frac{E}{k_B T}}\int_0^E dV\sqrt{V}\sqrt{E-V} \\ &= \frac{1}{2}(k_B T)^{-3}E^2 e^{-\frac{E}{k_B T}} \end{aligned} \tag{7}$$

which is exactly the distribution of energies, as it very well should be.

2.5 interaction with microwave field.

The Hamiltonian of a ground state atom in a static magnetic quantization field can be written in terms of the unperturbed states $|F, m\rangle$

$$\begin{aligned} H_0 &= \sum_{m=-1}^{1} \mu_B B_z g_{F=1} |F=1,m\rangle\langle F=1,m| + \\ &+ \sum_{m=-2}^{2} (\hbar\omega_{hf} + \mu_B g_{F=2} m B_z) |F=2,m\rangle\langle F=2,m| . \end{aligned}$$

Here ω_{hf} is the hyperfine transition frequency, g_F is the Lande giromagnetic ratio of the hyperfine manifold F and B_z is the magnitude of the quantizing magnetic field. We want to calculate the effect of a magnetic field oscillating at a frequency close to $\omega = \omega_{hf} + \delta$, with $\delta \ll \omega_{hf}$. In the most general form this oscillating MW field is elliptically polarized with $\hat{a}$ and $\hat{b}$ as the major and minor axes of the polarization ellipse and $\hat{a} \perp \hat{b}$: $\mathbf{B}_{mw} = \hat{a}B_1 \cos(\omega t) + \hat{b}B_2 \sin(\omega t)$. Since we want to look at transitions between the hyperfine manifolds it makes sense to write the interaction Hamiltonian in terms of the electronic spin and nucleus angular momentum $H_I = -\mu_B(g_S\mathbf{S} + g_I\mathbf{I}) \cdot \mathbf{B}_{mw}$. Using the appropriate Clebsch-Gordan coefficients we can write the $m = 0$ states of both hyperfine manifolds in terms of the eigenstates of $\mathbf{S}, \mathbf{I}$:

$$|F=1, m=0\rangle = \frac{1}{\sqrt{2}} \left| m_I = \frac{1}{2}, m_S = -\frac{1}{2} \right\rangle - \frac{1}{\sqrt{2}} \left| m_I = -\frac{1}{2}, m_S = \frac{1}{2} \right\rangle$$

$$|F=2, m=0\rangle = \frac{1}{\sqrt{2}} \left| m_I = \frac{1}{2}, m_S = -\frac{1}{2} \right\rangle + \frac{1}{\sqrt{2}} \left| m_I = -\frac{1}{2}, m_S = \frac{1}{2} \right\rangle .$$

We can now write the matrix element between the two magnetic insensitive states $\langle 2| H_I |1\rangle$ involved with the clock transition, where we use the shorthand notation $|1\rangle = |F=1, m=0\rangle$, $|2\rangle = |F=2, m=0\rangle$,

$$\langle 2| H_I |1\rangle = \frac{1}{2}(\left\langle \frac{1}{2}, -\frac{1}{2} \right| + \left\langle -\frac{1}{2}, \frac{1}{2} \right|) H_I (\left| \frac{1}{2}, -\frac{1}{2} \right\rangle - \left| -\frac{1}{2}, \frac{1}{2} \right\rangle).$$

Since there are only $\left|\pm\frac{1}{2},\mp\frac{1}{2}\right\rangle$ terms involved it is simple to see that only $\langle 2|\, S_z B_{mw,z}\,|1\rangle$ and $\langle 2|\, I_z B_{mw,z}\,|1\rangle$ do not vanish ($S_{x,y}$ and $I_{x,y}$ will create states that are out of this subset). $B_{mw,z}$ is the projection of the MW field on the quantization axis. We get

$$\langle 2|\, H_I\,|1\rangle = \frac{1}{2}\mu_B B_{mw,z}(g_S - g_I) \approx \frac{g_S \mu_B B_{mw,z}}{2} \approx \mu_B B_{mw,z}, \tag{8}$$

where $g_S \gg g_I$ and $g_S \approx 2$ are assumed. Generally

$$\begin{aligned} B_{mw,z} &= B_{mw}\hat{a}\cdot\hat{z}\cos(\omega t) + B_{mw}\hat{b}\cdot\hat{z}\sin(\omega t) \\ &\equiv B_I\cos(\omega t) + B_Q\sin(\omega t) \equiv B_{MW}\cos(\omega t - \phi). \end{aligned} \tag{9}$$

The phase is $\phi = \arctan(\frac{B_Q}{B_I})$ and the field strength is $B_{MW} = \sqrt{B_I^2 + B_Q^2}$. We can write in complex form $B_{mw,z} = \frac{1}{2}B_{MW}e^{-i\phi}e^{i\omega t} + \frac{1}{2}B_{MW}e^{i\phi}e^{-i\omega t} = \beta e^{i\omega t} + \beta^* e^{-i\omega t}$. Note that for a MW containing any amount of circularity there are only two directions for the quantization field in which the matrix element vanishes (directions perpendicular to the plane of polarization: $\pm\hat{a}\times\hat{b}$) while for a strictly linearly polarized MW, aligning the quantization axis anywhere in the plane perpendicular to the MW field will result in a vanishing interaction. Matrix elements of the interaction Hamiltonian between identical states simply vanishes: $\langle 1|\, H_I\,|1\rangle = \langle 2|\, H_I\,|2\rangle = 0$ because of interference. Similarly, with $|1\rangle, |2\rangle$ being eigenstates of the unperturbed Hamiltonian H_0 we have $\langle 1|\, H_0\,|2\rangle = 0$, $H_0\,|1\rangle = 0$ and $H_0\,|2\rangle = \hbar\omega_{hf}\,|2\rangle$.

The time dependent Schrödinger equation is $i\hbar\frac{\partial}{\partial t}\,|\psi(t)\rangle = (H_0 + H_I)\,|\psi(t)\rangle$. A general state is $|\psi\rangle = \alpha\,|1\rangle + \beta\,|2\rangle$. Therefore under the influence of H_0 alone we get that the evolution is simply $|\psi(t)\rangle = \alpha\,|1\rangle + \beta e^{-i\omega_{hf}t}\,|2\rangle$. We can write a general form with the evolution due to H_0 factored out (i.e. using the "interaction representation"): $|\psi(t)\rangle = c_1(t)\,|1\rangle + c_2(t)e^{-i\omega_0 t}\,|2\rangle$. plugging into the differential equation:

$$i\hbar\dot{c_1}\,|1\rangle + (\hbar\omega_{hf}c_2 + i\hbar\dot{c_2})e^{-i\omega_{hf}t}\,|2\rangle = (H_0 + H_I)(c_1\,|1\rangle + c_2 e^{-i\omega_{hf}t}\,|2\rangle).$$

By multiplying from the left with $\langle 1|$ or $\langle 2|$ we arrive at two coupled differential equations:

$$\begin{cases} \langle 1| : & i\hbar\dot{c_1} = c_2 e^{-i\omega_{hf}t}(\mu_B\beta e^{i\omega t} + \mu_B\beta^* e^{-i\omega t}) \\ \langle 2| : & (\hbar\omega_{hf}c_2 + i\hbar\dot{c_2})e^{-i\omega_{hf}t} = c_1(\mu_B\beta e^{i\omega t} + \mu_B\beta^* e^{-i\omega t}) + \hbar\omega_{hf}c_2 e^{-i\omega_{hf}t} \end{cases}$$

Dropping terms that are oscillating like $\omega_0 + \omega \approx 2\omega_0$ ("rotating wave approximation" or RWA) and with the Rabi frequency defined by $\frac{\hbar\Omega}{2} = \mu_B\beta$ and $\delta = \omega - \omega_0$ we arrive at a nicely symmetric form:

$$\begin{cases} \dot{c_1} = -ic_2\frac{\Omega}{2}e^{-i\delta t} \\ \dot{c_2} = -ic_1\frac{\Omega^*}{2}e^{i\delta t} \end{cases}$$

A more common choice (and sometimes more useful) for a rotating frame is a frame in which the MW field is stationary. With this choice $|\psi(t)\rangle = c_1|1\rangle + c_2 e^{-i\omega t}|2\rangle$ and we similarly arrive at

$$\begin{cases} \dot{c_1} = -ic_2\frac{\Omega}{2} \\ \dot{c_2} = -i\delta c_2 + ic_1\frac{\Omega^*}{2} \end{cases} \tag{10}$$

For resonant ($\delta = 0$) microwave fields, or when $\Omega \gg \delta$, this can be summarized by (NIST official ION rotation matrix...)

$$\begin{pmatrix} c_2(t) \\ c_1(t) \end{pmatrix} = \begin{pmatrix} \cos(\Omega t/2) & -ie^{-i\phi}\sin(\Omega t/2) \\ -ie^{i\phi}\sin(\Omega t/2) & \cos(\Omega t/2) \end{pmatrix} \begin{pmatrix} c_2(0) \\ c_1(0) \end{pmatrix} \tag{11}$$

and when the MW drive is absent, $\Omega = 0$ and then $c_2(t) = e^{-i\delta}c_2(0)$ and $c_1(t) = c_1(0)$.

2.6 Spectroscopy Techniques

2.6.1 Rabi Spectroscopy

For Rabi spectroscopy we prepare the state in the $|1\rangle$ state ($c_1(0) = 1$, $c_2(0) = 0$) and then apply a MW pulse. For free, non-interacting, atoms the population in the excited state is then $\rho_{22} = |c_2|^2 = \frac{|\Omega|^2}{|\Omega|^2+\delta^2}\sin^2(\frac{\sqrt{|\Omega|^2+\delta^2}}{2}t)$. The frequency δ is scanned while keeping the Rabi frequency Ω constant. For a π pulse interrogation, $\Omega t = \pi$, the resolution (spectral FWHM) is obtained from solving numerically the non-linear equation $\sin^2(\sqrt{x}\pi/2) = \frac{1}{2}x$

and is found to be $\delta_{FWHM} \approx 1.6\Omega$. Ideally, the resulting spectral shape is a convolution of the atomic distribution and the free spectrum above; see figure 2. This method, while straightforward, has several drawbacks. Firstly, it is necessary to use longer and longer MW pulse if better resolution is desired. However, during the pulse the atoms may evolve: they are moving in the trap, suffer collisions with one another and may be subject to other noisy processes. This makes the modeling exact spectral shape quite involved and dependent on many parameters. Secondly (and trivially), the atomic signal is made smaller with increasing resolution since the MW pulse interacts with fewer and fewer atoms. This makes measuring the tails of the atomic distribution, to which only few atoms contribute, difficult. Lastly, using long pulses presents a challenge since it is necessary to keep the pulse area constant at low MW power. In the experiment we mainly utilize this techniques for rough spectral estimation where the exact shape of the spectral line is of no great consequence, an example being measurement of the bias magnetic field via the shift experienced by a magnetic sensitive transition. For this purpose the method of Rabi spectroscopy is well adequate since it allows to measure the position of peak of the distribution using only few measurements points, making it a fast measurement.

2.6.2 Ramsey Spectroscopy

Another common spectroscopy technique is the so called "Ramsey spectroscopy" (originally "Ramsey's method of separated oscillatory fields" [35]). In Ramsey spectroscopy the long Rabi π pulse is divided into two $\pi/2$ pulses, separated by a time T. The resolution is now determined by the inverse of this interval $\frac{1}{T}$, and not by the inverse of the pulse length, $\frac{1}{T_{pulse}}$, and so the pulses themselves can be made short by increasing the MW power and the Rabi frequency. Care must be taken to keep $\Omega \ll \mu_B B$, otherwise the interaction will involve states other than $|1\rangle, |2\rangle$ and the underlying assumption about a two-level system is no longer valid. With the MW pulses much shorter than any other timescale in the problem (e.g. oscillation time in the trap, time between collisions, etc), they can be treated as instantaneous, and we need not take into account the dynamics that occurs during the pulses, much simplifying the situation [26].

Ideally, a Ramsey experiment can be thought of as an atomic interferometer involving

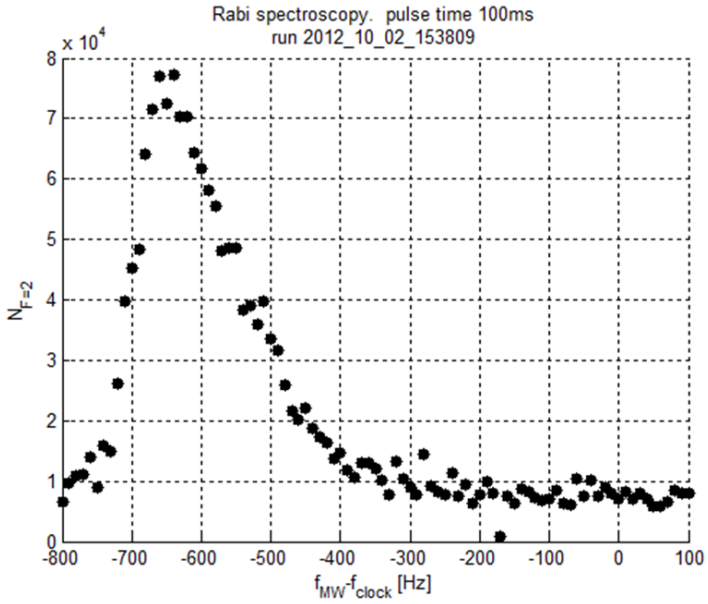

Figure 2: Rabi spectroscopy of atoms in a deep trap. The trap depth can be estimated from shift and the known values of the differential and ground state polarizabilities $U_0 \approx 1\text{mK}$

the two states $|1\rangle, |2\rangle$: each $\pi/2$ pulse acts as a beam splitter converting $|1\rangle \underset{\pi/2}{\rightarrow} \frac{1}{\sqrt{2}}|1\rangle - \frac{i}{\sqrt{2}}|2\rangle$ and $|2\rangle \underset{\pi/2}{\rightarrow} -\frac{i}{\sqrt{2}}|1\rangle + \frac{1}{\sqrt{2}}|2\rangle$. Two consecutive $\pi/2$ pulses like these, with the same phase and with no evolution between them are just a π pulse:

$$|1\rangle \underset{\pi/2}{\rightarrow} \frac{1}{\sqrt{2}}|1\rangle - \frac{i}{\sqrt{2}}|2\rangle \underset{\pi/2}{\rightarrow} \frac{1}{\sqrt{2}}(\frac{1}{\sqrt{2}}|1\rangle - \frac{i}{\sqrt{2}}|2\rangle) - \frac{i}{\sqrt{2}}(-\frac{i}{\sqrt{2}}|1\rangle + \frac{1}{\sqrt{2}}|2\rangle) = -i|2\rangle .$$

$$|2\rangle \underset{\pi/2}{\rightarrow} -\frac{i}{\sqrt{2}}|1\rangle + \frac{1}{\sqrt{2}}|2\rangle \underset{\pi/2}{\rightarrow} -\frac{i}{\sqrt{2}}(\frac{1}{\sqrt{2}}|1\rangle - \frac{i}{\sqrt{2}}|2\rangle) + \frac{1}{\sqrt{2}}(-\frac{i}{\sqrt{2}}|1\rangle + \frac{1}{\sqrt{2}}|2\rangle) = -i|1\rangle .$$

The second pulse can have a phase relative to the preparation pulse (simply by changing the phase of the MW oscillator). In the RWA this phase is just translated to a phase in the Rabi frequency of the second pulse: $\Omega \rightarrow e^{i\phi}\Omega$. The result is $|1\rangle \underset{\frac{\pi}{2},\phi}{\rightarrow} \frac{1}{\sqrt{2}}|1\rangle - ie^{-i\phi}\frac{1}{\sqrt{2}}|2\rangle$

and $|2\rangle \underset{\frac{\pi}{2},\phi}{\rightarrow} -\frac{i}{\sqrt{2}}e^{-i\phi}|1\rangle + \frac{1}{\sqrt{2}}|2\rangle$. The full Ramsey sequence involving the two pulses, preparation and analysis pulses, is therefore described by:

$$|1\rangle \underset{\frac{\pi}{2}}{\rightarrow} \frac{1}{\sqrt{2}}|1\rangle - \frac{i}{\sqrt{2}}|2\rangle \underset{\frac{\pi}{2},\phi}{\rightarrow} \frac{1}{\sqrt{2}}(\frac{1}{\sqrt{2}}|1\rangle - \frac{i}{\sqrt{2}}e^{-i\phi}|2\rangle) - \frac{i}{\sqrt{2}}(-\frac{i}{\sqrt{2}}e^{i\phi}|1\rangle + \frac{1}{\sqrt{2}}|2\rangle)$$
$$= \frac{1}{2}(1-e^{i\phi})|1\rangle - \frac{i}{2}(1+e^{-i\phi})|2\rangle$$

The directly measurable quantity is the population of the $|2\rangle$ state which after a Ramsey experiment is $|c_2|^2 = \cos^2(\phi/2) = \frac{1}{2}(1+\cos(\phi))$. By scanning the MW phase ϕ of the second $\pi/2$ pulse we therefore get a fringe, analogous to the fringe observed at the output of a Mach-Zender interferometer when the optical length of one of the paths is scanned.

The evolution of a single atom prepared in a superposition state by a $\pi/2$ pulse and experiencing a shift δ in its resonant frequency due to an differential AC stark shift is simple in the rotating frame: $|\psi(t')\rangle = \frac{1}{\sqrt{2}}|1\rangle - \frac{i}{\sqrt{2}}e^{-i\delta t'}|2\rangle$. After some time t the second $\pi/2$ pulse is applied and we get

$$|\psi(t)\rangle \underset{\pi/2}{\rightarrow} \frac{1}{\sqrt{2}}(\frac{1}{\sqrt{2}}|1\rangle - \frac{i}{\sqrt{2}}|2\rangle) - e^{-i\delta t}\frac{i}{\sqrt{2}}(-\frac{i}{\sqrt{2}}|1\rangle + \frac{1}{\sqrt{2}}|2\rangle) =$$
$$= \frac{1}{2}(1-e^{-i\delta t})|1\rangle - \frac{i}{2}(1+e^{-i\delta t})|2\rangle$$
$$= -ie^{-i\delta t/2}(\sin(\delta t/2)|1\rangle + \cos(\delta t/2)|2\rangle).$$

We only measure the population of the $|2\rangle$ state and so $|c_2^2| = \cos^2(\delta t/2) = \frac{1}{2}(1+\cos(\delta t))$. For an atomic ensemble in which not all the atoms experience the same shift (due to inhomogeneous broadening) we can define a distribution of detunings $\rho(\delta)$. Assuming the atoms are non interacting and that the system is closed (no external noise sources, no scattering of photons etc.) then each atom remains in its energy class and its average detuning δ is retained for the duration of the experiment. The ensemble average population

is given by

$$|c_2(t)|^2 = \frac{1}{2}\int d\delta(1+\cos(\delta t))\rho(\delta) = \frac{1}{2} + \frac{1}{2}\int d\delta\rho(\delta)\cos(\delta t) = \frac{1}{2} + \frac{1}{2}\Re\{\int d\delta\rho(\delta)e^{-i\delta t}\}, \tag{12}$$

where I used $\int dx\rho(x) = 1$. This is the Fourier transform of the distribution $\rho(\delta)$ which for non interacting particles is fully determined by the temperature and the shape of the trapping potential.

For an harmonic trap, with the potential energy distribution given by Eq. (4), $\rho(\delta)$ is obtained by a simple change of variables [26]

$$\rho(\delta_{ls}) = \frac{K^3}{2}(\delta_{ls} - \delta_0)^2 e^{-K(\delta_{ls}-\delta_0)}, \tag{13}$$

where $K = \frac{2\hbar}{\eta k_B T}$, $\delta_{ls}(\langle V\rangle) = \delta_0 + \frac{\eta\langle V\rangle}{\hbar}$. δ_0 is the maximal detuning at the trap bottom, $\langle V\rangle$ is the time averaged potential energy of the atom in the trap, $\eta = \frac{\Delta E_{HF}}{\Delta E_{S_{\frac{1}{2}}}} = \frac{\alpha_{hf}}{\alpha_0}$ is the ratio between the differential light shift and the light shift for the ground state, responsible for the trapping.

It should be clarified why it is the *average* potential energy that must be used here. Consider the instantaneous potential energy of one of the atoms in the ensemble:

$$V = \frac{1}{2}m\omega_x^2 x(t)^2 + \frac{1}{2}m\omega_z^2 y(t)^2 + \frac{1}{2}m\omega_z^2 z(t)^2.$$

The coordinates just change sinusoidally in time, $x_i(t) = A_i\cos(\omega_i t + \varphi_i)$, A_i and φ_i depending on initial conditions, but since generally the motion in (x, y, z) are not in phase, the trajectory is complicated and is actually a form of a three dimensional Lissajous curve. The instantaneous detuning due to light shift is simply $\delta(t) = \eta V(t)$ and the total phase accumulated between the two parts of the superposition is the time integral of the

instantaneous detuning $\phi(t) = \int_0^t dt' \delta(t')$.

$$\begin{aligned} \phi(t) &= \eta \sum_{i=x,y,z} m\omega_i^2 A_i^2 \int_0^t \cos^2(\omega_i t + \varphi_i) dt \\ &= \eta \sum_{i=x,y,z} \frac{m\omega_i^2 A_i^2}{2} \left(\frac{t}{2} + \frac{1}{4\omega_i} \sin(2\omega_i t + 2\varphi_i) - \frac{1}{4\omega_i} \sin(2\varphi_i) \right) \\ &= \eta \langle V \rangle t + \eta \sum_{i=x,y,z} \frac{m\omega_i A_i^2}{8} \left(\sin(2\omega_i t + 2\varphi_i) - \sin(2\varphi_i) \right) \end{aligned} \tag{14}$$

where we have identified $\langle V \rangle = \frac{m}{4} \sum_i \omega_i^2 A_i^2$. The first term in Eq.(14) is just a linearly advancing phase that depends on the *time averaged* potential of the atom, as would be obtained from the virial theorem. The second and third terms are bounded, and in times long enough ($\eta \langle V \rangle t \gg 1$) are negligible compared with the first term which is linear in t (modulo 2π). Taking into account that many atoms may be found in the same energy interval $(E, E + \delta E)$, and that their initial conditions are randomly and uniformly distributed in phase space, the experiment averages over them and their contribution is negligible. A typical Ramsey signal, together with its Fourier transform are shown in Fig.5. The transformed signal is fitted with Eq.(13).

The time domain Ramsey signal can be obtained from the distribution in Eq.(13) by Fourier transform [26], as in Eq.(12):

$$
\begin{aligned}
R(t) &= \Re\left\{\int_{-\infty}^{\infty} d\delta\rho(\delta)e^{-i\delta t}\right\} \\
&= \frac{K^3}{2}\Re\left\{\int_{\delta_0}^{\infty} d\delta(\delta-\delta_0)^2 e^{-K(\delta-\delta_0)}e^{-i\delta t}\right\} \\
\delta'=\delta-\delta_0 &= \frac{K^3}{2}\Re\left\{e^{-i\delta_0 t}\int_{0}^{\infty} d\delta\delta^2 e^{-K\delta}e^{-i\delta t}\right\} \\
&= \frac{K^3}{2}\Re\left\{e^{-i\delta_0 t}\frac{d^2}{dK^2}\int_{0}^{\infty} d\delta e^{-K\delta}e^{-i\delta t}\right\} \\
&= K^3\Re\left\{\frac{1}{(K+it)^3}e^{-i\delta_0 t}\right\} \\
&= \Re\left\{\frac{1}{\left(1+\left(\frac{t}{K}\right)^2\right)^{\frac{3}{2}}}e^{-i3\arctan\left(\frac{t}{K}\right)}e^{-i\delta_0 t}\right\} \\
&= \frac{1}{\left(1+\left(\frac{t}{K}\right)^2\right)^{\frac{3}{2}}}\cos\left(\delta_0 t+3\arctan\left(\frac{t}{K}\right)\right)
\end{aligned}
$$

Here δ_0 is simply the detuning at the trap bottom. Including the assumption of $\delta_0 = -|\delta_0|$ we return to the waveform derived in [26]:

$$
R(t) = \frac{1}{\left(1+\left(\frac{t}{K}\right)^2\right)^{\frac{3}{2}}}\cos\left(|\delta_0|\, t-3\arctan\left(\frac{t}{K}\right)\right). \tag{15}
$$

The additional phase term in the cosine is easy to understand in terms of the non symmetric distribution in the frequency domain, since any pure amplitude modulation will only give rise to a symmetric distribution in frequency domain. Another nice feature is the relatively slow decay of the Ramsey signal: at $t \gg K$ the signal decay as $(t/K)^{-3}$ only, as opposed to the exponential decay associated with Lorentzian lineshapes. This shouldn't be surprising since the spectral lineshape here has a strict cutoff from below at δ_0 (trap bottom has associated with it a maximal detuning) and is exponentially decreasing , due to the Boltzman factor, from above. However, this may be misleading, as seen in Fig.(3), where an exponential decaying function is compared to a decay of the form in

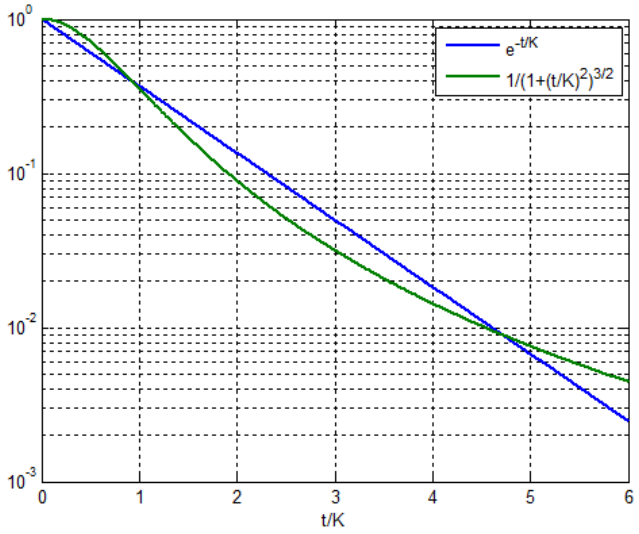

Figure 3: Comparison between exponential $e^{-t/K}$ decay and decay of the form $\frac{1}{\left(1+\left(\frac{t}{K}\right)^2\right)^{\frac{3}{2}}}$

Eq.(15) . Only for times $t < K$ the coherence is better with the non exponential decay, but afterwards exponential decay will allow for better coherence in the signal. The roles are again reversed at $t \approx 5K$, but at that point the coherence is practically lost with only 1% contrast remaining.

2.6.3 Echo and beyond.

We examine the state of an atom with detuning δ at a time t after the first Ramsey pulse $|\psi(t)\rangle = \frac{1}{\sqrt{2}}|1\rangle - \frac{i}{\sqrt{2}}e^{-i\delta t}|2\rangle$. Different atoms in the ensemble experience different average detunings and so their coherence is lost. But this type of decoherence (commonly referred to merely as "de-phasing") can be reverted by the application of a so called "echo pulse" [18]: a π pulse is applied with the result of interchanging between $|1\rangle$ and $|2\rangle$: $|\psi(t)\rangle \underset{\pi}{\rightarrow} -\frac{i}{\sqrt{2}}|2\rangle - \frac{1}{\sqrt{2}}e^{-i\delta t}|1\rangle$. Allowing the state to evolve for another duration t we get $|\psi(2t)\rangle_{\pi@t} = -\frac{i}{\sqrt{2}}e^{-i\delta t}|2\rangle - \frac{1}{\sqrt{2}}e^{-i\delta t}|1\rangle = e^{-i\delta t}(\frac{1}{\sqrt{2}}|1\rangle + \frac{i}{\sqrt{2}}|2\rangle)$. Applying the final $\pi/2$ Ramsey pulse we get $|\psi\rangle = e^{-i\delta t}|1\rangle$. The phase is now global and does not affect the coherence. An example of the effect is shown in figure 6: in this experiment a single echo pulse has the effect of extending the time in which the coherence decays to $1/e$ of its

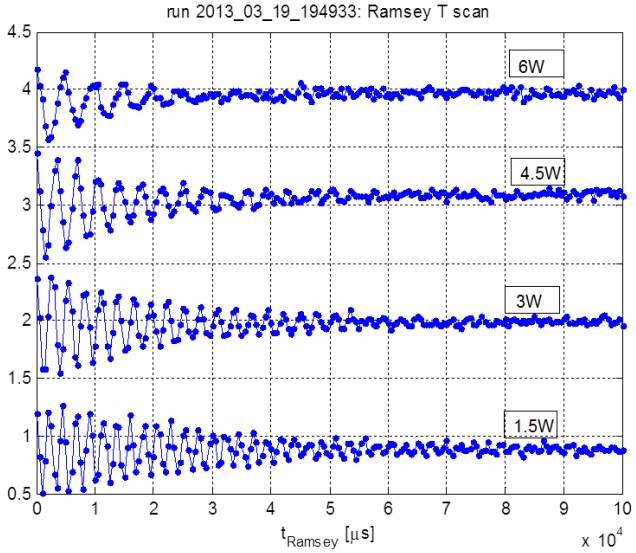

Figure 4: Ramsey scans for various trap powers. For deeper traps the atoms are hotter and decoherence is faster. The carrier detuning was adjusted such that many oscillations are visible within the coherence time for all the runs shown.

initial value by a factor of 4. Alternatively, the contrast at a time of 40ms in increased by factor of 7. Obviously, the coherence *does* decay at longer time, but this is not due to the inhomogeneous broadening caused by the trapping potential. Other processes are present, including collisions between atoms that causes them to change energy classes and average detuning, noise in the trapping potential, magnetic noises (to a lower extent since we are working on the clock transition) and other factors such as phase and frequency noise in the MW source itself. It is possible to extend the coherence even further by applying not a single echo pulse, but a train of echo pulses at intervals shorter than the typical correlation time of the different noise sources, i.e. pulses repeated faster then the collision rate will reduce the decoherence caused by such interactions to a large extent [1, 39, 22], as shown in Fig.7. The culprit now will be noises in the control field itself: errors in the pulse area will be accumulated when many pulses are applied and will be a source of decoherence. Such errors may be minimized by utilizing various pulse sequences, i.e. CPMG and the likes [1].

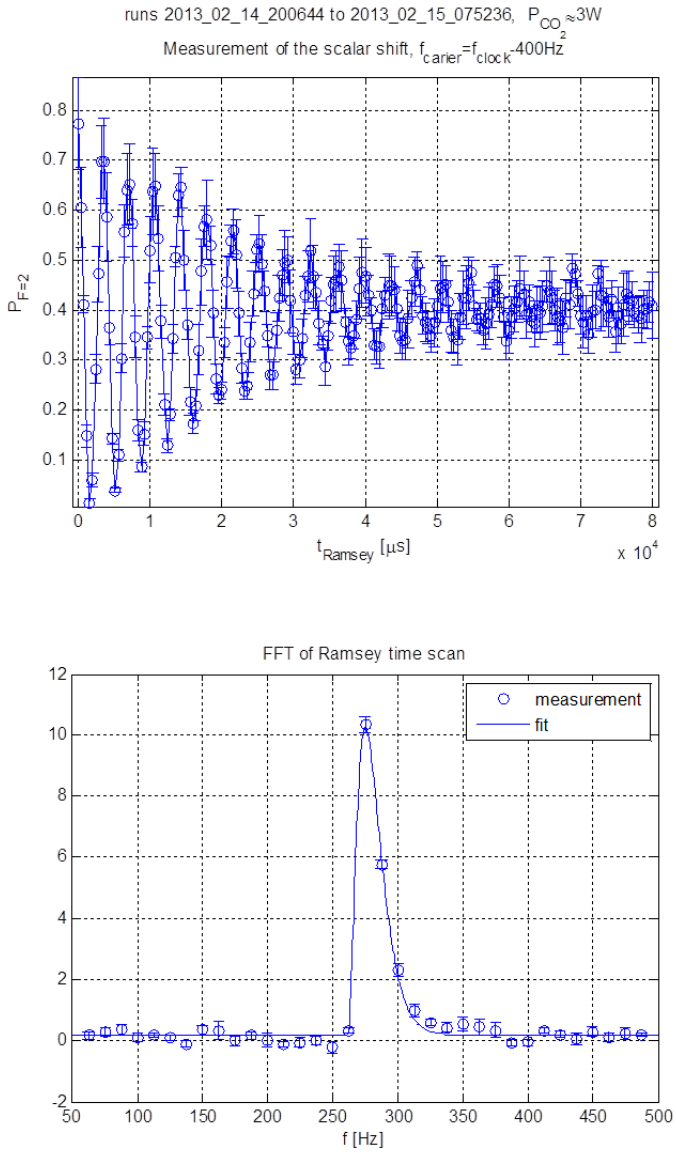

(a)

Figure 5: A measurement of the scalar shift. top: raw Ramsey signal. bottom: Fourier transform of the Ramsey signal and a fit to eq (13) yielding $f_0 = 261.7 \pm 0.7$Hz, $T = 20.45 \pm 0.8\mu K$. Taking into account the carrier detuning of -400Hz and the second order Zeeman shift of 15.5Hz: $\delta_0 = -400 + 15.5 + 261.7 = 153.8 \pm 0.7$Hz where the error in the second order Zeeman shift is neglected.

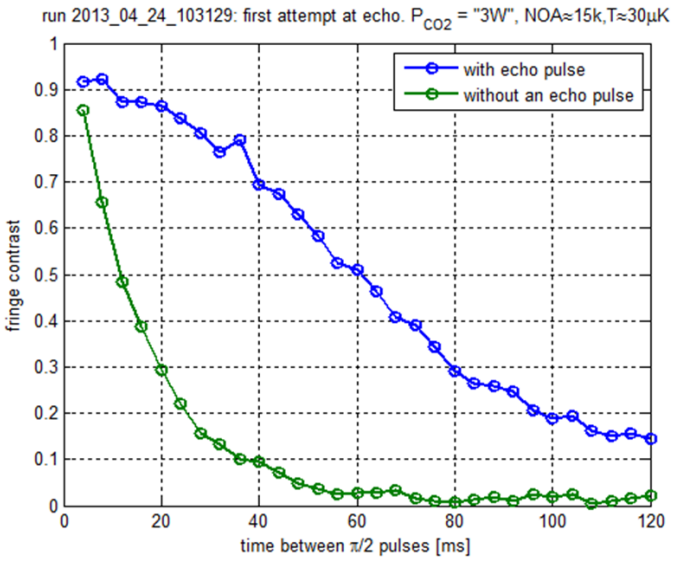

Figure 6: Ramsey fringe contrast, with and without an echo pulse halfway between the preparation and analysis $\pi/2$ pulses.

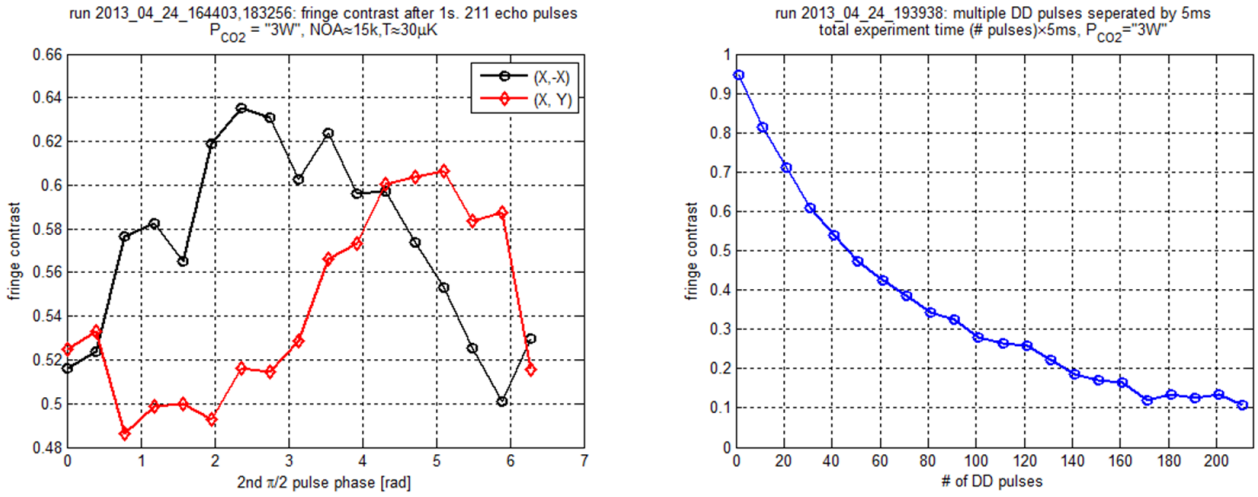

(a) (b)

Figure 7: **(a)** A multiple echo sequence with 211 pulses. A fringe contrast of 10% is retained after 1s. Two sequences are compared: (X,Y,X,Y..) and (X,-X,X,-X..) **(b)** Fringe contrast vs number of pulses with a (X,Y,X,Y..) sequence. Time between pulses is fixed at 5ms. 1/e time is ~0.5s with 100 pulses.

2.7 The ground state polarizability - revisited

The calculation of the polarizability of alkali atoms, as presented in section 2.2, is overly simplified. Atoms, even relatively simple ones like the alkali, are very complex entities, and by considering them as simple isotropic electronic charge distribution we miss many interesting features arising from their complicated structure. In this section several aspects of the polarizability will be discussed, including the the factorization of the polarizability to scalar, vector and tensor parts and how these different polarizabilities effects the interaction of the atom with an electric field.

2.7.1 Polarizability - not just a scalar

We begin again with the polarizability as it appears in a classical context. A neutral charge distribution, when placed in an electric field will experience a displacement of its negatively charged constituents from its positive ones, and will thus develop a dipole moment. For a small field the dipole magnitude is proportional to the field. However, the induced dipole need not necessarily be parallel to the original field and a more general expression than that given in section 2.2 would include the polarizability tensor α_{ij}:

$$d_i = er_i = \alpha_{ij} E_j$$

where d_i are the Cartesian components of the induced dipole moment and α_{ij} is a second rank tensor and a summation convention over repeating indices applies. A simple example of such is a behavior conductive one dimensional wire that is placed in an electric field: the induced dipole can only be along the wire, regardless of the direction of the field.

A second rank tensor can always be written as a sum symmetric and anti-symmetric tensors: $\alpha_{ij} = \alpha^a_{ij} + \alpha^s_{ij}$ where $\alpha^a_{ij} = \frac{1}{2}(\alpha_{ij} - \alpha_{ji}) = -\alpha^a_{ji}$ and $\alpha^s_{ij} = \frac{1}{2}(\alpha_{ij} + \alpha_{ji}) = \alpha^s_{ji}$. Further, the symmetric part can be decomposed to a traceless symmetric tensor $\alpha^t_{ij} = \alpha^s_{ij} - \alpha_{ii}$ and a scalar tensor $\alpha^0_{ij} = \frac{1}{3}\alpha_0 \delta_{ij}$ where $\alpha_0 = \sum_i \alpha_{ii}$ is just the isotropic polarizability encountered before.

Lets check how the different parts composing the polarizability transform under rotations. Generally a second rank tensor can be composed of dyadics made of cartesian

vectors $\alpha_{ij} = \sum_k u_i^k v_j^k$ or in operator form $\overleftrightarrow{\alpha} = \sum_k \vec{u}^k \otimes \vec{v}^k$ where $\otimes$ is an outer product between vectors. A rotation on the tensor $\overleftrightarrow{\alpha}$ is performed by rotating each of the vectors so that $\alpha'_{ij} = R_{il}R_{jm}\sum_k u_l^k v_m^k = R_{il}R_{jm}\alpha_{lm}$. When applying the rotation separately to the trace, the antisymmetric and the traceless symmetric parts of $\overleftrightarrow{\alpha}$ we find that each transforms according to the same rule but retains its symmetries, i.e, the scalar does not transform (it is a scalar!), the antisymmetric part transforms onto an antisymmetric part and symmetric traceless tensor remains a symmetric traceless tensor. Thus, the representation of the polarization in Cartesian coordinates has been reduced to three parts that do not mix when rotated - unlike the nine constituents in the original Cartesian representation. Each of the constituents of the new factorization cannot be reduced further - it is an "irreducible representation" of the rotation operator. The numbers naturally add up: there are nine independent coefficient of α_{ij} but this is reducible to a scalar with one component, which in terms of the vectors $\vec{u}$ and $\vec{v}$ is just a scalar product $\alpha^0 = \frac{1}{3}\mathbf{u}\cdot\mathbf{v}$, an antisymmetric tensor with 3 nonzero components which can be seen as a vector product $\vec{c} = \vec{u} \times \vec{v}$ and a traceless symmetric tensor with 5 (6-1) independent components.

An antisymmetric rank 2 tensor has only 3 independent non zero components (since the diagonal is all zeros and the rest are related by $\alpha^a_{ij} = -\alpha^a_{ji}$), and it can be shown **[5]** that it can be written in terms of a (pseudo) vector $\mathbf{c}$ given by $c_i = \frac{1}{2}\varepsilon_{ijk}\alpha^a_{jk}$. Attention should be drawn to the fact that since, for any vector $\mathbf{E}$, the vector product $(\mathbf{b})_i = (\mathbf{c}\times\mathbf{E})_i = \varepsilon_{ijk}c_jE_k = \alpha^a_{ij}E_j$ is orthogonal to the original $\mathbf{E}$, and to the embedded pseudo-vector $\mathbf{c}$. Therefore an antisymmetric part of the polarizability would give rise to an induced dipole that is perpendicular to the field that created it and it has no component along $\mathbf{c}$, so for a field aligned along $\mathbf{c}$, the antisymmetric part is not contributing to the induced dipole. It is reasonable to assume that there are some principle axes that could be reached by pure rotation that an application of a field along which will induce a dipole parallel to the field. However, if such principle axes existed, then the antisymmetric part must vanish since in this basis the polarizability tensor is diagonal. This is indeed the case - at least when considering static fields alone, i.e. there is no vector part to the polarizability tensor for static fields. For dynamic fields it is generally possible to have a vector polarizability. This is because that given that the field rotates fast enough, the lag in dipole moment oscillation after the field direction will result in a part of the dipole that is perpendicular

to the field regardless of its direction.

Consider the symmetric part α^s_{ij} in a reference frame in which it is diagonal. In this frame its action is intuitively clear - it rescales each of of the components of the field according to the its eigenvalues $\alpha_1, \alpha_2, \alpha_3$ to produce a dipole moment which is not necessarily parallel to the field.

Looking at the traceless part alone, its eigenvalues are $(\frac{2}{3}\alpha_1 - \frac{1}{3}\alpha_2 - \frac{1}{3}\alpha_3, -\frac{1}{3}\alpha_1 + \frac{2}{3}\alpha_2 - \frac{1}{3}\alpha_3, -\frac{1}{3}\alpha_1 - \frac{1}{3}\alpha_2 + \frac{2}{3}\alpha_3)$. For the isotropic case, $\alpha_1 = \alpha_2 = \alpha_3$, the tensor polarizability vanishes and the only non zero polarizability is the a scalar part. In a system with cylindrical symmetry two of the eigenvalues must have magnitudes, say $\alpha_1 = \alpha_2 = \alpha_\perp$ and then the eigenvalues for the traceless symmetric tensor become $\left(\frac{1}{3}\alpha_\perp - \frac{1}{3}\alpha_\parallel, \frac{1}{3}\alpha_\perp - \frac{1}{3}\alpha_\parallel, -\frac{2}{3}\alpha_\perp + \frac{2}{3}\alpha_\parallel\right) = \frac{\alpha_\perp - \alpha_\parallel}{3}(1, 1, -2)$ meaning there is really one independent polarizability coefficient $\alpha_T = \frac{\alpha_\perp - \alpha_\parallel}{3}$ and the ratio of the tensor polarizabilities between the axial and radial axes is just 2. The total polarizability includes also the scalar part. For our intuitive example of a one dimensional wire the two equal eigenvalues of the total polarizability tensor must vanish, therefore $\alpha_0 = \alpha_\parallel - \alpha_\perp$ and we arrive at a simple expression for the tensor polarizability, written in terms of the scalar polarizability, in the diagonal basis:

$$\alpha_T^{\text{1D wire}} = \frac{\alpha_0}{3}\begin{pmatrix} -1 & 0 & 0 \\ 0 & -1 & 0 \\ 0 & 0 & 2 \end{pmatrix}.$$

Finally, as the energy of interaction between the field and the induced dipole is $U = -\frac{1}{2}\alpha_{ij}E_iE_j = -\frac{1}{2}Tr\{\boldsymbol{\alpha}\boldsymbol{\chi}^\dagger\}$ where $\boldsymbol{\chi} = \{\mathbf{EE}\}$ is the rank 2 tensor constructed from the components of the field. Similarly to $\boldsymbol{\alpha}$, the tensor $\boldsymbol{\chi}$ can be decomposed into scalar, vector and tensor parts then the energy becomes $U = -\frac{1}{2}Tr\{(\alpha^0 + \alpha^1 + \alpha^2)(\chi^0 + \chi^1 + \chi^2)\}$. Since $Tr\{AS\} = 0$ for a symmetric A and antisymmetric S the sum simplifies to $U = -\frac{1}{2}Tr\{\alpha^0\chi^0\} - \frac{1}{2}Tr\{\alpha^1\chi^1\} - \frac{1}{2}Tr\{\alpha^2\chi^2\}$. The first term is just the energy due to the scalar part of the polarizability and it is proportional to $|E|^2$. The second term (vector) is identically zero for static fields or linearly polarized light. The third term is the contribution from the tensor polarizability to the energy. We can easily evaluate the third term in the basis that diagonalizes α^2 - for atomic wavefunctions this simply implies putting the quantization axis along $\hat{z}$. In this basis we can immediately write the trace

of the multiplication as the scalar product between the diagonals of the two matrices ($|\varepsilon_i|^2 - \frac{1}{3}|\varepsilon|^2$ are just the diagonal terms of the traceless χ^2, with $|\varepsilon|^2 = \sum_i \varepsilon_i^2$):

$$\begin{aligned} Tr\{\alpha^2\chi^2\} &= \alpha_1\chi_{11} + \alpha_2\chi_{22} + \alpha_3\chi_{33} = \\ &= \alpha_1(|\varepsilon_x|^2 - \frac{1}{3}|\varepsilon|^2) + \alpha_2(|\varepsilon_y|^2 - \frac{1}{3}|\varepsilon|^2) + \alpha_3(|\varepsilon_z|^2 - \frac{1}{3}|\varepsilon|^2) = \\ &= \alpha_T(|\varepsilon_y|^2 + |\varepsilon_x|^2 - \frac{2}{3}|\varepsilon|^2) - 2\alpha_T(|\varepsilon_z|^2 - \frac{1}{3}|\varepsilon|^2) = \\ &= -\alpha_T(3|\varepsilon_z|^2 - |\varepsilon|^2) \end{aligned}$$

where in the last two steps we assumed cylindrical symmetry (so $\alpha_1 = \alpha_2$ and $\alpha_3 = -\alpha_1 - \alpha_2$ for tracelessness) and used explicitly $|\varepsilon_x|^2 + |\varepsilon_y|^2 = |\varepsilon|^2 - |\varepsilon_z|^2$. To summarize, the dependence of the tensor polarizability shift on the field has the form $(3|\varepsilon_z|^2 - |\varepsilon|^2) = |\varepsilon|^2(3\cos^2(\theta) - 1)$ where θ is the angle between the field and the axis of quantization (the axial direction of a polarizable body having a cylindrical symmetry).

Up to this point, we have only considered the response to stationary (DC) field, or equivalently the case of an instantaneous response. In general, as already seen in the rather naive treatment in section 2.2, the polarizability can have some phase with respect to an oscillating field. In the following we write again the energy of interaction using the real part of the classical dipole found before (still purely scalar at this point)

$$\begin{aligned} U &= -\frac{1}{2}\langle d \cdot E\rangle = -\frac{1}{2}\left\langle(\alpha\varepsilon e^{-i\omega t} + \alpha^*\varepsilon^* e^{-i\omega t})(\varepsilon e^{-i\omega t} + \varepsilon^* e^{-i\omega t})\right\rangle \\ &= -\frac{1}{2}\left\langle\alpha\varepsilon\varepsilon^* + \alpha^*\varepsilon^*\varepsilon + \alpha\varepsilon\varepsilon e^{-i2\omega t} + \alpha^*\varepsilon^*\varepsilon^* e^{-i2\omega t}\right\rangle \end{aligned}$$

where the angle brackets denote a time average. The fast oscillating terms do not contribute to the average energy and we are left with $U = -\frac{1}{2}(\alpha\varepsilon\varepsilon^* + \alpha^*\varepsilon^*\varepsilon)$. Cutting through some corners we proceed by simply promoting the α and $\varepsilon\varepsilon^*$ to rank 2 tensors and we end up where we wanted to be

$$U = -\frac{1}{2}(\alpha_{ij}\varepsilon_i\varepsilon_j^* + \alpha_{ij}^*\varepsilon_i^*\varepsilon_j).$$

Unlike the DC case, now there can be a antisymmetric part to both the polarizability and the electric field tensor χ, and a contribution to the interaction energy from the vector

polarizability is expected. Some intuition as to the nature of the vector polarizability can be gained by the following argument. As already discussed in previous paragraphs the role of the antisymmetric part is to create a dipole which is always perpendicular to the field. But then how can the field interact with the vector part of the dipole? This can only be if the field rotates continuously, and the dipole lags behind it, such that the two vectors are not strictly perpendicular. Then it is clear why the vector polarizability is simply zero for static fields, and also why a circular polarization is required. There is an interesting connection between dissipation and the vector polarizability. Without dissipation and the accompanying phase lag, there will be no vector part to the polarizability, and anyway - they both depend on the imaginary part of the polarizability in the same way.

We have seen that the polarizability tensor, expressed in a Cartesian basis, can be written in the form of three distinct parts that transform under rotations as a scalar, vector and a tensor, and do not mix within themselves. However, a Cartesian basis is not the only possible basis, and when a certain spherical symmetry exist a spherical basis may simplify matters greatly, since in this basis the representation is already irreducible. Then we can write the scalar part simply as a rank 0 spherical tensor α_0^0, the vector part as a rank 1 spherical tensor with 3 components, $\alpha_{q=0,\pm1}^{K=0}$ and the traceless symmetric part as a rank 2 spherical tensor with 5 components $\alpha_{q=0,\pm1,\pm2}^{K=2}$. We can similarly write the Cartesian field components in term of spherical vectors with $E_0 = E_z$ and $E_{\pm1} = \mp\frac{1}{\sqrt{2}}(E_x \pm iE_y)$. As the energy of interaction between the field and the induced dipole is $U = -\frac{1}{2}\alpha_{ij}E_iE_j$ it can be considered as a scalar product between the polarizability tensor and a tensor composed of the components of the field. The in the spherical basis the energy is $U = -\frac{1}{2}\sum_{k=0}^{2}\sum_{q=-K}^{K}(-1)^q\alpha_q^K\{EE\}_{-q}^K$. The formulation of the problem in terms of spherical tensors is quite convenient and allows for immediate results when evaluating the polarizability of an atom in a specific quantum state, since the electronic wavefunction is commonly constructed out of angular momentum eigenstates. Then the evaluation of the relevant matrix elements is an exercise in the addition of angular momentum.

2.7.2 Atomic dipole polarizability

Let us consider the stark interaction $\mathcal{H}_{Stark} = -\mathbf{d}\cdot\mathbf{E}$ as a perturbation. We assume that the atom can be described by the free Hamiltonian $\mathcal{H}_0$ and that all of its eigenstates $\left|n^{(0)}\right\rangle$ and energies $E_n^{(0)}$ are known. The details of perturbation theory can be found in any text book on quantum mechanics. Here I only present the basic framework. In a perturbative approach we assume that the correction to the Hamiltonian is small and has the effect of changing the wavefunction and energies of the original Hamiltonian by a little bit: $|n\rangle = \left|n^{(0)}\right\rangle + \lambda\left|n^{(1)}\right\rangle + \lambda^2\left|n^{(2)}\right\rangle + ...$ and $E_n = E_n^{(0)} + \lambda E_n^{(1)} + \lambda^2 E_n^{(2)} + ...$ The parameter λ is taken to be 1 at the end of the calculation and only serves to help with bookkeeping the number of times the perturbation comes in (the order of the correction). As always $\mathcal{H}\left|n\right\rangle = E\left|n\right\rangle$. We plug in $\mathcal{H} = \mathcal{H}_0 + \lambda V$ (V is a generic perturbation) and the expressions for the perturbed energies and states and collect terms of same order in λ. The results are well known (for a century..) and can be found in any basic textbook on quantum mechanics [40, 43]

$$\begin{aligned}\left|n^{(1)}\right\rangle &= -\sum_{m\neq n}\left|m^{(0)}\right\rangle\frac{\left\langle m^{(0)}\left|\mathcal{H}_{Stark}\right|n^{(0)}\right\rangle}{E_m^{(0)}-E_n^{(0)}}\\ E_n^{(1)} &= \left\langle n^{(0)}\left|\mathcal{H}_{Stark}\right|n^{(0)}\right\rangle\end{aligned}$$

for the first order correction. Explicitly for the Stark interaction $E^{(1)} = -\left\langle n^{(0)}\left|\mathbf{d}\right|n^{(0)}\right\rangle\cdot\mathbf{E} = 0$ because the dipole operator $\hat{\mathbf{d}} = -e\hat{\mathbf{r}}$ is of odd parity and cannot have an expectation value between states of definite parity. Continuing to second order in the energy

$$\begin{aligned}E_n^{(2)} &= -\sum_{m\neq n}\frac{\left\langle n^{(0)}\left|\mathcal{H}_{Stark}\right|m^{(0)}\right\rangle\left\langle m^{(0)}\left|\mathcal{H}_{Stark}\right|n^{(0)}\right\rangle}{E_m^{(0)}-E_n^{(0)}}\\ &= -\left\langle n^{(0)}\right|\left[\sum_{m\neq n}\frac{\hat{\mathbf{d}}\cdot\mathbf{E}\left|m^{(0)}\right\rangle\left\langle m^{(0)}\right|\hat{\mathbf{d}}\cdot\mathbf{E}}{E_m^{(0)}-E_n^{(0)}}\right]\left|n^{(0)}\right\rangle.\end{aligned}$$

Comparing to $\Delta E = -\frac{1}{2}\alpha\mathbf{E}^2$ we define the quantum mechanical polarizability operator

(valid to second order in perturbation theory) as

$$\hat{\boldsymbol{\alpha}}_{\boldsymbol{n}} = 2\left\langle n^{(0)}\right| \sum_{m\neq n} \frac{\hat{\mathbf{d}}\left|m^{(0)}\right\rangle\left\langle m^{(0)}\right|\hat{\mathbf{d}}}{E_m^{(0)} - E_n^{(0)}} \left|n^{(0)}\right\rangle$$

or in component form

$$\hat{\alpha}_{ij,n} = 2\left\langle n^{(0)}\right| \sum_{m\neq n} e^2 \frac{\hat{r}_i\left|m^{(0)}\right\rangle\left\langle m^{(0)}\right|\hat{r}_j}{E_m^{(0)} - E_n^{(0)}} \left|n^{(0)}\right\rangle$$

Higher orders term will also involve higher powers of the electric field and so for *linear* dipole polarizability we must stop here. It has been shown **[11, 4, 51]** that for the $J = \frac{1}{2}$ ground state of alkali atoms, the scalar polarizability is not dependent on the hyperfine state quantum number F and that the tensor polarizability is identically zero, unless the hyperfine interaction is included in the perturbing Hamiltonian, only then a hyperfine state dependent scalar polarizability arises $\alpha_S(F)$ and the previously "forbidden tensor polarizability" obtains a small but finite value, $\alpha_T(F, m_F)$. The shift of a level due to a static electric field then takes the form

$$\Delta E_{F,m_F} = -\frac{1}{2}\alpha_S(F)E^2 - \frac{1}{4}\alpha_T \frac{3m_F^3 - F(F+1)}{F(2F-1)}(3E_z^2 - E^2).$$

The numerical values for the different polarizabilities can be calculated using advanced numerical methods and predictions were given as early as the 60s' of the previous century. The main difficulty is that in order to evaluate the electric polarizability of an atom the electronic wavefunctions must be known to great accuracy - impossible for all atoms except the very simple ones like Hydrogen and maybe Helium. Therefore theoretical advances were slow and meaningful predictions were not available until the late 60's [11].

In recent years the subject of atomic polarizabilities has seen a renewed interest. First, the continuous advancement in the accuracy and stability of atomic clocks has has reached a point in which the shift in the clock transition freqeuncy due to the electric field of the omnipresent black body radiation is measuremable and affecting the performance of the atomic clock. This shift is only affected by the scalar differential polarizability because

of the isotropic nature of the BBR. Because of the special role of Cs as the atomic clock primary standard and the definition of the second by the hyperfine transition frequency of Cs it has gained much attention and its scalar polarizability was measured in recent experiments **[44]**. For the purpose of predicting the BBR shift the tensor polarizability plays no role, but as it is always present in experiments involving static linear fields, it must also be known in order to take its effect into account. This motivated the experiments in [33] that measured the so called "forbidden tensor polarizability", and also discovered a 40 year old error in the theory made up by Sandars in 1968 [50]. While Cs is expected to retain its role in time keeping standards for years to come, Rb atoms has also a special role as a secondary time standard. Its scalar polarizability has been measured in some atomic beam experiments back in the early 70's and some measurements of the F=2 hyperfine state tensor polarizability were also made around that period **[15, 30]**. Recently a theoretical prediction for the magnitude of the tensor polarizability of several alkali atoms including that of Rb was made by Dzuba, Flambaum and Derevianko [11]. They used a specialized numerical method to calculate the scalar and tensor differential polarizabilities to third order in perturbation theory. As far as we are aware of, ours is the only direct measurement of the *differential* tensor polarizability of the hyperfine clock transition in ^{87}Rb. Our method has allowed us to directly measure the *ratio* between the scalar and tensor shifts, as experienced by atoms trapped in a quasi-electrostatic trap, thereby minimizing errors arising from fluctuations and mis-calibration of the applied electric field.

Finally, the role of the vector polarizability should be briefly mentioned. As have been demonstrated by Porto and in a different experiment by Kuzmich **[28, 10]** it is possible to use the dependence of the vector part of the polarizability on the quantizing magnetic field, as well on the polarization of the applied radiation, to tune the total polarizability such that the differential polarizability of certain clock transitions vanish. By applying a large magnetic field and using circularly polarized light Kuzmich and friends has demonstrated long coherence times in atoms trapped in a lattice that would otherwise have suffered large inhomogeneous broadening. The phenomena was explained in an article by Derevianko [9].

3 The Setup

Our system is a cold atoms experiment housed in a single vacuum chamber. ^{87}Rb atoms are introduced into the chamber by commercial (Alvatec) isotope enriched (98%), dispensers, heated by a current of 3.6A. We can momentarily increase the Rb partial pressure in the chamber, approximately by a factor of 10, by exposing it to light emitted from violet (405nm) LEDs (Epitex Inc, L405-66-60-110) **[2]**, seen in Fig.8b. The atoms are collected and cooled in a six-beam magneto optical trap (MOT). Each of the MOT beams is delivered by single mode fiber, followed by a half wave plate, a polarizing beam splitter, a quarter wave plate and a $\times 3$ beam expander. We have designed and constructed six identical "projectors" to which the fibers are connected and encloses all the optics in a rigid package, allowing for convenient mounting of the MOT beams close to the chamber. Rather than using six separate fibers to deliver the light to each of the six beams, we use three fiber splitters. Using fiber splitters instead of six separate fibers somewhat simplifies the setup, and by using the two outputs each splitter for a pair of counter-propagating MOT beams, we reduce differential mode intensity noise within a pair. The output beam from each of the projectors is circularly polarized and 22mm in diameter, with about 40mW per beam, and is detuned 18MHz to the red of the F=2$\rightarrow$F'=3 transition (tagged levels F' will always indicates levels belonging to the $P_{\frac{3}{2}}$ excited state hyperfine manifold, while untagged levels F indicates levels belonging to the ground state $S_{\frac{1}{2}}$ hyperfine manifold). The light for the MOT which is generated by a tapered amplifier, seeded with a homebuilt laser module (cooling laser), based on an Eagleyard DFB diode laser. The cooling laser is offset locked to a second (master) laser, in turn locked to the F=2$\rightarrow$F'=3 transition by absorption spectroscopy in a pump-probe scheme in which the pump frequency is modulated by an AO modulator in the servo loop. A second laser, similarly locked to the F=1$\rightarrow$F'=2 transition provides about 10mW repumping light for the atoms.

A magnetic gradient of 10G/cm for the operation of the MOT is provided by a pair of air-cooled coils, each of 200 turns driven with 3.6A of electrical current.

After being cooled in the MOT some of the atoms are transferred into the quasi-electrostatic trap (QUEST) formed by a CO_2 beam, tightly focused to a waist of approximately 30μm by a 38.1mm intra-vacuum aspherical lens. The loading of the QUEST is

accomplished by ramping down the cooling and repump power and increasing the detuning of the cooling beams from 18MHz during the MOT phase to 70-120 MHz, depending on the conditions. This transient loading stage lasts about 40ms after which the 780nm lasers are shut-off, and we end up with up to 5×10^5 optically trapped atoms at a temperature of approximately 100μK, measured 50ms after loading and for a trapping laser power of 14W. Both the temperature and the number of atoms found in the trap after loading is highly dependent on the trap power and its waist. For most of the experiments we use much lower power for our trapping beam and we typically allow for 2-3s of self evaporation, ending up with 40,000 atoms at 30μK, for a trap beam power of 3W.

We have three pairs of magnetic coils that are used to compensate the bias magnetic field at the position of the atoms as well as to apply a magnetic bias in any direction and at field amplitude of up to 1G. The current through the coils is PID controlled by a National Instruments 7852R FPGA card, which also provides the locking for the various lasers and controls the experimental sequence at the micro-second level. In Fig. 8a the vacuum chamber, as well as the MOT beams projectors, magnetic compensation coils and the imaging system are seen.

It should be noted that this setup was not built as a standalone experimental apparatus, but rather as a part of a much more complex "atom-ion-hybrid" system. During its design many constraints that had to do with the future system were taken into consideration, causing several aspects of the system to be less than optimal for the purpose of the experiments described below, including the positioning of the system itself, the relatively long distance between the imaging optics and the atoms etc.

In the following paragraphs several technical details regarding some of the more important subsystems in the experimental setup will be outlined.

3.1 Vacuum system

Vacuum-wise the project has definitely began on the left foot with the unfortunate consequence of short trap lifetime on the order of one second. To further complicate things, our ^{87}Rb dispensers were casualties to a bizarre accident involving a defective (demonic?) current supply, leaving them all but empty, and the cell sputtered with Rb. We managed to

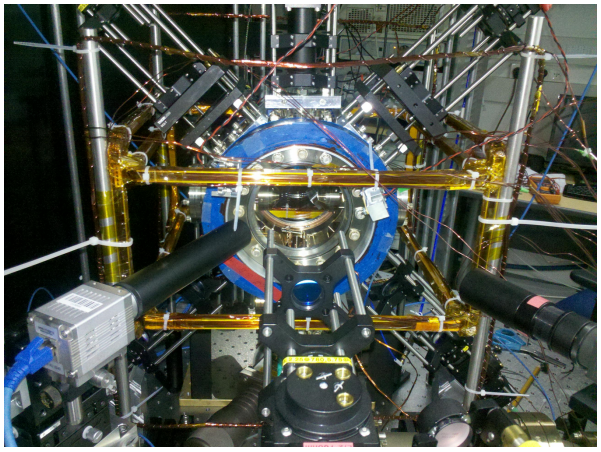

(a)

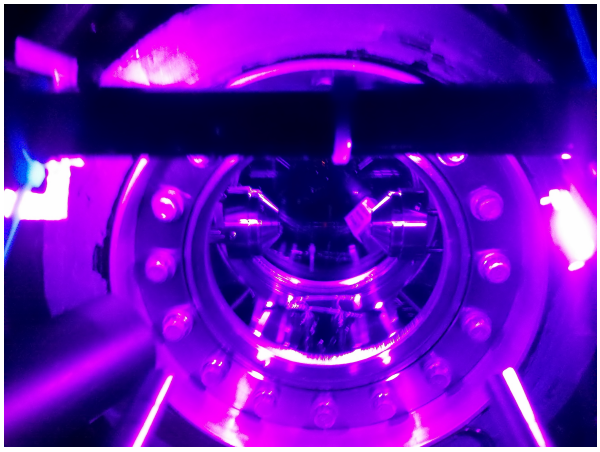

(b)

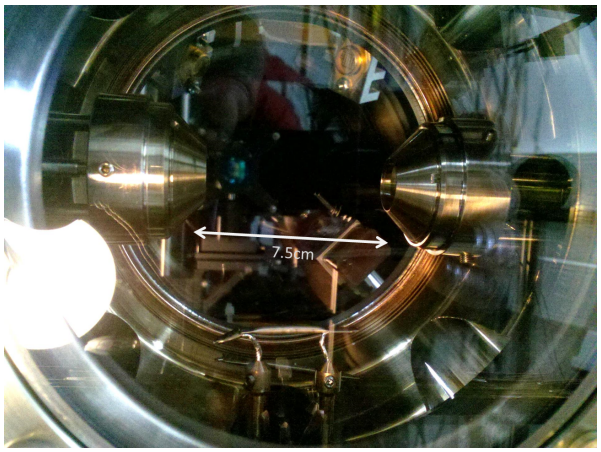

(c)

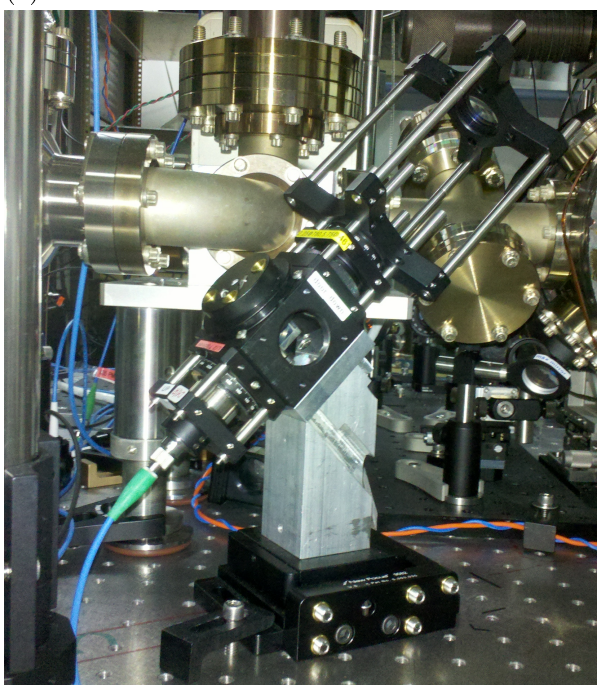

(d)

Figure 8: **(a)** experimental setup. shown are the vacuum chamber, magnetic compensation coils (blue), intra-vacuum ZnSe lens holders (conical), MOT beam projectors, imaging system, MOT gradient coils (blue)
(b) close-up during a UV LED pulse. A MOT cloud is vaguely showing midway between the intra-vacuum lenses. **(c)** The internals of the vacuum chamber, as seen through the CF6 window. **(d)** one of the MOT beam "projectors". A single mode optical fiber is connected to a wide beam collimator, followed by a $\lambda/2$ plate, PBS, $\lambda/4$ and a $\times 3$ beam expander. An iris located before the beam expander can be used for alignment purposes.

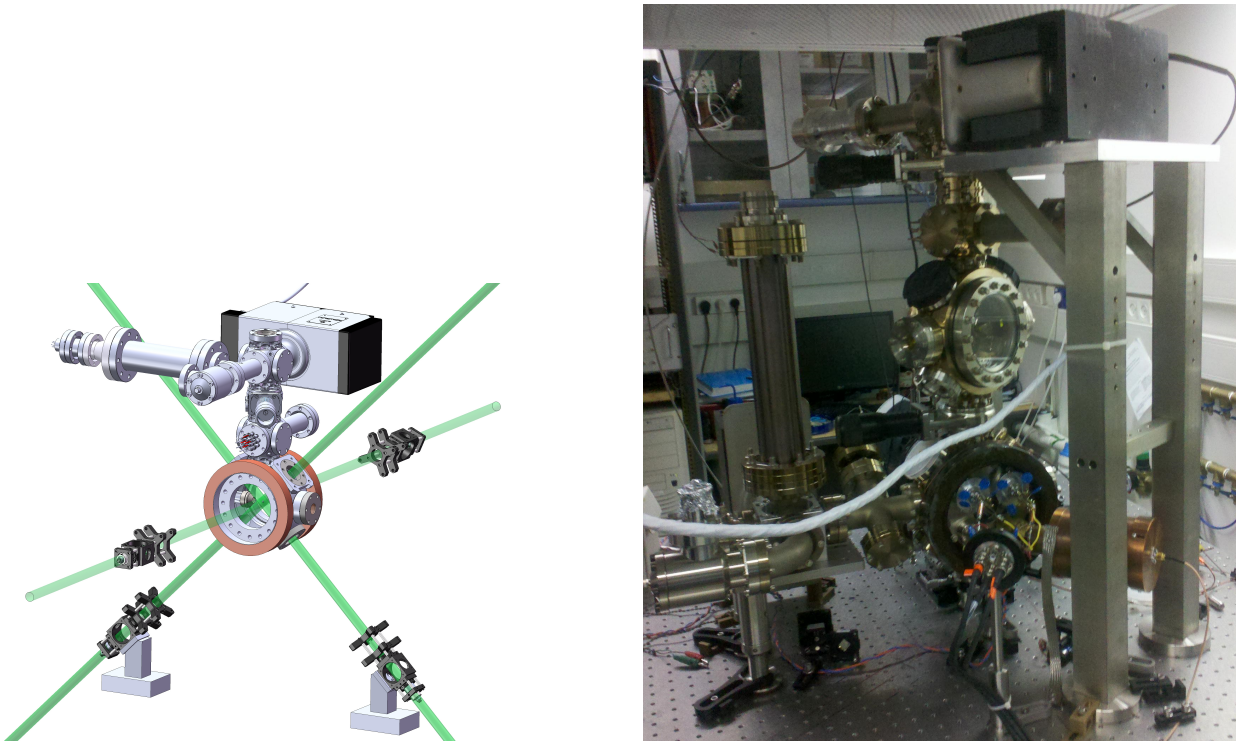

(a) (b)

Figure 9: **(a)** The vacuum system was designed in Solidworks **(b)** And here is the completed system - assembled for the first time in January 2014

continue to work and improved our laser cooling setup, implemented dipole trapping and MW spectroscopy, but after a year of fighting the inevitable we decided to break vacuum and bring the system back to full working order. Upon opening the cell we discovered the intravacuum lenses coated with an opaque material which we presume was a thin film of Rb turned opaque after having reacted with the outside atmosphere. The cause for the originally bad vacuum conditions were not apparent. We discovered at least one UHV design error: the intravacuum lens holders, machined inhouse, were made of ST303 "readily machinable stainless steel" , which is not UHV compatible due to its high content of sulfur. One should better use ST304 or ST316 which are harder to machine but are better compatible to ultra high vacuum (and also much less magnetic). Looking for the main cause of bad vacuum was a real ordeal. We could not find an obvious leak (the vacuum wasn't actually that bad at $< 10^{-9}$ torr. just not good enough) so we took the approach of "lion in the desert", and conducted repeated bakeouts each time with different parts of the system. Only after several bakeouts we could find a subset of the system that could go to $< 10^{-10}$ torr, and we started building up from there. This took months. The finished system was much improved compared to the original, and included a titanium sublimation pump which was missing from the original design, improved vacuum conductivity from the science chamber to the pumps and a bigger ion pump. In order to simplify the design we gave up the possibility of moving the intra-vacuum lenses (originally implemented using flexible bellows which are prone to leaks if not handled delicately enough) and instead connected the lens holders to the chamber in a rigid way. The completed vacuum system can be seen in Figs.8,9.

After the aforementioned rehauling of the system we began to enjoy favorable vacuum conditions and long trap lifetimes, in excess of 30s, see Fig.10. The vacuum system is based on a stainless steel spherical octagon chamber from Kimball physics. It is pumped by a combination of a 40l/s starcell ion pump from Varian (now part of Agilent) and a titanium sublimation pump, also from Varian. We were able to reach UHV conditions, with pressure lower than $< 10^{-10}$ torr, as measured by an integrated Bayerd-Alpart vacuum gauge. It should be mentioned that one of the weak points of using a 10μm laser for the trapping beam is that you have to use ZnSe viewports, which have a rated bakeout temperature of 150°C only, limiting the quality of the vacuum that can be achieved. Also, as we

discovered, these viewports are much more prone to developing leaks. Of four viewports we tested, three were proved to be leaky to some extent. Luckily we were able to seal the leak we have found after the final bakeout using vac-seal, a special vacuum compatible glue. Maybe using windows made of harder material, e.g. silicon, would have been better with respect to vacuum performance, but the fact that ZnSe is transparent for visible light does make it easier when aligning the trap beam with the MOT.

It is worth mentioning that the vacuum in the chamber has improved by a factor of 3 during the year following the bakeout. We are not sure what is the cause but among the possibilities are long curing of the vac-seal (which can take months in room temperature), a virtual leak created inadvertently when applying the vac seal, outgassing from the (heated) Rb dispensers that naturally decreased after prolonged use or even the bakeout effect of the mild, year long, heating of the chamber caused by the MOT coils directly attached to it (they run at $\approx 50°$C). The lesson from this is that bakeout is not the end of the story and vacuum conditions are likely to improve over time (provided there's no hole in the bucket!).

3.2 780nm laser system

Laser light resonant, or nearly resonant, with the D2 transition of ^{87}Rb is used for many purposes in the experiment, such as laser cooling, magneto optical trapping, optical pumping and imaging. We use three homebuilt lasers, designed around a distributed feedback laser diode (DFB) from Eagleyard and locked to various transitions of the ^{87}Rb atoms. A DFB laser is a solid state device in which the active gain region is periodically structured to enable the back reflection of only a small band of optical wavelength (Bragg reflection). This in contrast with ordinary laser diode in which the optical feedback is achieved by reflection from the end facet of the diode, and is broad band, thereby necessitating the introduction of an external cavity. Commonly done by adding a grating in the Littrow configuration, where the first order of refraction is fed-back into the diode. By creating a Bragg reflector in the diode it is possible to maintain a stable and predictable lasing at a single frequency with a relatively (compared with extended cavity diode lasers) large mode-hop free region, making tuning of the laser quite easy. Another advantage of this

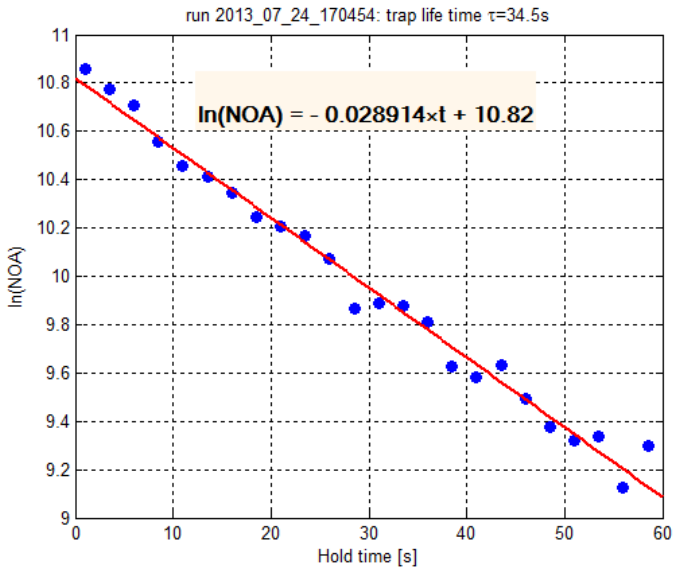

Figure 10: Background limited trap lifetime, shown in natural logarithmic scale for convenience. For F=1 atoms the trap lifetime is well over 30s. Vacuum is no longer an issue.

design is an inherent immunity to acoustic vibration, since the cavity and the gain medium are monolithic. The lasing frequency of a DFB laser can be controlled either by manipulating the temperature of the device, usually by a TEC, or by controlling the electrical current into the junction. For the devices we use, Eagleyard EYP-DFB-0780-00080-1500-TOC03-000x, $d\lambda/dT = 0.06\frac{\mathrm{nm}}{\mathrm{K}}$ and $d\lambda/dI = 0.003\frac{\mathrm{nm}}{\mathrm{mA}}$. There is however a price to pay, and the short cavity of a DFB laser of only about a millimeter (1.5mm for the model we use) results in a larger linewidth; we measure 2.8MHz using the beat between two identical lasers (the beat signal 3dB width as measured on a electronic spectrum analyzer is 4MHz), wide compared to the linewidth of an ECDL, typically below 1MHz. In this section we describe in detail the design of the lasers and the locking techniques used to keep them at the desired optical frequencies.

3.2.1 The master (reference) laser

This laser, tuned midway between the F=2→F'=3 and F=2→F'=2 transitions fulfills two functions. Firstly, it is used to provide a reference frequency to the cooling laser which is described in a following section. Secondly, some of its light is shifted in frequency by an acousto-optical modulator in a double pass configuration close to the F=2→F'=1 transition and used in a "depumping" beam that can be used to pump the atoms out of the F=2 ground state and into the F=1.

We lock the laser to an atomic line by the method of saturation absorption spectroscopy. The pump beam passes through an acousto optic in a double-pass configuration and this result in a shift of 133MHz of the laser frequency with respect to the locking point, half the separation between the F=2→F'=3 and the F=2→F'=2 transitions. The AO is driven by a VCO operating at 133MHz and frequency modulated at ≈80kHz by signal digitally synthesized by the FPGA controlling the experiment. The detected saturation absorption signal is modulated as a result, but after being mixed digitally in the FPGA with the original 80kHz reference and digitally filtered we end up with a dispersive error signal, zeroed around the absorption peak that enable the feedback to lock the laser to the transition, Fig.11. This method is highly resilient to low frequency noise since the demodulated base-band signal exist only as a digital representation within the FGPA, and

therefore is not subject to analog noise sources, as it would be if the demodulation was done by analog electronics. By modulating only the pump beam we eliminate unwanted residual intensity modulation on the laser that would otherwise be present at the laser output.

3.2.2 The slave (cooling) laser

This laser consists of a DFB which is amplified by a tapered amplifier (TPA), both from Eagleyard. The TPA (EYP-TPA-0780-01000-3006-CMT03-0000) provides approximately 1W of optical power, which is then double-passed through a AO operating at 133MHz. The 1^{st} order of refraction is divided into three by polarization beam splitters and halfwave plates and injected into the three fiber splitters which carry the light for the six laser cooling beams. We use the $\lambda/2$ plates to adjust the relative power in the MOT beams so that they are equal. The 0^{th} order is double passed through a second AO and used for detection of the atoms in the absorption imaging setup. Both AO's are intended to be used merely as fast switches, and so are driven at the same frequency which is kept constant throughout the experiment. Instead of using the AO drive frequency to control the frequency of the laser beams, we rely on an offset locking scheme to accomplish this task, with the benefit of much larger frequency span available to the laser (up to 400MHz).

Light from the master laser (< 1mW) is overlapped with fraction of the light from the slave laser (≈ 0.5mW), picked off by a single sided AR coated window placed before the TPA. The optical intensity on the detector is $I \propto |E_m(t) + E_s(t)|^2 = |E_m|^2 + |E_s|^2 + 2E_m E_s$, and with $E(t) \sim E\cos(\omega t)$ the instantaneous intensity has a DC component which is the combined intensity of the two beams, a component oscillating at twice the optical frequency, which cannot be detected by (any) electronics, and a component oscillating at the difference frequency $\Delta\omega = \omega_m - \omega_s$. Actually it is only $|\Delta\omega|$ that is detected, but by increasing (or decreasing) the frequency of the slave laser and monitoring the direction in which $\Delta\omega$ changes we can also determine the sign. In practice this happens automatically by setting the sign of the error signal in a feedback loop. The resulting beat signal is detected by a fast photodiode, reversed biased by a 18V from a couple of 9V batteries, and amplified by a preamp and then a RF amplifier to obtain a signal of a few 100mV

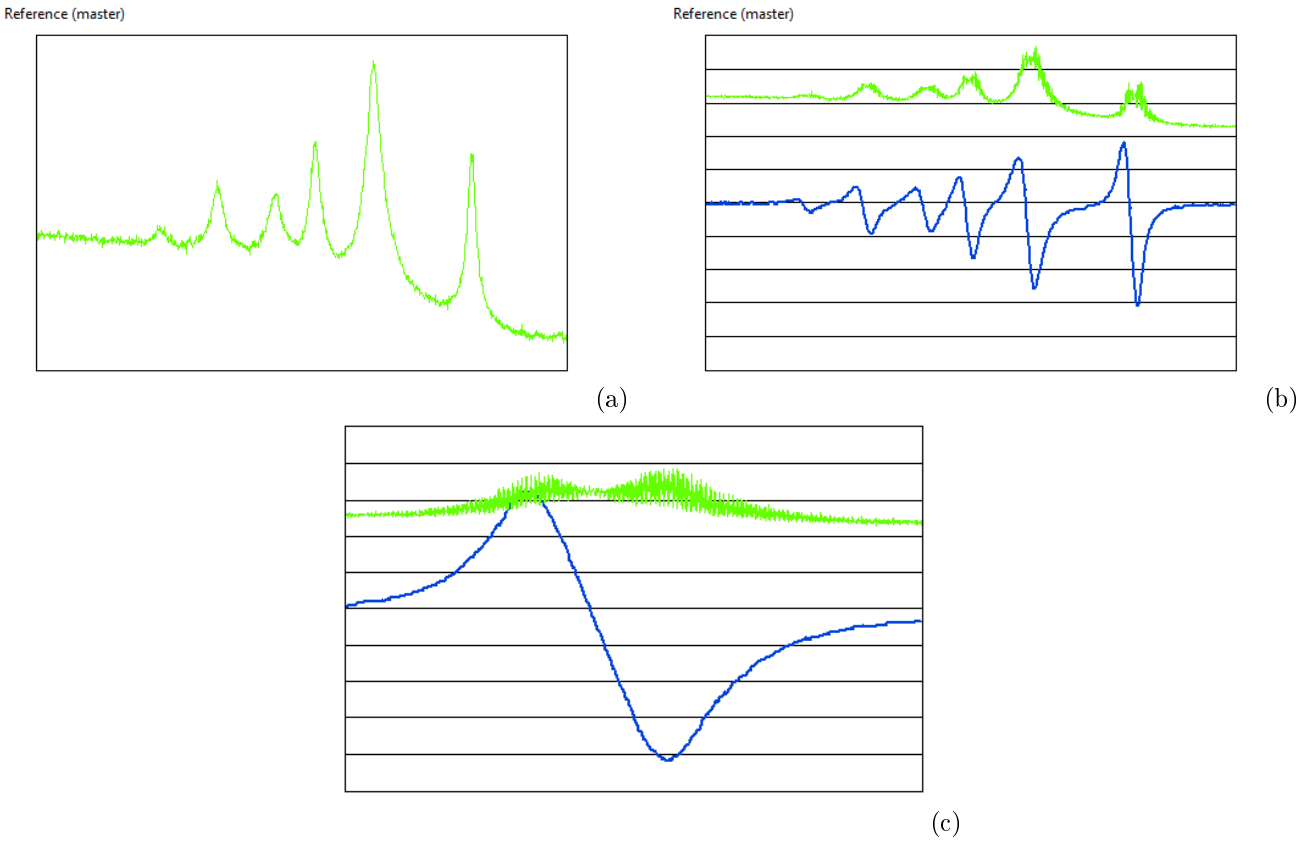

Figure 11: (a) Dopler-free saturation-absorption spectroscopy of the F=2→F' lines ("cooling lines") . During normal operation the laser is locked to the F=2→F'=3 line, which is the rightmost peak in the figure. (b) On top is the raw, modulated, saturation - absorption spectrum. Note that around the peaks the modulation, appearing a as thickening of the line in the figure, is minimal (zommed-in scan in (c)). On the bottom of the figure is the demodulated signal obtained by digitally mixing the signal on the top with the local oscillator and filtering the resulting waveform with a digital low pass signal. The laser can be locked to any of the zero crossings that now corresponds to the centers of the spectral peaks.

amplitude. This signal is filtered by a RF low-pass filter to reduce unwanted spurius pick up signals and is then input to an EVAL-ADF4113 (Analog Devices), configured as a fast cyclic counter of period 500, which is able to operate up to ≈400MHz. Each time the counter reaches a count of 500 cycles of the beat signal it outputs a TTL signal of about 5ns duration, too short for the FPGA to detect with high fidelity. We use a DS1040M-100 (a simple programmable one-shot pulse generator) to increase the pulse duration to about 40ns which is reliably detected by the FPGA. A second counter operating at 80MHz is implemented digitally in the FPGA and is reset at each TTL received from the external fast counter. The value of the internal counter at the moment of reset is a measurement of the period of the beat signal. The FPGA then uses the difference between the measured period and a reference period (set-point) as an error signal for controlling the slave laser. When monitored on an electronic spectrum analyzer the beat signal is found to be 4MHz wide (3dB points) which indicates that each of the DFB lasers has a 3dB linewidth of 2.8MHz, assuming they are identical, see Fig.13.

This electronic locking scheme has many benefits. It is very stable and the laser remains locked for weeks at a time. It allows for a large tuning range for the slave laser, up to 400MHz was achieved reliably, which is hard to achieve with other means such as AO frequency shifters. While response isn't as fast as could be obtained with a AO shifter, we can still achieve frequency jumps of 100MHz with a transient time of < 0.5ms, see Fig**.14**. It is also possible to change the direction of the relative detunings from red to blue by simply inverting the sign of the error signal in the digital feedback loop. While electronic offset locking schemes were demonstrated before [36, 46, 21], our implementation, relies on a modified evaluation board of a commercial PLL device and an NI FPGA card for all digital control, does not require any expertize in fast electronics, and could be readily implemented in similar setups.

3.2.3 Repump laser

The repump laser is built similarly to the reference laser with some exceptions. It is locked to the F=1→F'=2 transition by a similar lock-in method, however, for this laser, it is the drive current that is modulated to create the lock-in signal which results in small

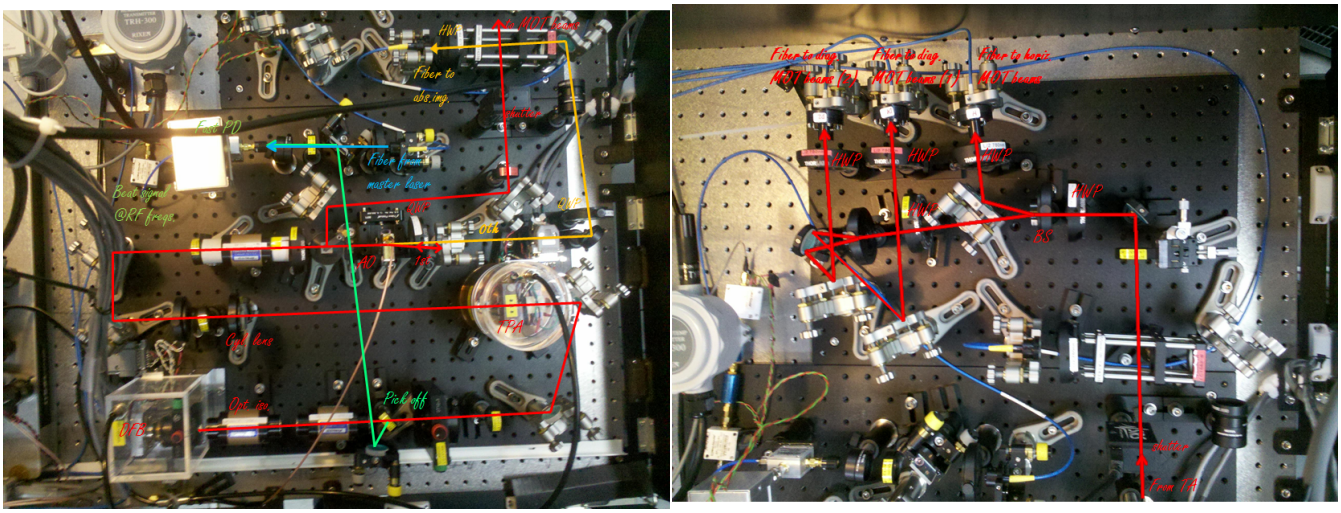

(a) (b)

Figure 12: (a) Cooling laser line. (b) Cooling laser coupling into three fibers

frequency and intensity modulation of the laser output. This modulation in the repump laser parameters has little effect on the experiment (a fast, 80kHz noise on the florescence signal from the atoms, naturally averages out in most measurements), however, it may be worthwhile to improve the locking scheme by including an AO in the loop, similar to whats done in the master laser setup.

3.3 Magneto Optical Trap

Loading of an optical trap, the typical depth of which is only a few mK at best, requires cooling of the atoms. Additionally, the small trapping volume of such traps (for reasonable laser powers), demands high densities of the cold gas. It is therefore essential to have a cold and dense reservoir of atoms from which to load the trap. A mageto-optical-trap (MOT), a common tool of atom physics, provides just that, with typically T $\approx 150\,\mu$K and $n \approx 10^{11}\,\mathrm{cm}^{-3}$.

The cooling light, detuned 18MHz red of resonance with the F=2→F'=3 transition is produced by DFB laser diode and then amplified by a tapered amplifier and delivered to the chamber using three polarization maintaining fiber splitters, each has one "pigtailed"

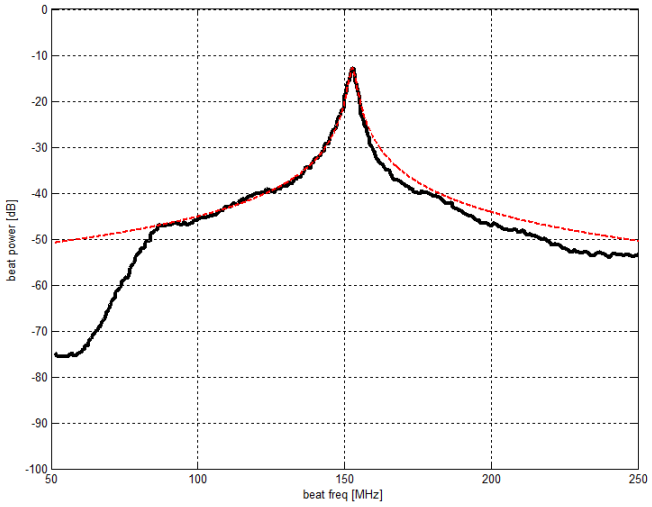

Figure 13: The beat signal between the master and slave lasers, as measured on an electronic spectrum analyzer. Raw data in black showing the beat signal, the noise floor and the effect of the RF filter as a cut around 70MHz. In dashed red line is a Lorentzian fit $y(f) = \frac{A}{(f-f_0)^2+\left(\frac{FWHM}{2}\right)^2}$ to the spectral peak. The FWHM as extracted from the fit is 2.55 MHz with a 95% confidence interval of 70 kHz. This FWHM is in terms of electrical, not optical power. The linewidth of each of the beating lasers, assuming they are identical, is $2.55\,\mathrm{MHz}/\sqrt{2} \approx 1.8\,\mathrm{MHz}$.

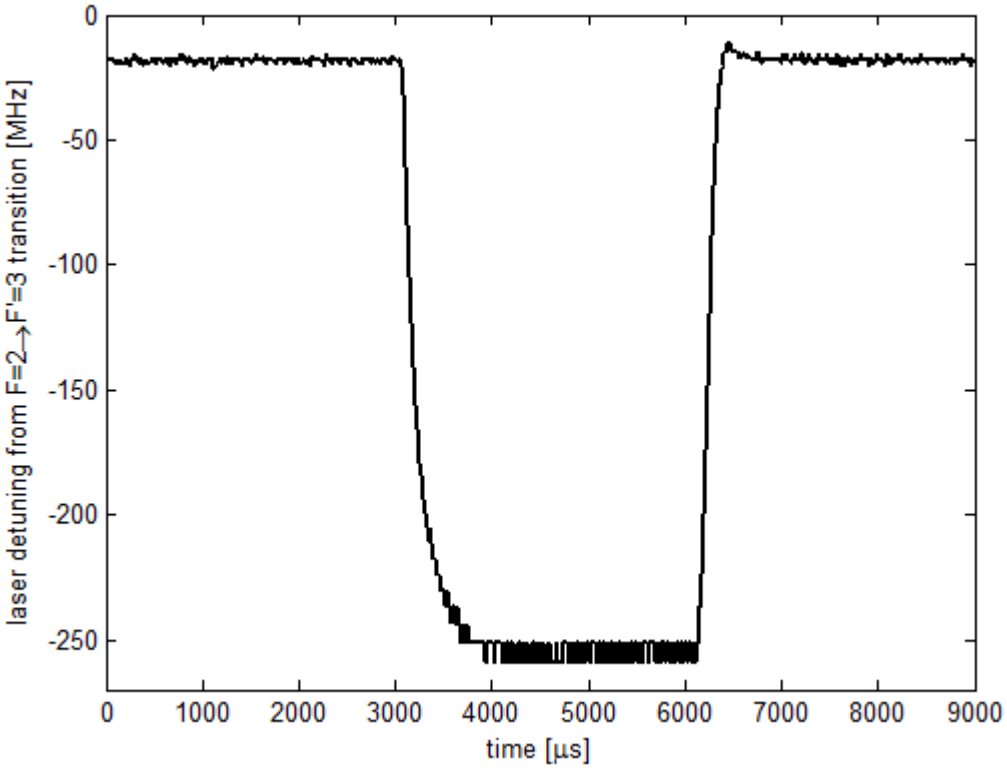

Figure 14: Transient performance of the offset locking controlling the frequency of the cooling laser. Initially the laser is locked at its normal MOT operation frequency, detuned 18MHz from the cooling transition. Then it is shifted by 237MHz to a detuning of 255MHz, and brought back after 2ms. The first transient in the down direction is completed in 700μs and the second transient in the up direction is even faster, with only 300μs. These are limited by the transfer function, implemented digitally, of the control loop, not by the electronics of the laser, and could be made faster with some effort.

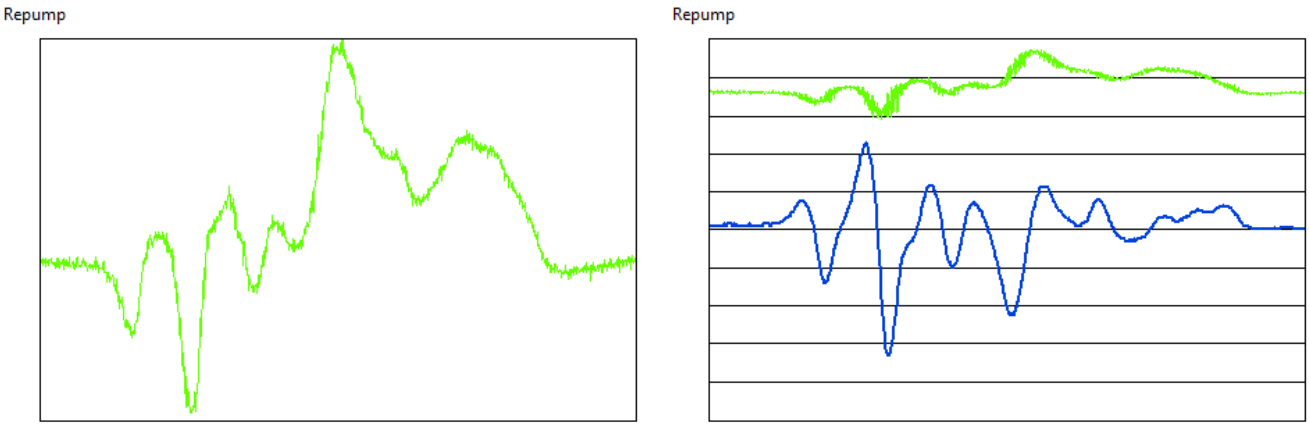

(a) (b)

Figure 15: **(a)** Doppler-free saturation-absorption spectroscopy of the F=1→F' lines ("repump lines"). **(b)** On top is the raw, modulated, saturation - absorption spectrum. On the bottom of the figure is the demodulated signal. There seems to be way too many lines in the spectrum (ten instead of six) but this due to a technicality: the Rb reference vapor cell was placed too close to the optical isolator with its high magnetic field. This naturally causes Zeeman splitting and deformation of the spectral lines. However, this effect is constant in time and so once a locking point is chosen for the laser and the driving frequency of the acousto optic switch is calibrated accordingly, there are no consequences to this, rather annoying, disturbance. It is nice to note that the modulation scheme implemented for locking to a peak center (rather than side of peak), also has the added benefit of reducing the noise due to its inherent lock-in mechanism, and indeed, the multiple lines, that are hardly visible in the non modulated saturation absorption signal, become pronounced features in the demodulated one.

(a) (b)

Figure 16: **(a)** master (reference) laser setup. In red are the beams relevant to the locking scheme, blue is a beam directed to provide a reference to the offset locking of the cooling laser, in green is a portion of the laser acting as a depumper, tuned to the F=2→F'=1 transition, and delivered to the atoms by an single mode optical fiber. **(b)** photograph of the same setup, including the repump laser.

input port and the output is divided equally between two FC/APC ports. The output ports of the fibers are connected to specially built "projectors": a rigidly constructed optical setup that outputs a wide (22mm) beam of the correct circular polarization for each beam the MOT. These projectors can be placed close to the chamber windows and thus reduces instabilities caused by beam pointing, and add to the robustness of the system in whole. One of the MOT beam projectors is shown in Fig.8d. A separate single mode fiber terminated by a wide beam collimator followed by a beam expander (22mm diameter beam at output) delivers about 10mW of repumping light to the atoms.

The magnetic field gradient of 10G/cm required for a Rb MOT is created by a pair of air cooled coils of 200 windings, directly attached to the vacuum chamber, approximately in an anti-Helmholtz configuration. The coils are connected in series to reject differential current fluctuations and are driven by a A8002 power supply from Agilent. The current to the MOT coils is fed through a MOSFET, and can be switched on and off by applying the appropriate TTL signal from the FGPA card controlling the experiment. While the current is shut off within 300us, the magnetic field itself takes longer to vanish because of eddie currents in our metallic vacuum chamber.

The number of atoms in the MOT saturates at a $10 - 30 \times 10^6$ atoms after $\approx$15s of loading, but these numbers are very sensitive to the exact conditions in which the MOT is operated and should only be taken as representative. The numbers of atoms in the MOT can be increased by approximately an order of magnitude by turning on, during the loading phase, an array of six light emitting diodes operating at 405nm, which are placed close to the chamber windows and are positioned to best illuminate the large 6CF windows and the stainless steel walls of the cells. While this is a valuable tool for experiments requiring large numbers of trapped atoms, we did not make much use of this technique. With prolonged operation of the violet LEDs depletion of this source of Rb is observed, causing the number of atoms to drop from one run to the next. While it does saturates to a value larger than what can be achieved without using the LEDs, the time it takes for saturation, and the terminal value depends on the duty cycle in which the experiment is being run, therefore this method could not be used in many of our experiments which had the opposite demands, i.e. for low density samples with high shot-to-shot stability in the number of trapped atoms.

3.4 Optical (quasi electrostatic) trap

The trap is formed using a single beam of a CO_2 laser, tightly focused using a f=1.5" aspherical lens, placed inside the vacuum chamber. The beam is then recollimated by an identical lens, exits the vacuum cell through a second ZnSe viewport and directed into a beam dump. The laser intensity is controlled using an acousto optical modulator driven with about 25W of RF power at 40MHz. Since almost all of the RF power is absorbed in the AO crystal there are thermal effects that cause beam pointing and also transmission efficiency issues. We were able to greatly reduce these thermal effects by driving the AO simultaneously with two RF frequencies, f_1 =30MHz and f_2 =40MHz, while keeping the total power constant ($P_{total} = P_{f_1} + P_{f_2} = const.$), similarly to [14, 13]. This is achieved by using an analog feedback loop on the total RF power injected into the AO: the amplified RF signal power is measured using a home built device and is used as an input to a commercial PI controller (Precision Photonics). The control signal is used to feedback on the power of the 30MHz (RF2) signal to keep the total amplified RF power constant. The diffraction order resulting from the auxiliary RF drive is separated by a mirror and directed into a water-cooled beam dump. This is similar to what is done in [14, 13], however their implementation was by feed forward rather than feed back. To control the optical power in the trapping beam we use a second feedback loop, digitally implemented by FPGA: the first diffracted order from the AO is sampled using the <1% transmission through a 99% mirror which is then focused on a fast photo detector (Vigo PVM 10.6). The PD amplified output (Boston Electronics 481-1X fast amplifier, 1MHz bandwidth) is used to actively feed-back and control of the CO_2 laser power used in the experiments by changing the RF power at the primary frequency that is driving the AO. A schematic of the CO_2 laser beam line is given in Fig.18.

Initial alignment of the trap was aided by increasing the MOT, either by using a higher current in the dispensers or by using the light-assisted desorption scheme. With the MOT highly visible it was easy to observe it from the ZnSe ports and through the intra-vacuum ZnSe lenses. Because of the slightly shorter focal length of the lens at 780nm compared with their design wavelength of 10.6μm ($f_{780\text{nm}} = \frac{n_{@10.6\mu\text{m}}-1}{n_{@780\text{nm}}-1} f_{10.6\mu\text{m}} = n = \frac{2.40266-1}{2.52906-1} 38.1\text{mm} = 34.95\text{mm}$) an image of the MOT is created outside of the vacuum

chamber, on the optical axis of the intravacuum lens, at a distance $d \approx 423$mm from the lens, calculated using the lens equation $\frac{1}{d} = \frac{1}{f_{780\mathrm{nm}}} - \frac{1}{f_{10.6\mu\mathrm{m}}}$, assuming the lens is positioned such that the trapping beam at 10μm is focused at the MOT. With the help of a CCD we are able to place an iris around the image of the MOT. The initial alignment is completed by passing the CO_2 beam through the iris and perpendicular to the ZnSe window (verified by looking at the reflection of the overlapping trace beam from a HeNe laser). This procedure is almost guaranteed to end with a detectable amount of atoms in the trap, which is then maximized by further adjustments to the beam and the MOT position. Since our intra-vacuum lenses are fixed (they were adjustable in the original design, but the flexible bellows that were used were suspected to be leaky and were retired) we are not able to move them so that the MOT is at the focus. However, it is straight forward to move the MOT by changing the magnetic bias field during the loading time (the dark MOT phase), so that the magnetic zero (bias+gradient) is at a position that maximizes the loading into the trap. We then remove the excessive bias after the loading is done to work at zero magnetic field conditions (or at some other predetermined bias, see section 4). This procedure does have its drawbacks since cooling schemes that rely on zero magnetic fields, such as PGC, cannot be used (or rather, can only be used provided that the "loading" magnetic biased is returned to zero quickly after loading is done), nevertheless, these are generally unnecessary when working with a CO_2 trap, as exemplified in a similar CO_2 setup mentioned in [14] where a CO_2 trap was loaded at a bias field of 1G.

The loading of MOT atoms into the optical trap is done as follows. The trap beam is turned on together with the MOT and is kept on during the accumulation phase of atoms in the MOT. A depumper beam, which is detuned with respect to free atoms, but resonant with atoms experiencing the stark shift of the S-P transition caused by the trap beam, is turned on to pump trapped atoms into the F=1 ground state. In parallel we go into a brief (50ms) dark MOT phase in which the detuning of the cooling beams is ramped to 70MHz red of the cooling transition (compared with a detuning of 18MHz during the MOT collection phase) and the intensity of both the cooling and the repumper beams is ramped down. During the dark MOT phase the radiation pressure pushing the atoms apart is greatly reduced and so the cloud collapses towards the magnetic field zero. We therefore shift the zero field point to the position of the optical trap to optimize the loading by

introducing a magnetic bias field during the loading stage, Fig.17. At the end of this stage all cooling and pumping beams are extinguished by both AO switches and mechanical shutters, and the magnetic field gradient of the MOT is turned off. The remaining atoms are now trapped solely due to the potential of the focused CO_2 beam.

We have confirmed that the lifetime of trapped atoms depends on the hyperfine state they occupy as we see much shorter lifetimes for the F=2 state than for the F=1 state, Fig. 21. This behavior is density dependent and has to do with inelastic, hyperfine changing, collisions between F=2 atoms (the energy released in such an event is $\approx 300\,\mathrm{mK}$, much larger than the trap depth). Because of the short lifetime of the F=2 atoms, it is essential to pump the atoms into the F=1 ground state and make sure no resonant stray light is present that may redistribute the atoms back between the hyperfine states [8]. We have found that we need to completely mask the vacuum chamber from stray photons from the 780nm lasers using large, blackened aluminum plates (curtains would have worked just as well, but we are concerned by the high power CO_2 trapping laser). Under these conditions the lifetime of trapped atoms was background gas dependent at slightly over 30s.

We have found that by shining a weak depumping beam on the F=2 to F'=1 transition, tuned such that only atoms passing close to the trap center are resonant with it (due to light shift induced by the trap itself), we can enhance the loading of the dipole trap, by as much as $\times 3$. The increase in the trapped atom count is due to two independent effects. First, by turning the dipole trap into a "dark spot" - where atoms spend most of their time in the dark F=1 state their density may increase due to reduced radiation pressure they experience (because of rescattered cooling light). This is similar to the increase in density observed in a dark SPOT MOT [23]. Secondly, as already mentioned, trapped atoms in the F=2 state tend to undergo hyperfine changing collision with the unavoidable accompanying loss from the trap. By spectrally selecting trapped (and therefore stark shifted) atoms to be pumped into the F=1 state we reduce the probability for such events, therefore greatly increasing the trapped atoms lifetime and the loading efficiency. This same effect could also be achieved by creating a dark spot in the repump laser and overlapping it with the dipole trap, but it is more effective to actively pump the atoms into the F=1 manifold in the region of interest [3]. We took advantage of the fact that the dipole trap shifts the atoms into resonance with the depumper, making alignment trivial (a weak, wide optical

pumping beam was used). But we could probably benefit from a stronger depumper beam, focused around the dipole trap and optimized with respect to its waist and intensity to maximize the "forced dark spot MOT" effect. By doing that we hope to be able to increase the cold atom density at the region of the dipole trap and therefore the loading efficiency even further.

We are able to measure directly many properties of the trap by using the trapped atoms themselves as probes. We list some of these methods in the following paragraphs. First, the oscillation frequencies of the trapped atoms can be measured by exciting motion in the trap. We did this using two different methods: parametric excitation of the trapped atoms and kicking of the atoms in the trap. In the case of parametric excitation, the trapping beam power was gently ($<10\%$) modulated by applying an amplitude modulation on the RF driving the AO that controlling the CO_2 power, and as a result the trap depth and the trapping frequencies themselves are modulated. The atoms are excited when the modulation frequency matches twice the oscillation frequency of the trap $\omega_m = 2 \times \omega_{trap}$. The trapped atoms are excited into motion with ever increasing amplitude and are eventually lost from the trap, or merely heated if the excitation is weak enough. By sweeping the modulation frequency and repeating the experiment we can map all the resonances of the trap. However, it may be necessary to adapt the modulation amplitude and the duration in different frequency bands. An example of such measurement is given in Fig.19.

In the other method we used, that of kicking the atoms, the scheme is much simpler: the trap is turned off for a short time on the order of 75μs and then turned back on. When the trapping is renewed, the atoms are no longer in their equilibrium position and so they begin to oscillate in the trap. The atoms are finally released from the trap at some time t after recapture and following some convenient TOF both the size of the cloud and its center of mass position are measured by absorption imaging. Since the atoms expand ballistically after this final release it is actually the velocity oscillations of the trapped atoms that are measured, but this is of no significance since only the frequency of the oscillation is of concern. While the trap is off the atoms expand due to their finite temperature by an amount given by $\sigma_e(t) = \sqrt{\frac{kT}{m}}t \approx 4\mu$m, for atoms at 30μK. The radial size of the trapped

atom cloud is $\sigma_r = \sqrt{\frac{kT}{m\omega_r^2}} \approx 6\mu$m and so the radial expansion is significant and oscillations of the trapped atoms in the radial breathing mode are excited. In the axial direction the deformation is negligible since $\sigma_z = \sqrt{\frac{kT}{m\omega_z^2}} \approx 60\mu\text{m} \gg \sigma_e(t)$ and motion in the axial oscillation frequency is hardly excited. During the brief transient release from the trap the atoms also fall by $\frac{1}{2}gt^2 \approx 50$nm, but when comparing this figure to the radial extent of the cloud we did not expect expected to be able to measure the center of mass mode of oscillation, that is excited by shifting the whole cloud relative to its equilibrium position in the trap. From the fact that we actually are able to see a clear signal from this mode of oscillation we gather that probably some extra momentum is imparted on the atoms during the on-off transient. An example of such a measurement, showing oscillations both in COM position and in the cloud size are shown in Fig. 20. A factor of two between the breathing and common mode oscillation is measured, as expected. It is interesting to note that the amplitude of the common mode oscillation as appears in the data is just one pixel, or about 6μm, at the resolution limit of our imaging system. The reason it is still resolvable is that we are not trying to resolve between two objects, but rather to pinpoint the center of one object, a much easier task limited by the signal to noise ratio, not by the optical resolution. For the "kick" type of measurements, only one frequency component is present in the data, belonging to the radial mode of oscillation in the trap. As mentioned above, the appearance of just one frequency component is due to the fact that the axial mode is hardly excited by the kick (the cloud axial expansion is small compared with its extent in this dimension) but also due to the damping time of the oscillations (due to collisions and inharmonicity of the trap) being smaller than the axial oscillation period. Not being able to measure the axial frequency with this method is not a major issue since we can estimate the axial frequency if we know the radial frequency by the relation in Eq.(2), furthermore, since it is the geometric mean frequency $\omega = (\omega_r^2\omega_z)^{\frac{1}{3}}$ that is usually of interest (i.e. in calculating the density) the error in it due to misestimation in the axial frequency is $\frac{\Delta\omega}{\omega} = \frac{1}{3}\frac{\Delta\omega_z}{\omega_z}$.

Another quantity of the optical trap, that can be measured directly using the trapped atoms themselves, is its depth. It is generally true that for any two energy levels in the atom the shift caused by the trap light is different, because the polarizability of different levels is determined by the exact electronic wavefunction of the state. If we are able to

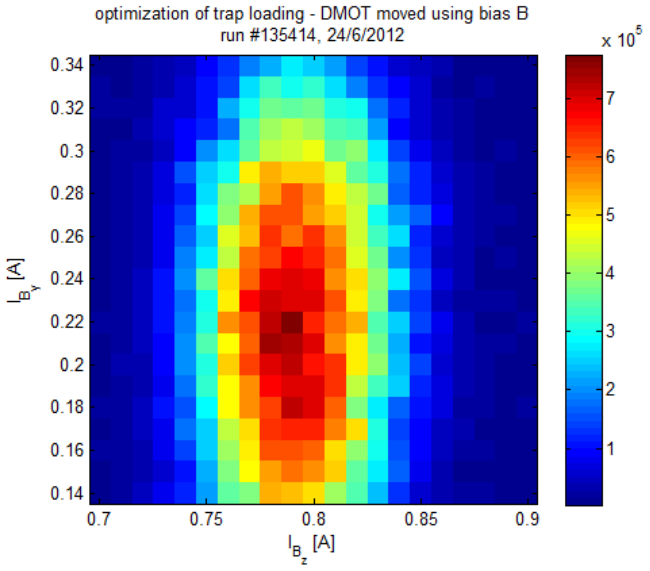

Figure 17: CO_2 trap loading is optimized by moving the zero of the total magnetic field, by changing the bias magnetic field. This is done transiently during the dark MOT phase, to which the CO_2 loading is most sensitive.

measure the frequency of the transition and compare it to the transition frequency of free atoms we can deduce the depth of the trap if the differential polarizability is known. We have performed such measurements both in the optical regime where we measured the shift of the D2 line as function of the trap beam power, and in the MW regime, taking advantage on the differential polarizability between the hyperfine levels of the ground state. More details can be found in the results part of the thesis, in sections 5 and 4.

3.5 Microwave system

Manipulation of the internal state of the trapped atoms using microwave radiation resonant with the hyperfine splitting frequency has been an important tool in this work, and have helped to perform many tasks, including measurement and control of the bias magnetic field, microwave assisted optical pumping into any desired Zeeman state, precision measurements of certain atomic properties and even measured the temperature trapped

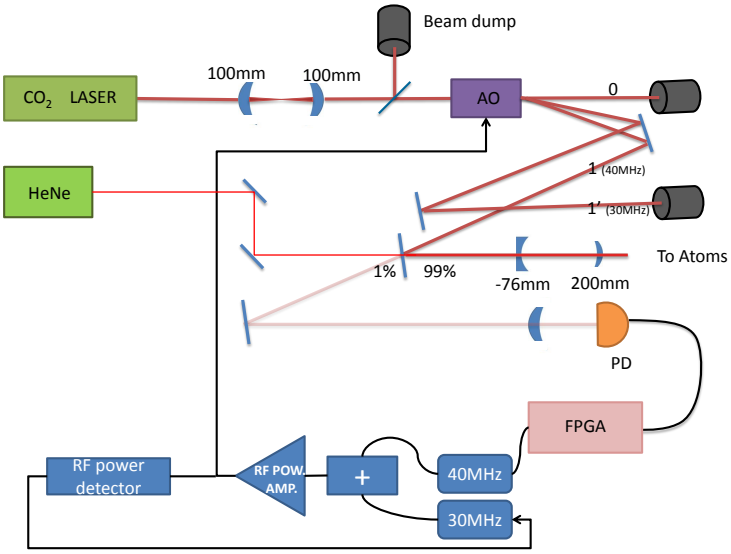

Figure 18: CO_2 laser line

atoms measuring the shape of an inhomogenously broadened line. All of those requires injecting radiation close to the hyperfine transition frequency at 6.8Ghz.

MW radiation is delivered into the chamber by a specially made waveguide antenna, Fig.22. The antenna is terminated by a paraffin spacer that when pressed against the fused silica surface of the viewport ensures better impedance matching and lower reflection of MW radiation from the window. The small dimensions of this antenna allows it to be mounted very close by to the chamber, increasing the field at the location of the atoms. The MW signal is delivered to the antenna by a semi-rigid coaxial cable with low loss from a mini-circuits MW amplifier (ZVE-3W-83+), capable of delivering 3W of power. The amplifier is fed by two separate MW signal generators, combined at the input by a splitter-combiner. The Rabi frequency is directly related to the MW power that is delivered to the atoms by $\Omega \propto \sqrt{P}$ and we are able to measure a Rabi frequency of approximately $2\pi \times 15$kHz, with $t_{\pi/2} = 35\mu s$.

Our main MW source is an Anritsu 68347B which is locked to the 10MHz reference generated at a commercial Rb frequency standard from Stanford Research Systems (FS725). We use the Anritsu mainly for precision spectroscopy and for operations requiring control

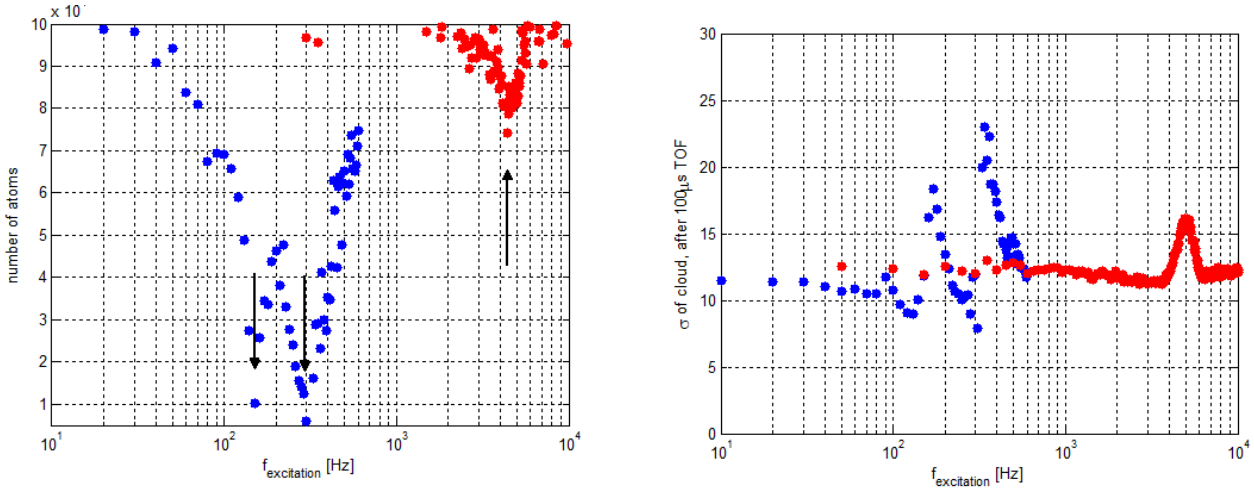

(a) (b)

Figure 19: Parametric resonance measurement. The excitation amplitude as well as the duration was not the same for low and high frequencies, plotted as blue and red circles. (a) This is a measurement of the number of atoms remaining in the trap after a modulation of the trap depth was applied. The vertical arrows point at the signal from a parametric resonance at 150Hz, 300Hz and 4400Hz. The highest frequency resonance is at twice the radial oscillation frequency, the signal at 300Hz is at twice the axial frequency and the signal at 150Hz is at the axial frequency and results from a subharmonic of the parametric excitation (the amplitude of the excitation was set to be quite large at the lower frequency parts of the experiment. (b) same experiment, but his time looking at the cloud size following excitation. Here the resonance is manifested as increase of the temperature of the cloud - resulting in larger cloud size. An interesting feature is the slight shift of the resonances to higher frequency compared with the loss measurement, so they are found at 160Hz, 320Hz and 5000Hz. This is due to to the inharmonicity of the trap - hotter atoms can be excited at lower frequencies and this actually causes cooling of the cloud below the resonance, effectively moving the center of the feature to higher frequencies.

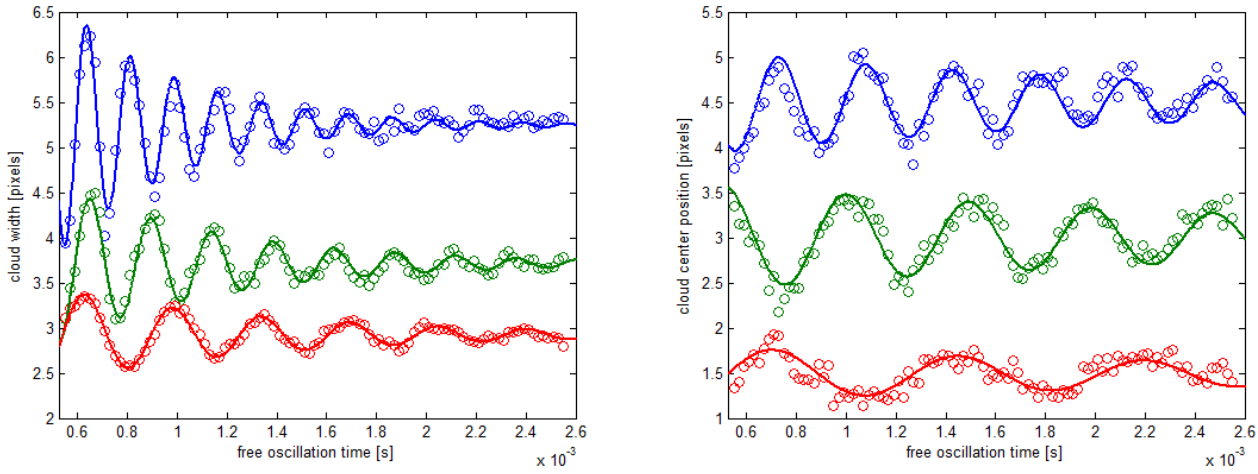

(a) (b)

Figure 20: Free oscillations of trapped atoms following a kick (trap was turned off for 75μs then on again). For both (a) and (b) a 12W trap appears as blue, 6W trap appears as green and a 3W trap as red. Solid lines are fits to an exponentially decaying sinus function. (a) Breathing mode, at twice the trap radial frequency, measured as oscillation in radial cloud width, following a ballistic expansion of 200μs. Values from fit (5712Hz,4087Hz,2819Hz) corresponding to radial frequencies of (2856Hz,2043.5Hz,1409.5Hz) (b) Common mode oscillations, at the radial frequency, showing as oscillations in the position of the cloud center. Values from fit (2865Hz,2038Hz,1340Hz). Both mode of oscillations were measured together. Here the trapping beam waist was different then in the parametric resonance measurement, in Fig.19.

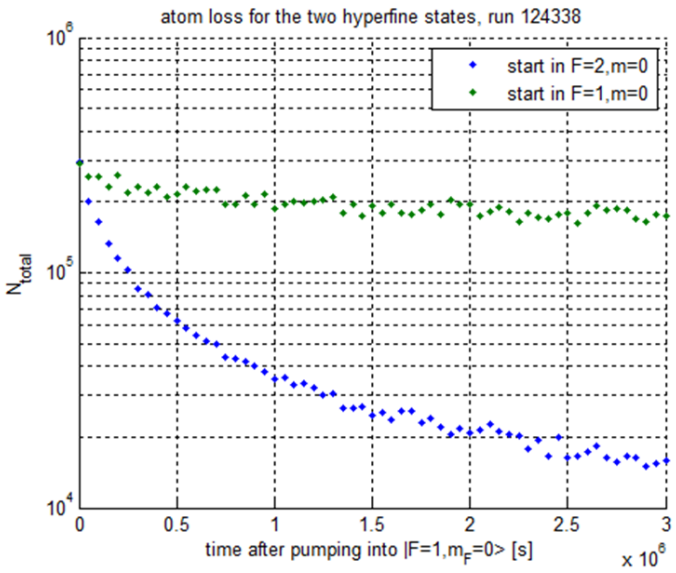

Figure 21: State dependent loss. For atoms in the F=2 trap loss is very short (<1s) and clearly density dependent since loss rate is reduced with number of atoms.

over the MW pulse phase, such as in Ramsey measurements, using its high quality analog phase modulation. For a greater flexibility we use it in addition with a secondary MW source, composed of a Keithley 3390 function generator operated at around 34MHz which is mixed up with a 6800MHz signal (to obtain 6834MHz at the HF resonance) output from a modified evaluation board (EVAL-ADF4158, setup up in the factory with a 5000MHz vco that needed to be replaced by a 6800MHz one), both locked to the same 10MHz reference discussed before. Because of the lower sideband at 6766MHz the effective power arriving to the atoms is reduced by a factor of 2 (Rabi frequency reduced by $\sqrt{2}$) but this does not present a problem, as our Rabi frequency is high enough. The lower sideband is detuned by approx 70MHz from the transition, and does not have a measurable effect on the atoms with $\frac{\delta}{\Omega} \approx 10^{-3} \ll 1$. With the Keithley 3390 it is easy to configure a FSK (frequency shift keying) scheme in which the output frequency can jump withing a fraction of a μs between two preset frequencies, at a TTL command from the FPGA running the experiment. This feature is quite useful and is used to our advantage in our MW assisted optical pumping scheme. Finally, a digital phase shifting scheme can be implemented by

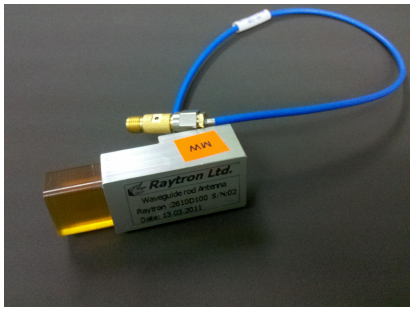

Figure 22: A compact microwave waveguide antenna used for injecting 6.8GHz radiation into the vacuum chamber.

using the FSK: by offsetting the frequency by Δf_{FSK} and returning to the original frequency within a time t we gain a phase of $\Delta\phi = t \times \Delta f_{FSK}$ (e.g. $\pi/2$ for 1MHz shift and 0.25μs delay). By this combination of few relatively cheap components we can get most of the functionality (that we need) of the multi $10K Anritsu.

3.6 MW assisted optical pumping

When atoms are loaded into the dipole trap it is beneficial to first pump them into the F=1 state. This prevents hyperfine changing collisions that result in loss due to the large energy release ($\Delta E = h{\cdot}6.8\text{GHz} \approx k_B{\cdot}300\text{mK}$). For that matter it is not important which Zeeman state they are pumped into, therefore this pumping is accomplished by using either the cooling laser or the depumping F=2→F'=1 laser, resulting in approximately $1/3 : 1/3 : 1/3$ distribution between the m=0,±1 levels of F=1 manifold. But when performing MW spectroscopy it is better to have the whole population in only one of the m states and increase the signal by a typical factor of 3. This will also increase the phase space density by the same factor, since the atoms will not be distributed among three distinguishable states.

We do the pumping in an unorthodox way, which leads to close to 100% pumping into the $|F = 1, m = 0\rangle$ state, as exemplified in Fig.23. We use a programmable function generator (Keithley 3390) mixed with an oscillator at 6,800MHz (A modified EVAL-ADF4158EB1Z from Analog Devices). The resulting MW signal is amplified and transmitted by a custom made waveguide antenna into the chamber. We use the FSK function

of the signal generator to enable switching between two MW frequencies resonant with the $|F=1,m=1\rangle \rightarrow |F=2,m=2\rangle$ and $|F=1,m=-1\rangle \rightarrow |F=2,m=-2\rangle$ transitions (at plus or minus three times the Zeeman splitting). By repeatedly (typically 20 cycles) applying a π pulse at each frequency and then applying a short 100μs pulse from the depumping laser (resonant with the F=2→F'=1 transition) we are able to almost completely empty the m=±1 states of the F=1 level, and are left with all the atoms in the m=0 state. This procedure is not optimal and some heating (on the order of 5μK) is observed, however, for our measurements, done at a low phase space density, this is of no consequence. Moreover, if this MW assisted pumping is done before an evaporation cooling stage, then the slight increase of temperature may be of no significance, and phase space density is increased due to the concentration of the population in a single internal level. This method for optical pumping is very flexible, enabling us to prepare the atoms in any of the m states (or alternatively to *empty* any of the m states) of the F=1 manifold, simply by a correct choice of the MW frequencies used in the pumping process, and without having to prepare an optical pumping beam with a specifically tailored polarization or alignment with respect to the quantization magnetic field.

3.7 Magnetic field control

When performing spectroscopic measurements on the Hz level, it is important to have precise control over the magnetic field at the location of the atoms, otherwise uncontrolled shifts may occur due to the second order Zeeman effect (affecting the otherwise magnetic insensitive clock transition). The best probe for the magnetic field are obviously the atoms themselves. In order to generate a specific magnetic bias in a certain direction, we first make sure that the stray magnetic field is nulled (this we achieve to better than 1mG or 100nT, see figure 25a). Then we can turn on a bias in a known direction using a set of three orthogonal, calibrated, magnetic bias coils, arranged in pairs centered around the vacuum chamber. We take advantage of the fact that the magnetic field at the location of the atoms, prior to any compensation, has a projection on all three major axes (defined by the bias coil pairs and the geometry of the vacuum system) of several hundreds of mili-Gauss, so that a bias in both the positive and negative direction of the X,Y and Z axes

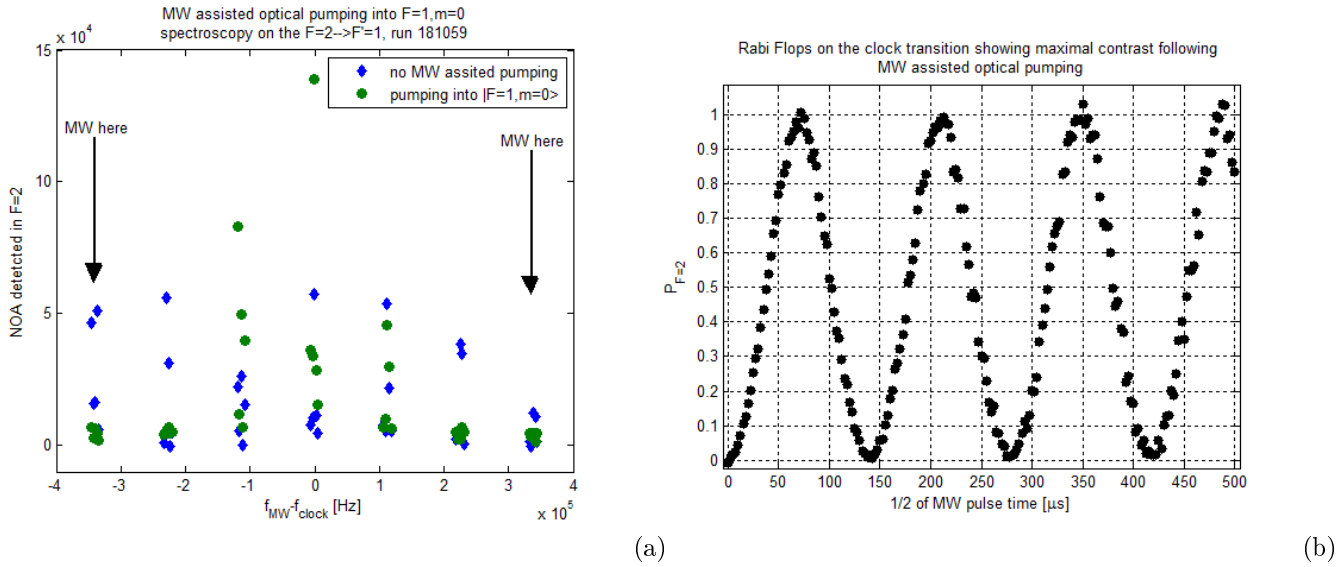

(a) (b)

Figure 23: MW assisted optical pumping. (a) Magnetic spectrum taken before and after pumping into the $|F = 1, m = 0\rangle$ Zeeman state. The black arrows indicate the frequency of the MW pulses that were used repeatedly for the pumping, and were interleaved with pulses from a depumper laser on the F=2→F'=1 transition. By applying the pulses on the transitions $m = \pm 1 \rightarrow m' = \pm 2$ the $m = 0$ population is not affected. (b) Rabi oscillations following pumping into $|F = 1, m = 0\rangle$ demonstrating a contrast close to 1: practically all the atoms are pumped into the clock state. A noise of few percent cause isolated measurements to be <0 or >1.

can be generated without needing to change the polarity of the current in the bias coils, simply by setting a current which is above or below what needed for compensation, thus greatly simplifying the electronics controlling the compensation currents. The current in the coils is actively feedback controlled by the FPGA, using a sensing resistor (5x0.1ohm, Dale) and a MOSFET (IRF540). We have the ability to generate any magnetic field vector (limited by $B < 1$G) and also to dynamically trace paths in the magnetic space, during an experimental sequence. Some of the effects of a dynamic quantization axis are presented in section 6.

The method for automatically finding the correct currents in each coil to null the residual magnetic field is simple and robust, and has enabled us to make prolonged measurements without student intervention. The absolute value of the magnetic field, with an applied field B_{ax} in the $\pm\mathbf{x}$ directions is given by $|\mathbf{B}_{\pm}|^2 = (B_{0x} \pm B_{ax})^2 + B_{0y}^2 + B_{0z}^2 = B_{0x}^2 + B_{0y}^2 + B_{0z}^2 + B_{ax}^2 \pm 2B_{0x}B_{ax}$, where B_{0i} are the components of the residual bias field. By measuring the field felt by the atoms under a *known* applied field in both positive and negative direction of three orthogonal axes, we can isolate the bias field components B_{0i} by using $|\mathbf{B}_+|^2 - |\mathbf{B}_-|^2 = 4B_{0x}B_{ax}$, and compensate for them. In order to calibrate the coils in the first place we first manually null the magnetic field by scanning the current in the compensation coils and looking at a MW spectroscopy scan showing at least the $m = 0 \rightarrow 0$ and $m = 0 \rightarrow \pm 1$ lines. Once the bias magnetic fields is zeroed (within our accuracy of approximately 1mG), it is possible to better calibrate the coils in term of current in mA per field in mG (actually we use some arbitrary units determined by the digital control in the FPGA and refer to the Zeeman splitting on the m=0→m=±1 transition in kHz, not mG, but this is of technical importance only). With a well calibrated set of coils it is then possible, given that the drift in magnetic field is not too large (a drift of more than 10kHz was never observed), to apply a *known* bias field in the $\pm\hat{x}$,$\pm\hat{y}$,$\pm\hat{z}$ directions. The position of the m=0→m=+1 peaks in the spectrum is measured and any shifts between the + and - peaks (figure 26) are due to a drift in the external field, which is then compensated by updating the values of the compensation currents, figure 25c. This procedure is repeated whenever there is a need to better null the magnetic field and was usually interleaved between measurements in long experimental runs.

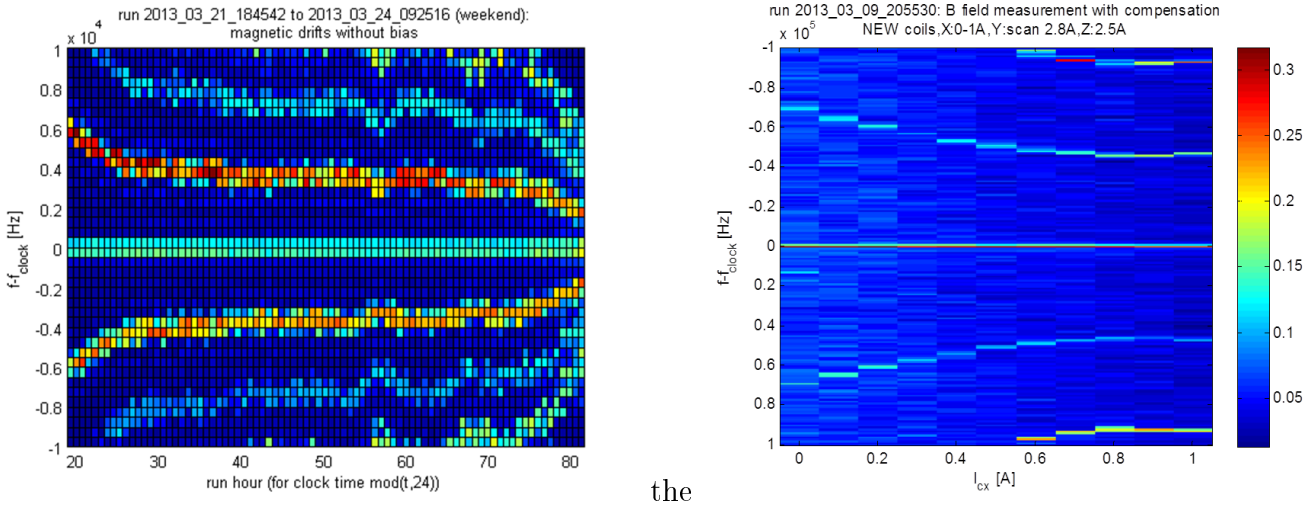

(a) (b)

Figure 24: **(a)** A long measurement of uncompensated magnetic field, showing drifts in the field magnitude. The bright stripes represents transitions between states in the different Zeeman manifold, and the further they are apart the larger is the magnetic field. **(b)** Here the current in one of the compensating coil pairs is scanned. The magnetic field generated by the compensating coil cancels one of the components of residual field at around 0.9A. The finite spectral distance between Zeeman transitions at this point is due to residual field in the orthogonal directions.

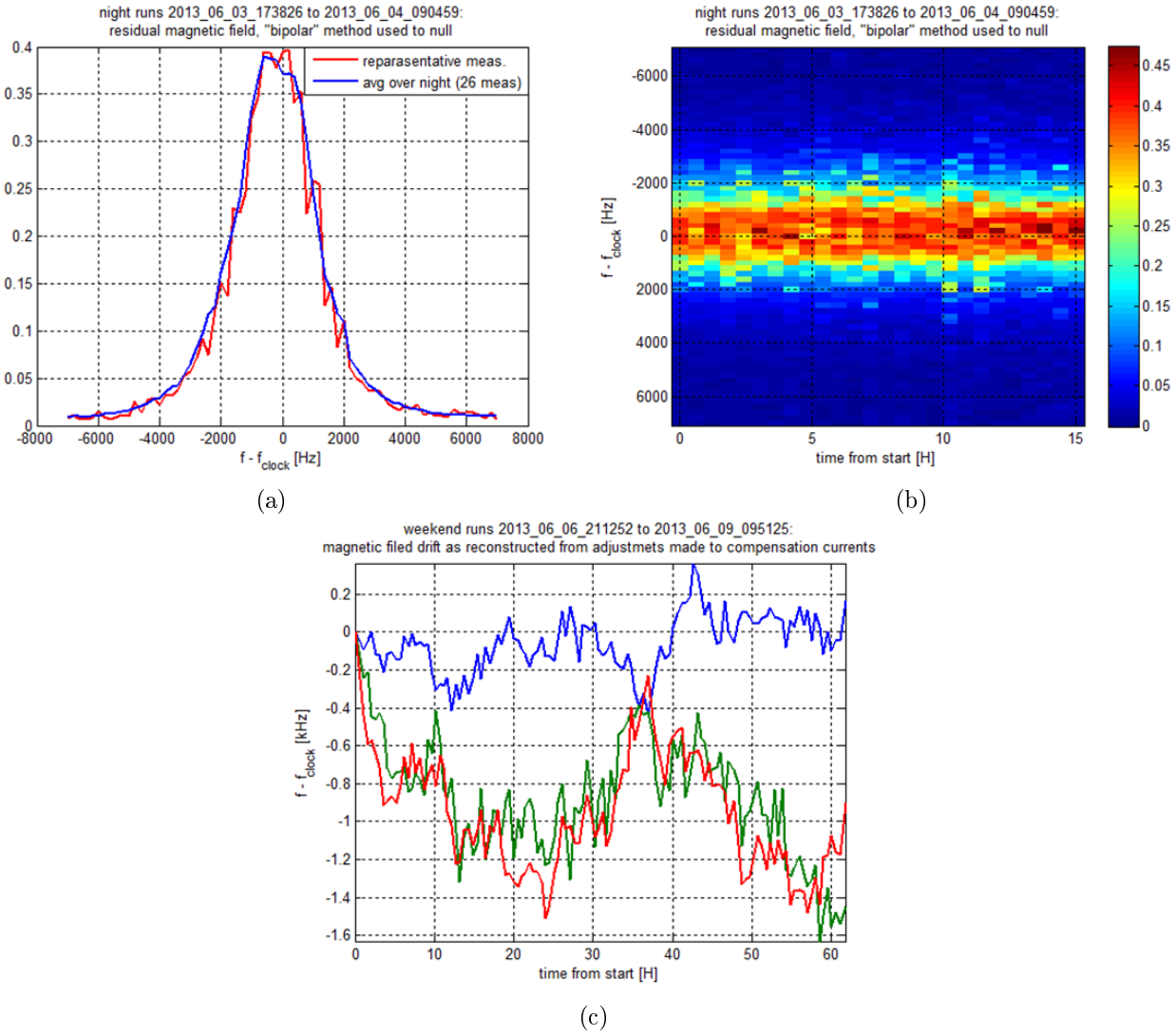

Figure 25: **(a)** Residual magnetic field measurement after automatic nulling. Magnetic Zeeman lines are closer than their widths, limited by AC magnetic noise. **(b)** same measurement as in (a), showing individuals scans **(c)** Magnetic field drifts, as obtained from the auto-calibrated compensation currents. (blue,green,red) refer to the stray magnetic field in the (x,y,z) axes. There are slow drifts with very long time scales and small amplitude

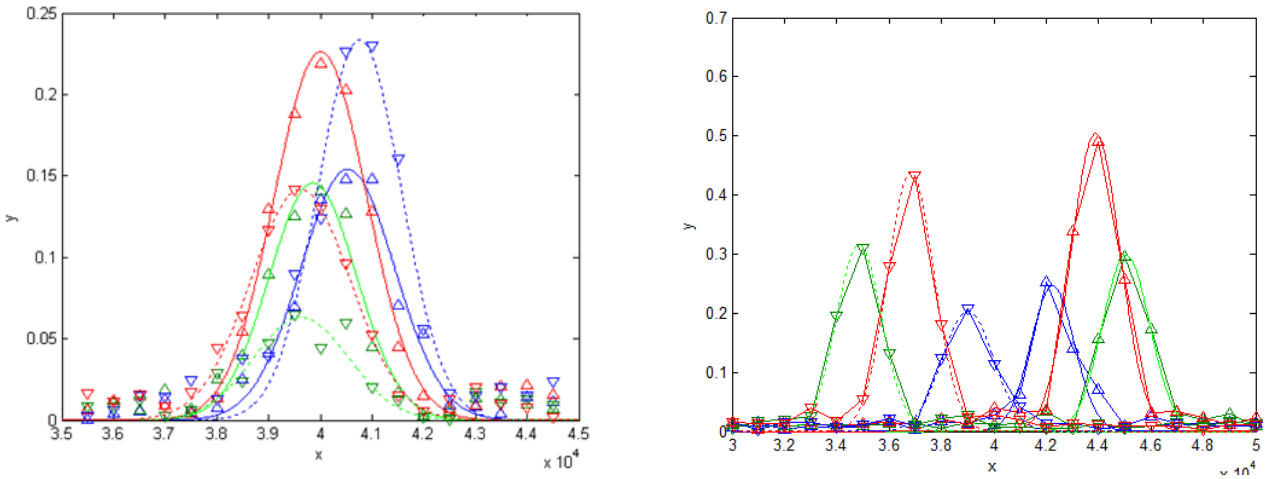

(a) (b)

Figure 26: A snapshot from the magnetic auto nulling procedure. (Blue,green,red) are with bias applied in the (x,y,z) directions. ∇ represents biases in the negative directions and $\triangle$ represents positive biases. On the left the residual field is nearly compensated while on the right there is a residual field of approx. (1.25kHz,5kHz,4kHz) or (1.8mG,7.1mG,5.7mG) in the (x,y,z) directions. The Zeeman shift of the $m = 0 \rightarrow m = \pm 1$ used for this calibration is 700kHz/G.

3.8 Absorption imaging and normalized detection of the hyperfine population

In many similar systems dealing with spectroscopy of trapped atoms, the detection of the population in each of the hyperfine states is done by recording the fluorescence from the atoms, proportional to the number of atoms in the F=2 state, when they are exposed to light resonant with a closed transition, F=2→F'=3 for ^{87}Rb [26, 38]. To make a normalized detection, beneficial for its lower sensitivity for fluctuations in atoms number, one must also measure, in the same experimental run, either the population in the F=1 level alone or the total number of atoms. In our system is was difficult to get decent fluorescence readings because of the large distance between the atoms the light collecting objective (a distance dictated by the geometry of the vacuum system). Also, because of technical reasons there is quite a lot of scattered light causing a decrease in the signal-to-noise ratio in florescence measurements. Instead, we rely on a absorption imaging of the F=2 and F=1 populations, a method that is better suited to the small NA (≈ 0.084) of our imaging system. This is done by taking two absorption (shadow) images of the atomic cloud, the first without a repumping (F=1→F'=2) beam, and the second with the repump included. Thus we image the population in the F=2 hyperfine state alone in the first image, and the whole cloud (both populations) in the second. As is typical in such images, in which a laser beam is aligned directly on the camera, there is a highly visible fringe pattern in the two images. While we were able to reduce the visibility of these fringes and also to make them more stable in time, by using an uncollimated fiber as the source for the absorption beam, these fringes are still a problem and make the analysis of the absorption images difficult. Usually in absorption imaging of cold atoms one gets rid of these fringes by taking another "reference" image that does not include the atoms very shortly (tens of micro-seconds) after the image containing the shadow of the atoms is taken. It is essential to take the reference image at a delay shorter than the fringe decorrelation time, governed by the acoustic vibrations in the systems. Unfortunately, our camera is a "double shutter" camera, meaning that only two consecutive images can be taken at short a interval, and both are used for the normalized detection scheme. Instead we take a third image without atoms 100ms after the data-full images and rely on image processing algorithms to remove

the fringes from all images, similarly to [32, 27]. With the imaged fringe contrast largely reduced, as seen in Fig. 28, it is possible to measure the total number of atoms and F=2 population, by simply fitting the images to a two dimensional Gaussian function. However, even when the quality of the absorption image is enhanced by the fringe removal algorithm, it is still a problem to detect the population in measurements in which the population of the F=2 state, or the total number of atoms, is very low, since the fitting algorithm may fail. To circumvent this problem we employ the following procedure: we take advantage of the fact that in a typical measurement run it is only the population that changes between data points, while the temperature and number of atoms remain the same. The shape of a cloud of thermal atoms has the same shape regardless of the number of atoms, and depends only on its temperature, for a fixed TOF. It is possible to create a clear image of representative F=2 and F=2 + F=1 clouds by just averaging over the images of "F=2" and "total" clouds. We then fit a 2D Gaussian to each of these representative images, extracting the centers and widths of the clouds. These are used as fixed parameters when extracting the number of atoms by fitting each individual noisy image. This heuristic method greatly improves the population estimation from a series of measurements and we can typically achieve rms detection error of $\approx 2\%$ in the population, as estimated from the scatter around a fit for a single Ramsey fringe, seen in Fig. 41.

3.8.1 absorption imaging

Consider a beam of light close to resonance with a closed transition of the atoms (F=2→F'=3 in our case). Each of the atoms scatters photons from the beam at a rate $R_{ph} = \frac{\Gamma}{2}\frac{I/I_{sat}}{1+I/I_{sat}+(\frac{\Delta}{\Gamma/2})^2}$, where I_{sat} is the saturation intensity, $\tau = \frac{1}{\Gamma}$ is the excited state life time (here the excited state is the $5P_{\frac{3}{2}}$) and Δ is the detuning from the transition in $2\pi \times$ Hz. For a beam of low intensity resonant with the transition, the scattering rate reduces to $R_{ph} = \frac{\Gamma}{2}\frac{I}{I_{sat}}$. As the light passes through an atomic sample of density n it encounters $N = c \times n$ atoms per unit time per unit area. Each of the atoms scatters on average R_{ph} photons per unit time and so the intensity is reduced as $\frac{dI}{dt} = -NR_{ph}h\nu = -nc\frac{h\nu\Gamma}{2I_{sat}}I$. Using $\frac{dI}{dz} = \frac{1}{c}\frac{dI}{dt}$ we get to $\frac{dI}{dz} = -n\frac{h\nu\Gamma}{2I_{sat}}I$. Solving this simple equation we retrieve the Beir-Lambert law $I(z) = I_0 e^{-n\sigma z}$, with I_0 the intensity of the incoming beam and the photon

scattering cross section $\sigma = \frac{h\nu\Gamma}{2I_{sat}}$. We can use this to calculate the intensity of the output beam, for any density profile $n(x,y,z)$ as $I(x,y) = I_0(x,y)e^{-\int n(x,y,z)\sigma dz} = I_0(x,y)e^{-\sigma\tilde{n}(x,y)}$ where $\tilde{n}(x,y) = \int dz n(x,y,z)$ is defined as the column density. In absorption imaging we record this intensity profile $I(x,y)$ on a CCD or similar device and normalize it by the intensity profile of the beam with no atoms present $I_0(x,y)$. Taking the natural logarithm of the result we are left with an image of the optical density (OD), that is proportional to column density. By either summing over the whole pixel array, or better yet, fitting to a adequate model of the column density (for thermal atoms this is usually just a two dimensional Gaussian), we obtain the number of atoms in the image. A reference image I_0, containing no atoms, is obtained by turning on a depumper beam resonant with the F=2→F'=1 transition for a short time (typically 20μs), transferring all the atoms in the cloud to the dark (w.r.t. the detection beam) F=1 state. The two images, with and without the atoms, are thus taken for the same atomic sample within a short interval, typically <200μs. A typical image is presented in Fig. 27.

3.8.2 absorption imaging for normalized detection

Sometimes, however, it is not possible to take both data and reference images within a time short enough such that the fringe patterns in both images are correlated. We are faced with this problem when trying to make a normalized detection of the hyperfine populations since we must use both available exposures of our double shutter camera to photograph the F=2 atoms and total atom populations, as required for our implementation of normalized detection. We circumvent this problem by taking many reference images and synthesizing from them a suitable reference for each of the data images. The method relies on the assumption, correct to a good approximation, that while the fringe pattern itself changes rapidly, its statistical properties change much more slowly. It could be said that while any two recorded fringe patterns are different, they still share the same characteristic features and the change is only in the relative weight of those prominent features. This is true because the objects causing the interference pattern, such as dust specs on the optics, reflecting surfaces in the beam paths etc do not move between realizations, only due to acoustic vibrations. This method is based on the eigenface method for face recognition

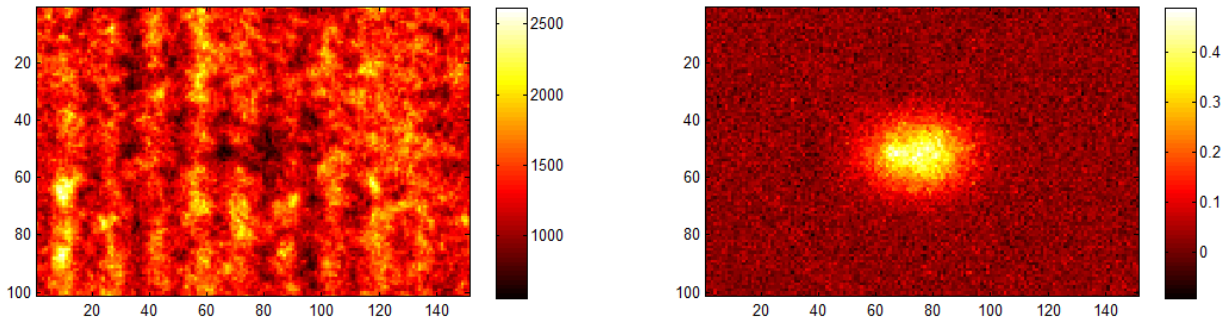

(a) (b)

Figure 27: Absorption imaging. (a) A shadow image of about 60,000 atoms at $\approx 70\mu$K, 600μs after being released from the trap. The atoms are barely visible as a slight decrease in the intensity of the absorption beam (resonant with the cycling transition F=2→F'=3) as recorded on a CCD. (b) A optical density image, obtained by dividing each pixel of the shadow image by the pixels of a reference image and taking the natural logarithm. The reference image is taken just 100μs following the shadow image, using a fast double shutter camera. We are able to remove the atoms completely from this reference image by shining a depumper beam on the F=2→F'=1 transition, causing the atoms to be pumped into the dark F=1 ground state.

where the same principle applies[45]: while all faces are different, almost all of them contain very similar features such as two eyes placed symmetrically around a single nose.. (if you are lucky and nothing very unpleasant has taken place). More generally this procedure is usually referred to as "principle component analysis" (PCA), and is closely related to a more general singular value decomposition (SVD). In the following paragraph the main points of this method and specifically its application for the removal of fringes from absorption images is discussed, similar to [32, 27].

An image I is a $m \times n$ matrix containing real values. From an image matrix I, a column vector ("a face") $x \in \mathbb{R}^d$ with d entries is formed by vertically concatenating the columns from I (it is easier to work with vectors). The "mean face" is the expectation value $\mu = E\{x\}$. Centered face vectors are defined by substructing the mean face $y = x - \mu$ ($E\{y\} = 0$). The variance $Var\{y\} \equiv E\{y^T y\} = \sum_{i=0}^{d-1} E\{y_i^2\}$, where y_i is the ith element of the random vector v, is a measure of the deviation from the mean face. The covariance matrix is defined as $C = E\{yy^T\}$. . The eigenvectors v_k ($k = 0, 1, ..d-1$) of C satisfy the eigenvalue equation: $Cv_k = \lambda_k v_k$. The eigenvectors form a basis so any centered face y can be written as $y = \sum \alpha_k v_k$. Using the eigenvectors we can write the variance as $Var\{y\} = E\{\sum_{kl} \alpha_k \alpha_l w_k^T w_l\} = \sum_{kl} \delta_{kl} E\{\alpha_k \alpha_l\} = \sum_k E\{\alpha_k^2\}$ where we have used the orthonormality of the eigenvectors $\delta_{lk} = v_l v_k^T$. Multiplying the eigenvalue equation from the left with a transposed eigenvector v_k^T we arrive to $\lambda_k = v_k^T C v_k = v_k^T E\{yy^T\} v_k = E\{(v_k^T y)(y^T v_k)\} = E\{\alpha_k^2\}$ and finally $Var\{y\} = \sum_k \lambda_k$. What is the meaning of this? we have shown that the variation, $Var\{y\}$, is a sum of the contributions from variations in very certain directions in this m-dimensional space, which are the eigenvectors of the covariance matrix. The eigenvector with the largest eigenvalue contributes most to the variations. Since the data is not completely random, meaning, it has a structure (faces, fringes etc.) its real dimensionality is much less than the dimensionality d of the vector space, and therefore only a few of the eigenvectors, say k_0 of them, actually contribute. In other words $\frac{\lambda_k}{\lambda_0} \ll 1$ for some $k > k_0$. This is fortunate since we do not need all the d eigenvectors and eigenvalues (d is a large number). This property is beneficial when this method is used for face recognition, since any face can be attributed a small number of coordinates α_k which can then be used to identify it.

In practice, we usually do not know the covariance matrix C or the mean face μ

beforehand. These entities can be approximated by their empirical counterparts using N available images $\mathbf{x}_i$: $\hat{\mu} = \frac{1}{N}\sum_i \mathbf{x}_i$, $\hat{C} = \sum_i \mathbf{y}_i\mathbf{y}_i^T = AA^T$, where $A = [\mathbf{y}_0...\mathbf{y}_{N-1}]$ is a matrix holding N centered images. However, when attempting to directly implement the eigenface method we are faced with a problem: the dimension of the covariance matrix $\hat{C}$ is d^2, already huge for a modest sized image of 100 pixels on a side (then $d^2 = 10^8$). Finding the eigenvectors of such a huge matrix is computationally very demanding and in practice impossible. Instead we use the following trick: using that $\hat{C} = AA^T$, then $\hat{C}u_k = AA^Tu_k = \lambda_k u_k$. With $N \ll d$ the matrix $\tilde{C} = A^TA$ is of only $N \times N$. Its corresponding eigenvalue equation is $\tilde{C}\tilde{u}_k = A^TA\tilde{u}_k = \gamma_k\tilde{u}_k$. multiplying from the left with A we get $A(A^TA)\tilde{u}_k = A\gamma_k\tilde{u}_k = \Lambda_k A\tilde{u}_k$ but this also equals $(AA^T)A\tilde{u}_k = \Lambda_k(A\tilde{u}_k)$ or simply $\hat{C}(A\tilde{u}_k) = \gamma_k(A\tilde{u}_k)$. Hence $A\tilde{u}_k$ is an eigenvector of $\hat{C}$ with the eigenvalue γ_k, and therefore $\gamma_k = \lambda_k$ and $u_k = A\tilde{u}_k$.

The algorithm is as follows: we take a set of N reference images $\mathbf{x}_i$. We find the mean $\hat{\mu}$ and subtract it from $\mathbf{x}_i$ to obtained the centered images $\mathbf{y}_i$. Using the machinery described in the former paragraph, we find the set of most important eigenfringes (with highest eigenvalues) from a set of reference images we are ready to reconstruct the a reference image for each data image. This is done by projecting the data image on the set of orthogonal eigenfringe images, using only the part of the image that does not contain the atoms. The new reference image is $\mathbf{x}_{ref} = \sum \alpha_k u_k + \hat{\mu}$. A Matlab implementation of the fringe removal algorithm is given in appendix A.

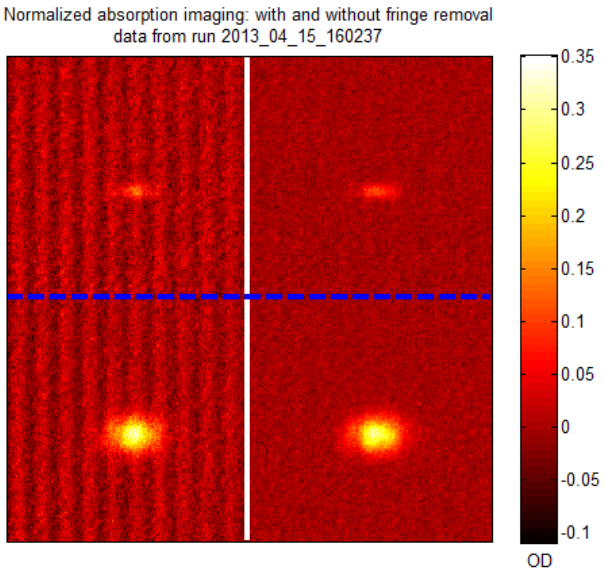

Figure 28: A typical example of the normalized detection using absorption imaging technique. On the left is an OD image obtained using a reference image taken some 200ms (limited by the rep rate of the camera), with clearly visible fringes. On the right, the contrast of the fringes is much reduced by using a synthesized reference image. The improved OD image enables accurate detection of the F=1,F=2 populations, the use of synthesized references makes it possible to use a double shutter camera without a reference image taken together with the measurement. In this example the extracted total number of trapped atoms is 38×10^3 of them 4,300 populate the F=2 state, for a $P_{F=2} = 11\%$.

4 A measurement of the ratio between the tensor and scalar hyperfine differential light shifts

4.1 Introduction

An atom, placed in an electric field, experiences a shift of its energy levels due to the Stark effect. This shift is the origin of the trapping potential induced by our CO_2 laser and can be written as

$$\delta E = -\frac{1}{2}\alpha_0 \mathbf{E}^2 \tag{16}$$

where α_0 is the static electric polarizability of the atoms and $\mathbf{E}$ is the electric field of the trap laser. The factor of $\frac{1}{2}$ is due to the fact that the electric dipole is induced, and not permanent. While Eq.(16) is an approximation that treats the electric field of the CO_2 laser radiation as a DC field, it is a very good one. A still better approximation could be used [47, 49], that takes into account $\omega_0 = 2\pi\frac{c}{795\text{nm}}$ the frequency of the closest transition (the D1 line at 795nm) and the trap laser frequency $\omega = 2\pi\frac{c}{10{,}600\text{nm}}$: $\alpha_0(\omega) = \frac{\omega_0^2}{\omega_0^2-\omega^2}\alpha_0 = 1.0057\alpha_0$ but the correction is unimportant for most purposes. Since both of the ground states of Rb share the same electronic configuration (both belong to the $5s$: the $l = 0$ orbital) it may be expected that they have the same polarizability. This is indeed true when hyperfine interactions are neglected. However, the fact that the electronic wavefunction is slightly distorted due to the hyperfine interaction gives rise to a F dependent polarizability. The shift may be written as

$$\delta E_{F,m_F} = -\frac{1}{2}\alpha_F^S \mathbf{E}^2 - \frac{1}{4}\frac{3m_F^2 - F(F+1)}{F(2F-1)}\alpha_F^T(3E_z^2 - \mathbf{E}^2) \tag{17}$$

where α_F^S and α_F^T are the scalar and tensor parts of the polarizability and E_z is the component of the electric field along the (magnetic) quantization axis [4, 11]. The differential

shift for the clock transition ($|F=1,m=0\rangle \leftrightarrow |F=2,m=0\rangle$) is

$$\begin{aligned}\delta E_{clock} &= \delta E_{2,0} - \delta E_{1,0} \\ &= -\frac{1}{2}(\alpha^S_{F=2} - \alpha^S_{F=1})\mathbf{E^2} - \frac{1}{4}(-\alpha^T_{F=2} + 2\alpha^T_{F=1})(3E_z^2 - \mathbf{E}^2) = \\ &= -\frac{1}{2}\left(\alpha^S_{clock} + \alpha^T_{clock}(3\cos^2\theta - 1)\right)\mathbf{E}^2 \end{aligned} \quad (18)$$

where $\alpha^S_{clock} = \alpha^S_{F=2} - \alpha^S_{F=1}$ and $\alpha^T_{clock} = -\frac{1}{2}\alpha^T_{F=2} + \alpha^T_{F=1}$ are respectively the differential scalar and tensor polarizabilities of the clock transition, and θ is the angle between the magnetic quantization axis and the applied electric field. For the Rb atom, the fact that the shift is different for its two hyperfine states implies that the clock transition frequency changes when an electric field is applied. Specifically for atomic clocks the stochastic field of black body radiation (BBR), that is always present assuming that the clock is not kept at cryogenic temperature, is of concern. Actually, uncertainty in the BBR shift is currently one of the limiting factors in the accuracy of Rb based atomic clocks [17]. Note that for an isotropic field such that of BBR, the tensor shift averages to zero so that the scalar shift is the only relevant shift. We introduce the scalar shift coefficient $h(\delta\nu_{clock})_S = k_s E^2$, in accordance with other works **[37, 11, 50, 15, 33]**. While there have been theoretical calculations to a 10^{-3} level ($k_s = -1.240(4) \times 10^{-10}\mathrm{Hz/(V/m)^2}$) [11, 37] and a measurement to few percent accuracy ($k_s = -1.23(3) \times 10^{-10}\mathrm{Hz/(V/m)^2}$) [30] of the scalar part of the hyperfine differential polarizability, no direct measurement of the tensor part of the polarizability for the ^{87}Rb clock transition was ever published, although a measurement of the tensor polarizability of the F=2 state was done using a "flop-in" RF transition between the magnetic sensitive states $|F=2,m=1\rangle$, $|F=2,m=2\rangle$ by atomic beam techniques **[15]**. Since generally the two effects occur together when applying a static electric field pointing in a certain direction, the value of the tensor polarizability is required to correctly compensate for it in measurements aimed in extracting the scalar polarizability [30, 44]. Also, a recent calculation [11] of the tensor part is accurate only to 30%. Clearly a measurement of this quantity with improved accuracy is called for. For Rb atoms trapped in a quasi electrostatic trap like in our system, the atoms can experience quite a significant scalar shift, due to the trapping laser itself, typically of hundreds of

Hertz, easily measured by MW spectroscopy, and with the tensor shift being approx 1% of the scalar it is measurable too. For convenience, we define the full tensor shift as the differential shift between two orthogonal configurations of the electric field, $\mathbf{E} \parallel \mathbf{z}$, $\mathbf{E} \perp \mathbf{z}$, and so the full tensor shift coefficient is defined by $h(\delta\nu_{clock})_T = k_T \mathbf{E}^2 = -\frac{3}{2}\alpha^T_{clock}\mathbf{E}^2$.

4.2 Measurement of the differential tensor shift

We have used Ramsey spectroscopy of atoms trapped in our quasi electrostatic CO_2 trap to measure the ratio between the tensor and scalar shifts. Here the CO_2 laser doubles both as a source for the trapping potential and a means to apply strong electric fields in vacuum. The experimental procedure is as follows: ^{87}Rb atoms are collected and cooled by a MOT are then loaded into a trap formed at the focus of a CO_2 beam. After loading all cooling lasers are extinguished by acousto optical switches and mechanical shutters and a self evaporation phase follows, allowing the atoms to cool further, down to 30-10μK, depending on the trap depth. The trap laser power is kept constant during this period in order to minimize transients in the applied field. After one second of self cooling we apply a magnetic field along the $\hat{x}$ axis, parallel to the propagation direction $\hat{k}$ of the trap laser. The atoms are then pumped into the $|F = 1, m = 0\rangle$ state using the MW assisted method described in previous section. After the pumping is complete we align the magnetic field with the direction chosen for the measurement (if necessary the magnetic field vector is rotated adiabatically during several ms by adjustments to the bias coils currents) . The direction of the applied magnetic field is cycled from one data point to the next between the three principle axes, which are determined by the orientation of the magnetic compensation coils, $\hat{x}$, $\hat{z}$ or $\hat{y}$ directions where $\hat{z}$ is along the polarization of the trap laser, and $\hat{y}$ is perpendicular to both. We wait for two more seconds before performing a Ramsey pulse sequence, where the two $\pi/2$ pulses are separated by a Ramsey time t, which is scanned to obtain a Ramsey time signal $R(t)$. In order minimize the effect of drifts in the system parameters t wasn't scanned linearly but rather we generated a random permutation of the pulse separation times in the range for 1ms to 80ms with 0.5ms resolution. The decaying Ramsey signal is shown in Fig.29, where the fit is done

with respect to a theoretical curve for non interacting atoms in a harmonic trap [26]]

$$R(t) = B + A\left[1 + \left(\frac{t}{K}\right)^2\right]^{-\frac{3}{2}} \cos\left[\delta t - 3\arctan\left(\frac{t}{K}\right) + \varphi\right] + C \cdot t \tag{19}$$

We use a similar notation as [26]: the bias B and the amplitude A are ideally $\frac{1}{2}$ for a perfect initialization at $|F = 1, m = 0\rangle$. C is a phenomenological linear baseline observed in the data and can be attributed to a slow T1 process. The decay constant is $K = \frac{2\hbar}{\eta k_B T}$ and $\eta = \frac{\alpha_S}{\alpha_0} = \frac{\hbar\delta_0}{U_0}$ is the ratio between the differential and ground state polarizability, or between the trap depth $U_0 = \frac{1}{2}\alpha_0 \mathbf{E}^2$ and the hyperfine shift $\hbar\delta_0 = \frac{1}{2}(\alpha_S + \alpha_T(\theta))\mathbf{E}^2 \approx \frac{1}{2}\alpha_S \mathbf{E}^2$. The detuning, relative to the synthesizer frequency (that sets the reference frame) is $\delta = -\left[|\delta_{synth}| - (|\delta_0| + |\delta_n| - |\delta_B|)\right]$ is composed of the MW synthesizer detuning from the free Rubidium clock transition frequency, $\delta_B = B \times 575.15\mathrm{Hz/G}^2$ is the second order Zeeman shift on the clock transition with a magnetic field B and δ_n is a density dependent shift. The synthesizer was always tuned to a frequency below the maximal shifted resonance frequency (at the trap bottom!) so that the inhomogeneous spectral distribution was completely to one side of the carrier placing the coldest atoms which experience the largest stark shift at the smallest detuning with respect to the local oscillator. By ensuring that the carrier is bellow the most severely detuned atom we have a well defined minimal frequency component in the Ramsey signal (related to the atoms at the trap bottom), and a well defined sense of rotation in the Bloch sphere. The number of trapped atoms and their density, always below $10^{12}\,\mathrm{cm}^{-3}$, was kept intentionally low by shortening the loading time, to keep density dependent mean field shifts, as well as effects of discrete collisions at a low level, to comply with the approximation for non interacting atoms. From this fit the absolute light shift, as well as the decay constant, the later depends only on the temperature of the ensemble, were extracted. The tensor and scalar parts of the differential hyperfine polarizability are obtained by directly measuring the shift with an applied magnetic bias directed along the polarization of the trapping laser ("$\mathbf{z}$"), along the $\mathbf{k}$ of the trapping laser ("$\mathbf{x}$"), a direction guaranteed to be perpendicular to the polarization (within the paraxial approximation), and a direction perpendicular to the other two ("$\mathbf{y}$"). The measurement was repeated between 12 and 16 times for each of the

applied magnetic field directions at different trapping laser powers, from 0.75W to 4.5W, covering half a decade of scalar shifts. Each Ramsey signal is composed of 160 experimental points, we obtained a total of 3×91 such Ramsey signals for a total of 43,680 instances of the experiment, during approximately 100 hours of almost continuous lab run time. A magnetic field recalibration sequence was interlaced between completed measurement cycles, about once an hour. At each magnetic field recalibration the field in all three principal directions is measured and the currents in the bias coils are adjusted to keep the field at 50kHz. We later use the those measurement of the magnetic field to estimate using a cubic spline interpolator the value of the field at the time of the Ramsey measurement (taken to be the mid time of the Ramsey measurement phase of the experiment) and this value is used to adjust the measured detuning to account for the drift in second order Zeeman shifts. We also measure the number of atoms at each measurement, a figure later used to account for mean field density shifts, as described in a following paragraph below.

4.3 Data analysis

After analyzing each of the Ramsey experiments we obtain a set of frequencies from the fit to the theoretical decaying signal. In Fig.30 we plot these frequencies, referenced to the local oscillator against the time at which the experiment was conducted. Already in this simple presentation the effect of the tensor polarizability is clearly showing: the shift measured with the magnetic field along at the two directions **x** and **y** orthogonal to the electric field of the trap, is the same, and both are smaller than the shift measured with $\mathbf{B} \parallel \mathbf{E}$. We observe a common behavior in which the measured frequency settles to a steady value in a time scale of an hour, probably due to a thermal drift effecting the trap depth. These drifts, on the order of 1% appear in almost all of the experiments at different trap powers, and have little effect on the measured tensor shift, however, by only using the measured shifts themselves and the difference between them to deduce the value of the tensor shift, we can take this effect fully into account.

The goal of this experiment is to measure the shift related to the tensor part of the differential polarizability of the clock transition. However, we have no reliable, direct, method to measure the field to which the atoms are subjected and is inducing the shift.

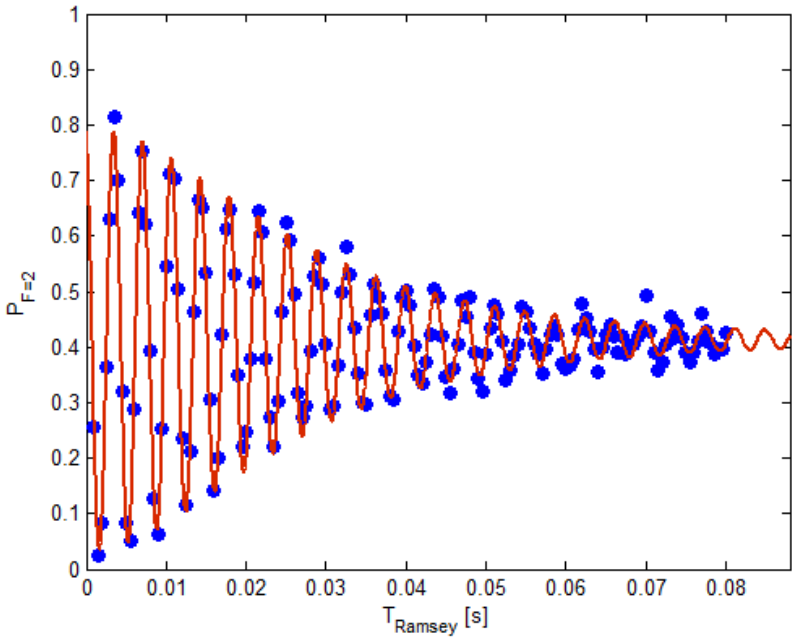

Figure 29: A typical Ramsey signal, in this example for a trap beam power of 1.5W. The blue circles are the populations as measured by absorption imaging. The red line is a non linear least squares fit to Eq. (19). Here the parameters extracted from the fit are K= 0.03287 (0.03149, 0.03424)s, $\delta = 2\pi\times263.8$ (263.4, 264.2)Hz with 95% confidence interval in parenthesis.

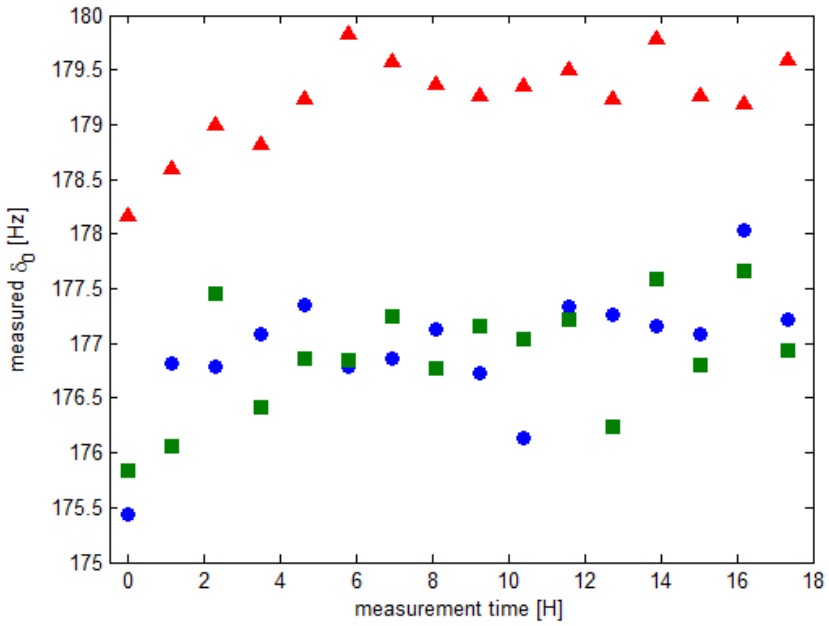

Figure 30: Results from individual consecutive runs. blue: $\mathbf{B}||\mathbf{x}$, green: $\mathbf{B}||\mathbf{y}$, red: $\mathbf{B}||\mathbf{z}$. note that for the two directions that satisfy $\mathbf{B} \perp \mathbf{E}$ the shifts are the same. The small drift is due to slow trap power drift during the first couple of hours of experiment. This drift is $<1\%$ and has no effect on the measurement since we for each run the difference $\delta_x = \delta_{B_z} - \delta_{B_x}$ and $\delta_y = \delta_{B_z} - \delta_{B_y}$is compared to δ_{B_z}.

Any method relying only on quantities of the trapping beam is questionable since calibration error in the beam power, waist, mode or the existence of aberrations will contribute to an error in the derived electric field and in the value attributed to the polarizability. Instead we use a self referenced method that only takes into account the spectroscopically measured shifts. The full tensor shift measured between the parallel ($\mathbf{B}$ along $\mathbf{z}$) and perpendicular directions ($\mathbf{B}$ along $\mathbf{x}$ and $\mathbf{y}$) of the magnetic field is referenced to the shift with the fields parallel. This shift by itself is an accurate, spectroscopic, measurement of the electric field, using the atoms themselves as a probe. Thus the quantity that is directly measured here is ξ, given by

$$\xi = \frac{\delta E_{\mathbf{B}\parallel\mathbf{E}} - \delta E_{\mathbf{B}\perp\mathbf{E}}}{\delta E_{\mathbf{B}\parallel\mathbf{E}}} = \frac{3\alpha^T_{clock}}{\alpha^S_{clock} + 2\alpha^T_{clock}} = 3\frac{\alpha^T_{clock}}{\alpha^S_{clock}}\frac{1}{1+2\frac{\alpha^T_{clock}}{\alpha^S_{clock}}} \approx 3\frac{\alpha^T_{clock}}{\alpha^S_{clock}} \tag{20}$$

The correction to the approximated relation is negligible compared with the experimental uncertainty, as seen later, but can be treated as a systematic effect and included in the result by multiplying it by $\xi \to \xi(1+\frac{2}{3}\xi)$.

In Fig.31 the difference in shifts between perpendicular and parallel orientations of the magnetic and electric fields are plotted against the shift with the fields parallel. This relation is necessarily linear, since everything is proportional to (the unmeasured) $\mathbf{E}^2$ and we continue by fitting a linear relation $y = mx + b$, to the data set $\{x_i, y_i\}$, with x_i the total shift (with electric and magnetic fields parallel) measured at the i'th experiment, and y_i the differential shift at the same experiment . The dimensionless slope m (both x_i and y_i have the units of frequency, Hertz) corresponds to the tensor to scalar ratio defined above in ξ and the bias b is expected to be consistent with zero. From this point we must proceed with caution. The uncertainties, and indeed the scatter in the $\{x_i\}$ is comparable to the scatter in the $\{y_i\}$, see Fig.30. It is therefor unjustified to use a simple linear least squares fit, which assumes no errors in $\{x_i\}$. While there exist iterative methods that take into account the scatter in the $\{x_i\}$, these cannot be justified by any model, and might be dependent on the initial conditions of the fitting algorithm **[20, 34]**. Instead we take a step back and examine the problem of fitting a line to a scattered data more carefully. We remember that the method of least squares originates from the demand to maximize the

likelihood of obtaining the data, given a Gaussian noise model and line parameters m, b: $\mathcal{L} = p(\{y_i\}|m, b, \{x_i\}) = \Pi_i \exp(-\frac{(y_i-(mx_i+b))^2}{2\sigma_{y_i}^2})$. We wish to generalize this expression to treat $\{x_i\}$ and $\{y_i\}$ on equal footing. Allowing noise in both x and y, a "true" point (x, y) is shifted by a Gaussian noise with zero mean and covariance matrix $\Sigma = \begin{pmatrix} \sigma_x^2 & \rho\sigma_x\sigma_y \\ \rho\sigma_x\sigma_y & \sigma_y^2 \end{pmatrix}$ where ρ is the correlation parameter between the noise in x and y. The "true" line on which all "true" points lie is parametrized by $(x = r\cos\theta, y = r\sin\theta + b)$, where b is the intercept point of the line with the y axis and $m = \tan\theta$. A point (x_i, y_i) is then measured with probability

$$\begin{aligned} p(x_i, y_i|r, \theta, b) &= \exp(-\frac{1}{2}((\mathbf{x_i} - \mathbf{x})^T\Sigma^{-1}(\mathbf{x_i} - \mathbf{x}))) \\ &= e^{-\frac{1}{1-\rho^2}\left(\frac{(x_i - r\cos\theta)^2}{2\sigma_x^2} + \frac{((y_i-b)-r\sin\theta)^2}{2\sigma_y^2} - \frac{\rho(x_i - r\cos\theta)((y_i-b)-r\sin\theta)}{\sigma_x\sigma_y}\right)} \end{aligned}$$

where $\mathbf{x} = \begin{pmatrix} x \\ y \end{pmatrix}$ and $\mathbf{x_i} = \begin{pmatrix} x_i \\ y_i \end{pmatrix}$.

We have one "extra" parameter indicating that now, even if we know the slope θ and the bias b of the linear relation, we still can't know from where along the line the point (x_i, y_i) originates, i.e. we do not know the "true" value of r. Having no prior assumption about the "true" position of the measurement (x_i, y_i) along the line, we can only regard it as having an equal probability to have originated anywhere along the "true" line, and thus get rid of it simply by tracing it out by integration $\int dr$. We use the relation $\int_{-\infty}^{\infty} e^{-(ar^2+br+c)}dr = \sqrt{\frac{\pi}{a}}e^{(b^2-4ac)/4a}$ and obtain

$$p(x_i, y_i|\theta, b) = \# \times e^{-\frac{(x_i\sin\theta-(y_i-b)\cos\theta)^2}{2(\sigma_x^2\sin^2\theta+\sigma_y^2\cos^2\theta-2\rho\sigma_x\sigma_y\sin\theta\cos\theta)}}$$

with # a normalization factor that do not effect the optimization. The complete probability, considering the complete measurement set is $p(\{x_i, y_i\}|\theta, b) = \Pi_i p(x_i, y_i|\theta, b) = e^{-\chi^2(\{x_i,y_i\},\theta,b)}$, and the optimum is again achieved by minimization of χ^2 with respect to b, θ. In fitting for the experimental data, the uncertainties σ_x, σ_y and the correlation parameter ρ were estimated using the data itself, separately for each experimental run at a given trap power, with each containing 12-16 independent, sequential Ramsey measure-

ments. The confidence intervals for the detuning that were obtained from the fit to the Ramsey time sequences themselves were comparable to the scatter in the data, but these were not used since the procedure to obtaining from the nonlinear least squares fitting program we used was not transparent.

By measuring the shift for each of the three principal magnetic field directions, **x**, **y** and **z**, and for several trap power setpoints, we obtain two equivalent data sets, δ_{zx} and δ_{zy} both as function of δ_z. We fit each with a line $y = mx + b$ using the method outlined above, and get

$$m_{zx} = 0.0125 \pm 0.0010 \quad ; \quad b_{zx} = 0.02 \pm 0.14$$
$$m_{zy} = 0.0139 \pm 0.0085 \quad ; \quad b_{zy} = -0.21 \pm 0.13$$

with the uncertainty being one standard deviation to either side, see Fig.32. Unfortunately there is a slight disagreement between the two slopes, on order of the statistical uncertainty (the 1σ confidence regions are nearly touching). In addition, the bias inferred from the second (z-y) data set is not consistent with zero, as could be expected from an ideal experiment. Having no preference to either one of the two configurations, we propose to treat both results on equal footing by just taking the average slope. We have decided to take a **very** conservative approach regarding the confidence interval for the combined result and to use the union of the two confidence intervals for the two independent results, i.e. the upper bound is taken from the larger slope obtained for the z-y experiment, and the lower bound is taken from the lower slope, obtained for the z-x experiment, see Fig.32:

$$m = 0.0132^{+0.0015}_{-0.0017} \quad ; \quad b = -0.09^{+0.26}_{-0.24}$$

We could not give a satisfactory explanation to the discrepancy between the slopes, and also the biases, as obtained from two equivalent experiments. One cause for the shift in bias and not slope, that comes to mind, is a systematic calibration error for the magnetic field, causing the field when aligned along **x** to be different from the field along **y**. However, the field was measured using the atoms as probes, and no systematic shift was found between the directions. At most, a drift of few hundreds of Hertz in the first order Zeeman shift

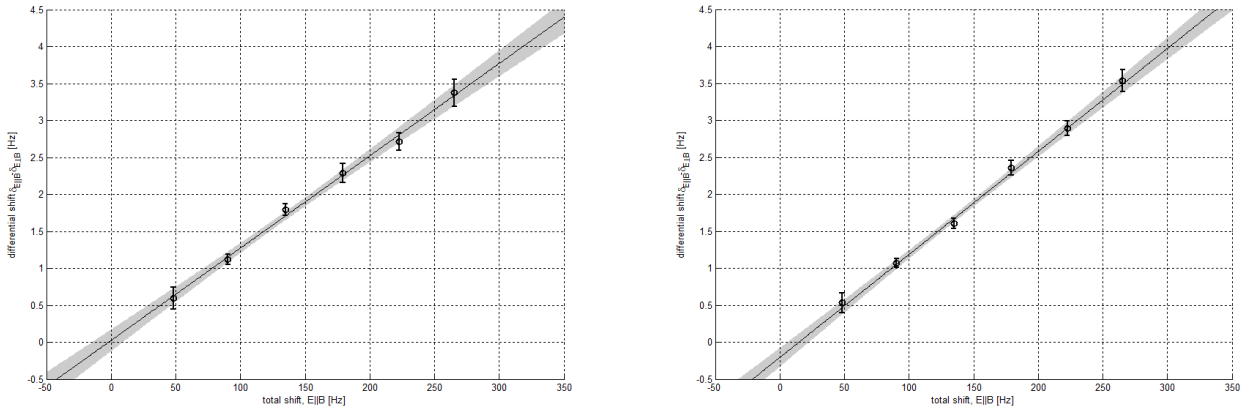

(a) (b)

Figure 31: (a) result of the z-x experiment $m_{zx} = 0.0125 \pm 0.0010; b_{zx} = 0.0024 \pm 0.14$ (b) result of the z-y experiment $m_{zy} = 0.0139 \pm 0.0085; b_{zy} = -0.20 \pm 0.13$. Combining the two results, treating them both as equally likely we get $m = 0.0132^{+0.0015}_{-0.0017}$; $b = -0.09^{+0.26}_{-0.24}$. The plotted data points are mean values for each trap power, the uncertainties are $\sigma/\sqrt{N}$ where N is the number of measurements at each trap power setting. The uncertainties on the total shift, plotted on the x-axis, are on the same order but cannot be seen in this scale. The shaded area contains all the linear fits with m,b values contained within the $\chi^2 = 1$ ellipse of the fit.

was detected ($<$1mG), bringing about less than 0.05Hz deviation from the second order Zeeman shift chosen for the experiment, at 2.93Hz (from a 50kHz first order Zeeman shift at a bias magnetic field of 71.4mG). Another possible cause could be misalignment between the direction along which the field is applied and the unit vectors defined by the linear polarization of the trap beam, $\hat{\varepsilon}$, the propagation direction of the beam, $\hat{k}$ and $\hat{k} \times \hat{\varepsilon}$. We assume that $\hat{x} \parallel \hat{k}$, $\hat{z} \parallel \hat{\varepsilon}$ and $\hat{y} \parallel \hat{k} \times \hat{\varepsilon}$ but errors in alignments may have occurred. This kind of error can only explain the different slopes, not the different bias found for the two experiments. The amount of misalignment, however, required to produce the discrepancy between the two measured slopes is much larger than could have gone unobserved. We discuss several possible systematic shifts in more detail in the paragraphs below.

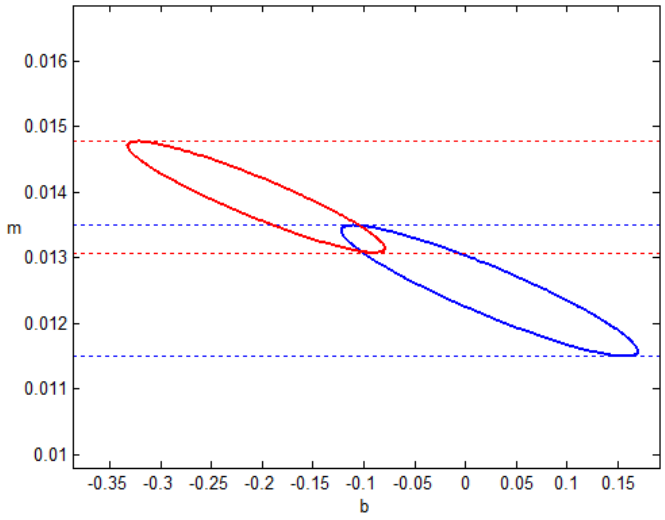

Figure 32: $\Delta\chi^2 = 1$ ellipses in the b-m plane for each experiment, blue: z-x experiment, red: z-y experiment. The dashed lines represent the projection of the confidence ellipse onto the one dimensional confidence interval for the slope, m. For the combined result from the two independent experiments we use the union of the two 1D confidence intervals, i.e. the interval between the upper dashed red line and the lower dashed blue line.

4.4 Systematic effects

There are some systematic effects that require attention.

First, while the clock transition does not suffer from the first order Zeeman effect, there is still a second order Zeeman shift of 575.15Hz/G^2. During the measurement we have repeatedly measured and calibrated the magnetic field at the position of the dipole trap, before taking each set of three Ramsey traces. This interlaced method insured that any random deviation (due to error in the calibration procedure) will be averaged and will only contribute to the scatter in the measured data. The calibration itself was done measuring the shift of the first magnetic sensitive transition and adjusting the current in the compensation coils such that a shift $\Delta f = 50 \pm 2\,\mathrm{kHz}$ is obtained, so the corresponding field is $|\mathbf{B}| = 71 \pm 3$ mG and the uncertainty in the 2nd order Zeeman shift on the clock transition is $\Delta f_{clk} = 2\mathrm{B}\Delta\mathrm{B} \times 575.15\,\mathrm{Hz/G}^2 = 0.235$ Hz. The adjustment to the currents is done using a pre-measured calibration factor and not in closed loop. The second order Zeeman shift, assumed common to all measurements is therefore $\delta_B = 2.93 \pm 0.23$ Hz. Any constant error in the measured value of the magnetic field for each of the three magnetic directions will only serve to shift the linear relation of Fig.31, and therefore will only effect bias, b. This is true whether the magnetic error is common to all directions, then the shift will be horizontal, or differential between a pair of the magnetic directions, then the linear realtion will be shifted vertically. It could be that the different bias observed for the z-x and the y-z measurements is due to a constant magnetic calibration error of the magnetic field in the y direction, nevertheless, this cannot explain the different measured slope. We use the calibration measurements of the magnetic field, done between Ramsey experiments to estimate the long term drifts in the magnetic field in all three directions, and attempt to better compensate the frequencies we measure in the Ramsey experiments according to the calculated second order Zeeman, at the time of the Ramsey experiment.

A second source for systematic error has to do with the measurement method itself. The atoms are trapped and so density shifts are present. We have tried to minimize the uncertainty in the atomic density by simply reducing the number of trapped atoms to a minimum while keeping a decent enough signal. The measured thermodynamic properties of the trapped atoms are given in table 2, the density can be calculated $n_0 = N\frac{m^{3/2}\omega_r^2\omega_z}{(2\pi kT)^{3/2}}$,

assuming a perfectly harmonic trap. The number of trapped atoms is directly measured by analyzing the same absorption images used for the Ramsey measurement. The temperature is obtained from the same data by using the decay constant K from the fit itself $K = \frac{2\hbar}{\eta k_B T}$. The radial trap oscillation frequency ω_r is measured directly by measuring the breathing mode frequency for several trap powers (generally $\omega_r \propto \sqrt{p_{trap}}$), shown in Fig.20 . This is done by abruptly turning the trap off and on again within $100\,\mu$s and then looking at the width of the atomic cloud after a TOF of approximately $300\,\mu$s. The calculated density shift was always below -0.5Hz[12, 19] and the uncertainty in this shift, based on the shot to shot fluctuations in the measured number of trapped atoms, is well below 0.1Hz. Again, this systematic shift is common between measurements done at the same trap power and so has no effect on the measured slope, nevertheless, we do use the calculated density shifts to correct the each of the frequency shift measurements. A source of error of greater importance could come from a calibration error in the trapped atoms number. If the number of trapped atoms is systematically over or under-estimated by a multiplicative factor, then the density shift will be wrong by the same factor. Since for our experiment the number of trapped atoms is roughly monotonic with the trap depth this kind of error could in fact cause a systematic error in the measured slope, by shifting different points in Fig.31 horizontally, in some proportions to their x-axis values. I was not able to determine if there is actually an error in the measured number of atoms. Even if allowing the density to be 10 times what actually measured, and also take the worst case, i.e. linear, dependence of the NOA on the trap power, we end with a 3Hz shift for the most shifted measurement point. Naturally the density shift is common for different magnetic field orientations and so the measurements are shifted horizontally, linearly with their total shift (a worst-case assumption). The effect would be to increase the slope by less than 1%, with 1% uncertainty on this systematic effect.

A third systematic error has to do with misalignment of the magnetic coils with respect to the three "natural" axes defined by $\hat{\varepsilon}$,$\hat{k}$ and $\hat{k} \times \hat{\varepsilon}$ will have an effect of lowering the measured value of the full tensor shift. For example, looking at the z-x experiment, and using Eq.(18), small alignment errors $\delta\theta_{x,z} \ll 1$ will have the effect of changing the slope in the following way $\xi_{misaligned} \approx 3\frac{\alpha^T_{clock}}{\alpha^S_{clock}}(1-\delta\theta_z^2-\delta\theta_x^2)$. From the construction of the magnetic coils we can estimate that they are centered better than 1cm at a distance of approx 20cm

from the atoms, allowing to bound the misalignment between the magnetic $\hat{x}$ direction and the trapping laser propagation direction $\hat{k}$ at $\delta\theta_x \lesssim \frac{1}{20} = 50$mrad. Similarly, assuming we can make sure that the $\hat{z}$ axis is exactly perpendicular to $\hat{x}$, and almost parallel to the polarization we have $\delta\theta_z \approx 50$mrad. Similarly $\delta\theta_y \approx 50$mrad. The orthogonality of the three magnetic axes was verified by first calibrating each them to a field of 40kHz and then activating them in pairs $(x+y, y+z, z+x)$. The measured magnetic field from each pair is then $B = \sqrt{2}B_0\sqrt{1+\cos(\alpha)}$ where α is the angle between the coils in the pair. For orthogonal coils we should get $B = \sqrt{2}B_0 = 56.6\,\mathrm{kHz}$. The Measured fields are within 1kHz of this value, Fig.33, and so the orthogonality between the coils is estimated to be better than 50mrad.

Yet another source for a systematic decrease of the measured tensor shift could arise from the angle between the optical axis (mean $\hat{k}$) and the electric field, i.e. deviations from the paraxial approximation. For an infinite plane wave the paraxial approximation is exact and this angle is always $\pi/2$ and need no consideration, however, we use a tightly focused beam where the local propagation direction may deviate significantly from the mean $\hat{k}$. The atoms are spread in a trap formed by a tightly focused beam, and if the cloud is too large, it may sample regions were the plane wave approximation at the focus is no longer valid. The size of this effect can be estimated and bounded to show that it is indeed a negligible effect. We know the radial and axial extents of the cloud $\sigma_z^2 = \frac{kT}{2U_0}z_r^2$, and $\sigma_r^2 = \frac{kT}{4U_0}w_0^2$. For the conditions encounterd in the experiment $\sigma_z < 0.25z_r$, $\sigma_r < 0.16w_0$. The beam width is given by $w(z) = w_0\sqrt{1+(\frac{z}{z_r})^2}$ and the derivative gives the angle at each axial coordinate $\delta\theta \approx \tan\delta\theta = \frac{dw}{dz} = \frac{w_0}{z_r}\frac{z/z_r}{\sqrt{1+(z/z_r)^2}}$. For our estimated waist $w_0 \approx 30\mu$m and $z < \sigma_z/2$ this angle is smaller than 15mrad at the beam edge ($\delta\theta^2 < 2.25\times10^{-4}$), and much smaller than that at the edge of the cloud. We conclude that deviations from the paraxial approximation near the focus of the trapping beam do not contribute to the error budget, compared with other systematics, most importantly, misalignment of the beam and magnetic field, or when comparing to the statistical errors.

Finally the trap laser may be of polarization not purely linear. Measurements done in our lab has put a bound on the linearity of the laser of better than 1 to 50 , consistent with the extinction ratio of the polarizer we could use for the measurement (we have a thin

film polarizer from II-VI) . A > 1 to 100 bound is provided by the manufacturer (this is a C55-L laser from Coherent). With an imperfect linear polarization $E_z^2 < E^2$ whichever the orientation of the magnetic field, thereby lowering the measured value of the tensor shift, see Eq.17. A second effect has to do with the vector polarizability shift, undiscussed until now. In [9] the author has calculated the effect of the vector differential polarizability of the clock transition for various atomic species, including ^{87}Rb, with the objective of using it to cancel the scalar shift, thereby getting rid of inhomogeneous broadening and the associated decoherence. In a related experiment [10] this was implemented with the effect of extending the coherence to many seconds. This is done by using a circulary polarized beam and setting the magnetic field to some "magic" value that depends on the trap laser wavelength. We refer to [9] and find the value of the magnetic field required to make the vector shift equal in magnitude to the scalar to be 41G, for ^{87}Rb trapped in a CO_2 trap. The effect is linear in the magnetic field, so for our applied field of 71mG the vector shift, for a purely circularly polarized trap laser, is just 1.7×10^{-3} that of the scalar, an order of magnitude smaller than the full tensor shift. For our laser, of almost pure linear polarization the circularity is probably < 0.1 and the effect is reduced by another order of magnitude, making it negligible.

The corrected value, including the most important systematic effects is

$$\xi_{meas} = 3\frac{\alpha^T_{clock}}{\alpha^S_{clock}} = 0.0133\,^{+0.0015}_{-0.0017 stat}\,^{+0.0006}_{-0.0000 syst}.$$

As it seems, at this rate of statistical uncertainty the small alignment and polarization imperfections do not hamper the measurement significantly, and the uncertainty in our measurements are dominated by statistical noise.

4.5 Conclusion

We have isolated and measured the shift caused by the tensor part of the differential polarizability of the magnetic insensitive hyperfine clock transition in ^{87}Rb. The experiment was conducted by performing Ramsey spectroscopy on a sample of cold atoms trapped in the intense quasi-static field at the focus of a CO_2 laser, at an accuracy allowing the

observation the 1-3Hz shift between two orthogonal direction of the quantizing magnetic field. While our experiment was the first to utilize this exact method, other experiments, as early as 1969, were conducted using atomic beam methods rather than trapped atoms. In [15] the experiment was done by passing the atomic beam between between the plates of high voltage electrodes creating a large DC field, and by measuring the frequency shift of the "flop in" transition between Zeeman substates ($|F=2,m=1\rangle \longleftrightarrow |F=2,m=2\rangle$), under a fixed magnetic field of 1G. This is not, however, a measurement of the tensor shift of hyperfine clock transition, with its obvious significance for the Rb atomic time standard. Another result related to our measurement comes from [11] were the authors have calculated the scalar and tensor HFI polarizabilities for several alkali atoms, including Rb and Cs. They compared their value for the tensor HFI polarizability of Cs to the experimentally measured value and found their result is off by about 30%. They have concluded that this error was due to the numerical method they have used and so recommended to correct also the value calculated for Rb by the same amount. Looking at the results of this theoretical calculation with $\xi'_{corrected} = 0.0153$, and $\xi'_{uncorrected} = 0.0119$, we note that our experimental result is nicely bracketed between the two, but closer to the uncorrected result. We hope that the availability of new experimental data could help advance the efforts of atomic physics theoreticians attempting to calculate ab-initio, the properties of alkali atoms.

We recognize some imperfections in the experimental method, to be corrected in a future realization of the experiment. First, since under the assumption of a linearly polarized trap beam the direction of the magnetic field could be reversed without an effect. This should be verified by flipping the magnetic field direction between measurements. Such a measurement could also serve to directly measure the vector part of the polarizability, since it will contribute to a shift between opposite direction of the magnetic field. Another difficulty is recognized when analyzing the data. We do not understand the discrepancy between the z-x and z-y experiments. We could not find any concrete evidence to a systematic effect within the data we took. For example, with the discrepancy in slope being 10%, a misalignment between trap beam and magnetic coil will have to be on the order of $\sqrt{0.1} = 0.3$rad or 17°. This is a huge misalignment that could not have gone unnoticed.

description	magnitude	effect on ξ	uncertainty
misalignment **k**,**x**	$<$50mrad	-0.25%	0.25%
misalignment **E**,**z**	$<$50mrad	-0.25%	0.25%
deviation from the paraxial approximation	$<$15mrad	0.02%	0.02%
polarization non-linearity	$<$0.02	-2%	2%
vector shift	depends on shift	2×10^{-4}	2×10^{-4}
density shift (worst case, 10$\times$ exaggerated)	$<$3Hz	+1%	1%
second order Zeeman shift	2.93$\pm$0.23Hz	no effect	n/a

Table 1: Systematic errors in the measurement of tensor to scalar fractional shift

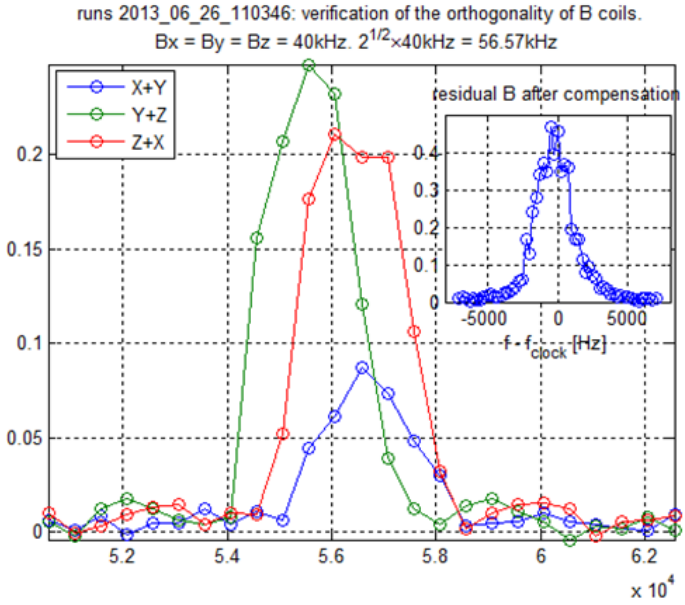

Figure 33: Measurement of the magnetic coils orthogonality using the applied field felt by the atoms. The peaks belongs to the $|F = 1, m = 0\rangle \rightarrow |F = 2, m = 1\rangle$ transition. The variation in the height of the peaks results from the different Rabi frequencies with the magnetic field aligned along each of the three principle axes. In the inset is the MW spectrum in the absence of an applied magnetic bias, with the peak belonging to all the visible transitions confined to less than 4kHz, showing that the filed in the absence of applied bias is very nearly null

CO_2 trap power	12W	6W	3W
$\omega_r/2\pi$	2950Hz	2040Hz	1390Hz

(a)

trap set point [W]	0.75	1.5	2.25	3	3.75	4.5
T [μK] (as obtained from fit to Ramsey decay, $K = \frac{2\hbar}{\eta k_B T}$)	16	14	21	27	28	34
NOA (shot to shot fluctuations of about 20%, std. dev. 10%)	3800	17800	17100	12500	21000	18700
$\omega_r/2\pi$ ($\omega_z \approx 0.1\omega_r$), $\omega \propto \sqrt{p}$	700	935	1183	1390	1576	1742
density [cm^{-3}]	3.4e10	5.6e11	5.5e11	4.1e11	9.1e11	7.9e11
density shift [Hz]	-0.01	-0.22	-0.21	-0.16	-0.35	-0.31
coll rate [s^{-1}]	1.2	19	23	19.5	44	41

(b)

Table 2: (a) trap frequencies, extracted from the measurement in fig.20 (b) measured and derived thermodynamic properties of trapped atoms

4.6 Can we reduce the uncertainty by uses of dynamical decoupling?

Following the initial success in measuring the relative tensor to scalar shifts we try to aim a little higher. Can we use methods such as spin echo or quantum lock-in to reduce the uncertainty in our measurement? Our typical Ramsey coherence time K is close to 20ms, and is limited by the requirement of minimizing the density shift while keeping a reasonable number of trapped atoms (few 10,000). A simple quantity representing the measurable signal is just the differential phase accumulation due to the tensor shift after a Ramsey decay time K: $\Delta\phi = \delta_T K$. The density shift is proportional to the density itself $n_0 = N\frac{m^{3/2}\omega_r^2\omega_z}{(2\pi kT)^{3/2}}$. With the trap oscillation frequency obeying $\omega \propto \sqrt{P} \propto E \propto \sqrt{\delta_T}$ where P is the trapping beam power, E is the electric field and $K = \frac{2\hbar}{\eta k_B T}$, we can relate the density to the accumulated phase difference by $n_0 = CN\delta_0^{\frac{3}{2}}K^{\frac{3}{2}} = CN(\Delta\phi)^{\frac{3}{2}}$ where C is a constant. When density broadening is significant, and processes such as collisional narrowing become important, Eq. (19) can no longer be used accurately describes the experimental Ramsey signal and our measurement strategy fails. The result is that $\Delta\phi$ cannot be increased by cooling the atoms further, without greatly complicating the measurement. Of course,

it is possible to reduce both the temperature and the number of atoms while keeping the density constant, but this will result in larger detection errors, necessitating massive averaging.

A possible solution to this problem is the use of a lock-in technique. By modulating the small tensor shift in sync with the applied echo pulses we should be able to measure a much larger signal, potentially up to a π phase shift [[24]]. There are two ways to accomplish this: either the polarization of the trapping laser or the direction of the magnetic field can be periodically rotated, and in either way the $3E_z^2$ term of Eq. (18) is modulated. Due to technical reasons we initially modulated the magnetic field direction.We implemented a system of coils, controlled by FPGA to be able to apply an arbitrary magnetic field vector. The control electronics are also able to rotate the magnetic field during the experimental sequence while keeping $|\mathbf{B}|$ constant. Such rotations can take as little as 1.5ms for a 90deg rotation. Unfortunately, when testing the systems on our trapped atoms we found out that while the DC operation of the magnetic control is satisfactory, its transient properties were not so. The rapidly changing magnetic fields induce eddy currents in our metal (stainless steel and copper) vacuum chamber, causing the magnetic field to change much slower (10ms-20ms timescales, depending on orientation, see figure 34) than planned or expected. Since the echo pulse must be applied at predetermined directions of the magnetic field (i.e at 90deg intervals) we have to wait for the eddy currents to subside, and this waiting time causes the dynamical decoupling to be ineffective because of loss of coherence from collisions and other factors, not remedied by the echos.

Giving up on the magnetic rotation method, and armed with an ancient half wave plate for $10.6\mu m$ (newly excavated from the dungeons of Asher Frism) we decided to try to rotate the polarization of the trapping laser while keeping the magnetic field constant during the experiment. To this end we are currently designing a fast waveplate rotator that will enable us to quickly rotate the polarization vector and allow dynamic techniques, and also to align the waveplate statically at any angle so that a measurement similar to the original Ramsey experiment (with the magnetic field statically aligned at different directions) can be done.

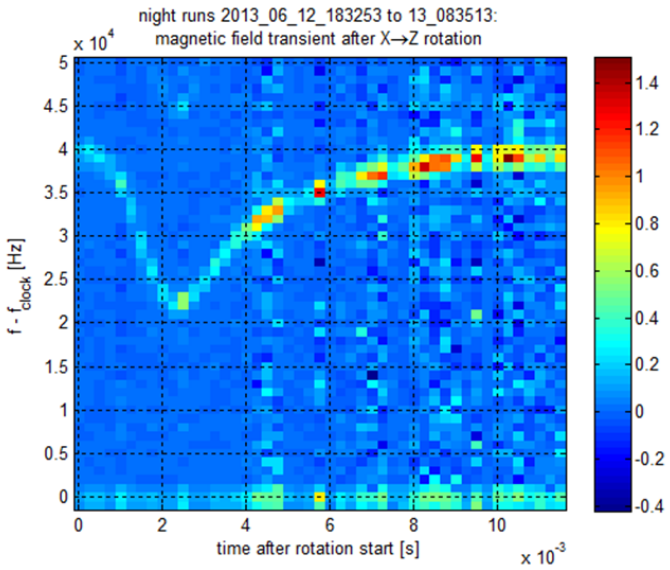

Figure 34: A magnetic field transient following a rotation of the applied magnetic field by 90 degrees. The transient is thought to be caused by eddy currents circulating in the metal parts of the vacuum chamber.

5 Laser spectroscopy on the $5S_{\frac{1}{2}} - 5P_{\frac{1}{2}}$ ("S-P") transition

In addition to MW spectroscopy we have also experimented briefly with laser spectroscopy of the trapped atoms. The goal was to to measure the shift in the $S_{\frac{1}{2}} \rightarrow P_{\frac{3}{2}}$ transition, compare it to the scalar shift in the clock transition (section 4.1), and extract the ratio between the two polarizabilities. While preliminary results looked promising, we could not get the accuracy we aimed for in measuring the shift ($<1\%$ is needed to improve on the measured value of the scalar polarizability) and decided to put the project aside for the time being, concentrating our efforts on the tensor vs scalar project described above. I give here a short overview of the experimental technique and the model describing the results.

The technique we used was spin-relaxation spectroscopy. In such an experiment, the atoms were loaded into the quasi-electrostatic trap in the F=1 ground state. Shortly ($<$1ms) before the measurement was done they are pumped into the F=2 state by a pulse of repumping light (resonant with F=1→F'=2). This preparation pulse is at a relatively

high intensity ($I \approx I_{sat}$) and is long enough to make sure that all the atoms are transferred into the F=2 state. Immediately following this preparation pulse, a spectroscopy pulse is applied, this time at a frequency close to the F=2→F=1 transition, transferring atoms to the F=1 hyperfine manifold. The power of this beam is monitored and recalibrated at each realization of the experiment, to compensate for variations in coupling efficiency to the single mode fiber delivering the light, and the frequency dependent efficiency of the double-pass acousto optical modulator, used to scan the frequency of the spectroscopy laser pulse. Following the spectroscopy pulse on the optical pumping transition the atoms are released from the trap and subsequently the fraction of the atoms remaining in the F=2 state is measured using normalized absorption imaging (described in sections above) and plotted against the frequency of the spectroscopy pulse to obtain a spectrum. This method, of using an optical pumping transition, rather than a closed transition, to interrogate the trapped atoms, ensures that a minimal number of photons is scattered, only two on average, with a minimal heating by the laser.

The shape of the trapped atoms spectrum is given by a convolution two functions, the first being the spectrum of free atoms and the second is the distribution of energies for trapped atoms, $\rho(\delta) = \sum_i \rho_{free}(\delta - \delta_{ls}^i)$ where the sum is over the individual atoms, and δ_{ls}^i is the transition lightshift of atom i at the moment of interrogation. The spectrum of free atoms can be derived as follows. Neglecting the finite linewidth of the laser and ignoring that the transition is not closed, the photon scattering rate is $R = \frac{\Gamma}{2}\frac{I/I_{sat}}{1+I/I_{sat}+4(\frac{\Delta}{\Gamma})^2}$. After the scattering of a photon there is a probability p to find the atom in the F=1 state, and a probability $q = 1 - p$ that the atoms remain in the F=2 state. The probability p need not remain constant during the optical pumping process and may depend in principle on the polarization of the optical pumping laser and the direction of the quantizing magnetic field, and also on the initial distribution of the atoms along the five Zeeman states of the F=2 hyperfine level. We shall ignore all these factors and retain only an empirical p, q that will be determined from a fit to the data. The probability for an atom to remain in the F=2 state after the probe pulse has passed is the probability that all the scattering events left the atom in its initial state: $P_{F=2} = (1-p)^N = q^{Rt_{pulse}} = q^{\frac{\Gamma}{2}\frac{I/I_{sat}}{1+I/I_{sat}+4(\frac{\Delta}{\Gamma})^2}t}$, where N is the mean number of scattered photons. This is the same probability as obtaining a series of N "heads" when flipping a biased coin with probabilities p, q (since even a single "tail"

result will change the probabilities to $p = 1, q = 0$ because of the optical pumping action of the probe beam). In principle Γ, q and I/I_{sat} are known, but in reality this model is over simplistic and also I/I_{sat} is dependent on probe alignment polarization etc. Therefore, in analyzing the data for free atoms we keep I/I_{sat} as a fitting parameter, and allowing for an error in the setting frequency of the probe laser, $\delta \to \delta - \delta_{0,free}$. We finally obtain a function that should be used in fitting the spectra of free atoms:

$$\rho_{free}(\delta) \quad = \quad e^{-\frac{a}{b+4(\frac{\delta-\delta_{0,free}}{\Gamma})^2}}.$$

Although the finite linewidth of the laser was not taken into account in this derivation, the function fit quite well with the measurement, as seen in a typical result in figure 36a.

The energy distribution of trapped atoms, provided that the interrogation time is short enough to effectively freeze atomic motion in the trap, should be identical to the *potential energy distribution* for atoms in a 3D harmonic trap, derived in section (2.4). For our experimental parameters $t_{pulse} \ll \omega_{trap}^{-1}$ ($\omega_{trap}^{-1} \approx 360\mu$s, $t_{pulse} = 10\mu$s) this "snapshot" model correctly describes the experiment. The trapped spectrum will therefore be a convolution between the free spectrum and this potential energy distribution, scaled and shifted in frequency as $\hbar\delta = \eta(V - V_0) = \frac{\alpha_{D2}}{\alpha_0}(V - V_0)$ where V_0 is the trap depth and α_{D2} is the differential polarizability of the $S_{\frac{1}{2}} - P_{\frac{3}{2}}$ transition (D2 line) determining the detuning of the transition for an applied electric field and α_0 is the polarizability of the ground state which determines the trap depth. The distribution for the detunings of atoms trapped in a 3D harmonic trap is thus given by:

$$\rho_{trapped}(\delta) = \# \times \sqrt{\delta - \delta_0} e^{-\frac{\hbar(\delta-\delta_0)}{\eta k_B T}}; \text{ for } \delta > \delta_0$$

To be able to fit this distribution to the data we must first convolve it with the distribution for free atoms, measured in a separate experiment. We define a fitting function as a numerical convolution between the best fitting distribution for free atoms and a test function with δ_0 and T as free parameters and use nonlinear least squares program to find a fit to the data, see Fig 36b. The values of the fitted are given in table 3. Unfortunately, when using the known value of $\eta = 1.6877$ [47], the temperature we got from the fit failed

to agree by other methods, such as MW spectroscopy done in the same experimental conditions or simple TOF measurements. Actually, the "temperature" found from the fit to the spectral function was larger by approximately a factor of two from the other, reference TOF and MW measurements. We could not give a satisfying explanation for this discrepancy and decided to stop pursuing this effort.

Although we didn't, eventually, performed the measurement taking interleaved laser spectroscopy measurements of the S-P shift and MW spectroscopy measurements of the hyperfine scalar shift, with the interleaving intended to minimize the effect of technical drifts in the experimental parameters on the result, we did have two MW measurements taken not long (10 days) after the laser spectroscopy session. By plotting the scalar shift against the trap power setpoint at which they were taken, and doing the same for the S-P shifts we obtain two slopes. The ratio between the two slopes is a measurement of the ratio between the differential hyperfine polarizability and the differential S-P polarizability. The result of these linear fits are

$$\begin{aligned} m_{MW} = 45.7 \pm 0.5\text{Hz/W} \quad ; \quad b_{MW} = 32 \pm 4\text{Hz} \\ m_{SP} = 2.88 \pm 0.05\text{MHz/W} \quad ; \quad b_{SP} = 0.30 \pm 0.33\text{MHz} \end{aligned}$$

the bias for the MW measurement can be explained as a combination of 15Hz second order Zeeman shift (calculated from the magnetic bias of 113kHz or 161mG) and an additional trap power calibration error of $\Delta P = \frac{-17\text{Hz}}{45.7\text{Hz/W}} = -0.37\text{W}$. The bias for the S-P measurement can be similarly attributed to a calibrational shift of -0.1W, but is not significant with respect to other uncertainties. The quite different calibration detected by considering the shift with respect to the trap beam power setpoint at which they were measured are a warning regarding the validity of the data, and indeed, when looking at the ratio between the slopes, it disagrees at the 15% level with the ratio between the polarizabilities, as measured previously [47, 37]:

$$\begin{aligned} \frac{m_{MW}}{m_{SP}} &= (1.58 \pm 0.03) \times 10^{-5} \\ \frac{\alpha_{HF}}{\alpha_{D2}} &= (1.850 \pm 0.013) \times 10^{-5} \end{aligned}$$

Trapping laser power	12W	6W	3W
S-P Spectroscopy shift [MHz]	34.0 (33.2, 34.7)	17.1 (16.8, 17.4)	8.3 (7.5, 9.1)
S-P spectroscopy T[uK]	163 (146, 180)	88 (78, 98)	44 (32, 57)
TOF T[uK]	67 (63, 71)	45 (40, 50)	22 (19, 25)

Table 3: 95% confidence interval is given in parenthesis

Unfortunately, we did not have the opportunity to complete this experiment and maybe be able to resolve the different discrepancies with a more careful experimental method.

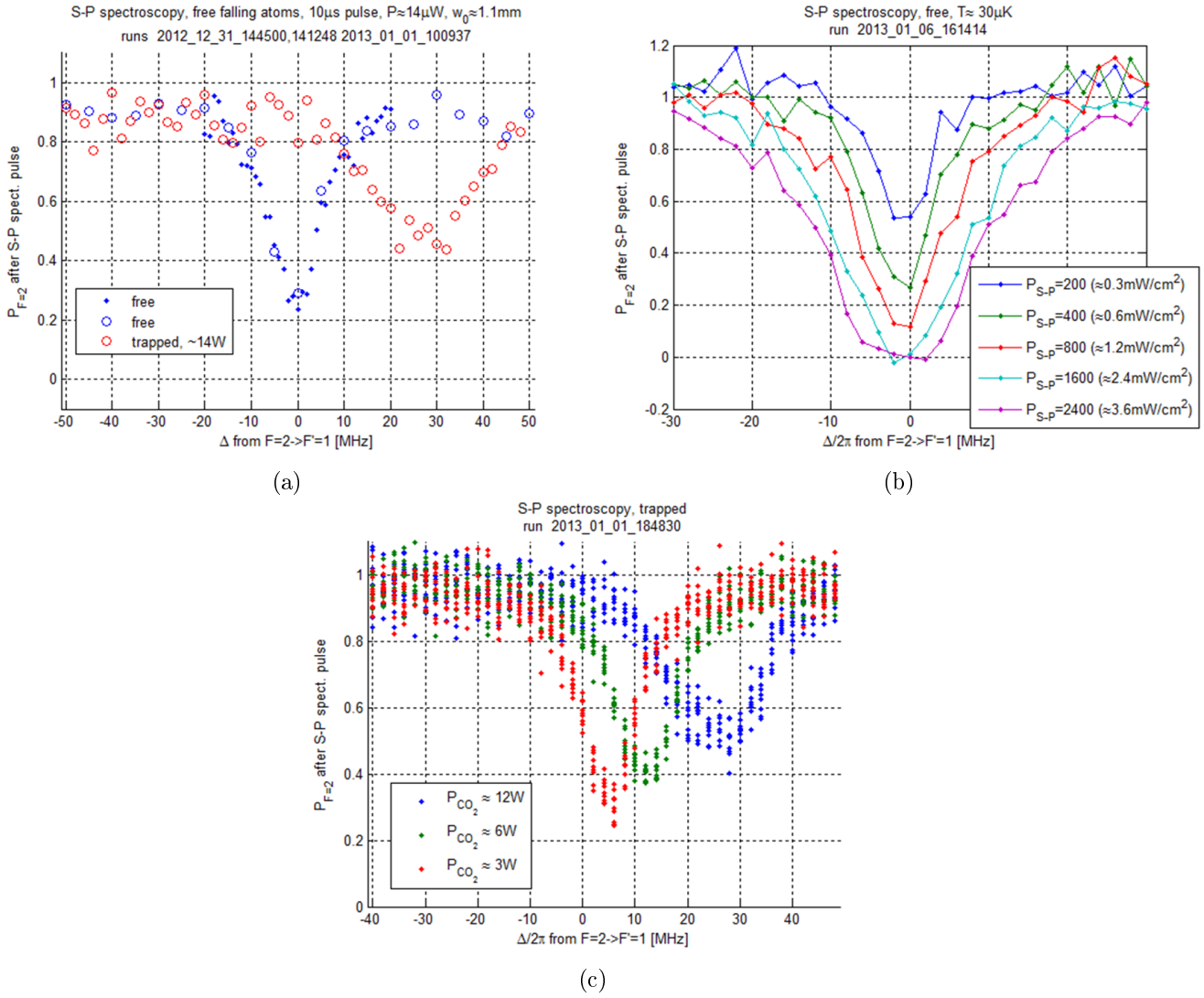

Figure 35: **(a)** Laser spectroscopy of free (blue) and trapped (red) atoms. A shift of about 30MHz and significant broadening are apparent for the trapped atoms. **(b)** spectroscopy of trapped atoms using various probe powers. For high enough intensity the transition is saturated with significant broadening as a result. For spectroscopy probe power should be kept to a minimum allowing a detectable signal. **(c)** spectroscopy of trapped atoms in different trap powers. The shift and also the line width is dependent on the trap depth. The asymmetry in the line shape is expected: there is a bottom to the trap.

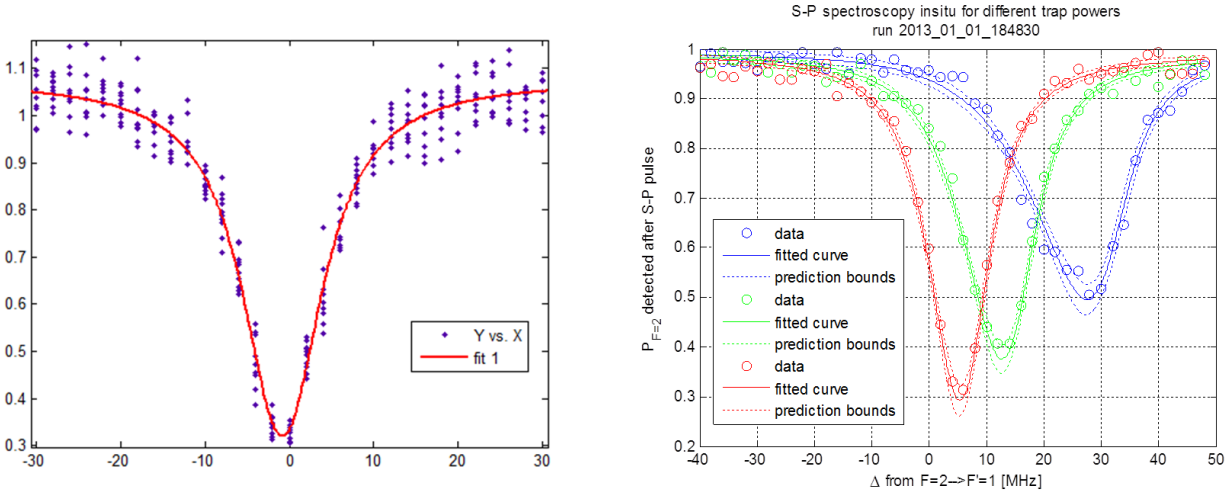

(a) (b)

Figure 36: **(a)** spectrum for free atoms. we use this "kernel" spectrum when making a fit for trapped atoms spectrum. **(b)** spectra obtained for trapped atoms in various trap powers. The spectrum for each trap is a convolution of the light shift distribution and the free atoms spectrum.

6 Effects of a dynamic quantization axis

The "tensor shift" experiment of section 4 was done by measuring the shifts with three orientations of the magnetic field and then substructing them to reveal the effect of the tensor polarizability. We have tried to implement another approach to this differential measurement, in which the difference between the shifts with the magnetic field parallel or perpendicular to the trap electric field is measured directly. This can be done by rotating the field during the Ramsey sequence such that in the interval $T_{Ramsey}/2 < t < 0$ the magnetic field points one way (say along the **z** axis) and in the second the interval $T_{Ramsey} < t < T_{Ramsey}/2$ the magnetic field points along a perpendicular direction (say **x**). If an echo π pulse is placed at $T_{Ramsey}/2$ the overall phase is only due to the differential shift, and equals $\phi_{zx} = \frac{1}{2}\left(\delta_z T_{Ramsey} - \delta_x T_{Ramsey}\right)$ and the common scalar shift is automatically canceled. Any decoherence due to inhomogeneity in the atomic population is removed and the fringe contrast will depend on other noise processes. A still better scheme would be to use a pulse sequence with many π pulses and rotate the magnetic field

between any two pulses, thus extending the coherence to even longer times by fighting decoherence due to collisions, fluctuations in the trap laser power, magnetic field noise and other noise processes **[1]**. This will allow to increase the sensitivity by increasing the measured phase, which is proportional to the measurement time. While this scheme may sound simple, it requires a well controlled magnetic field vector that can be rotated in a time short compared to the Ramsey time.

After some work on the electronics driving the compensation coils generating our bias magnetic field we were in a situation that we were able to point the magnetic field vector along any direction in 3D with its magnitude stabilized. We were also able to draw any trajectory in the 3D magnetic space in timescales of a few ms. However, further investigation revealed that our control over the magnetic field was limited. The total field was a combination of the (well controlled) applied field and a transient magnetic field due to eddie currents, generated in the many conducting surfaces near the atoms (specifically in very low resistance copper gaskets used for sealing the vacuum chamber). These eddie currents are very slow to dissipate (decay times of 20ms have been observed) and in effect limit the rate at which magnetic fields can be changed controllably. At this point we also noticed that the phases we were measuring were much larger than what could be expected due to the tensor shift. With a typical shift of 2Hz (see Fig.31) and a Ramsey time of 40ms one could expect a phase of 0.25 rad or 14° . However, phases approaching 90° were observed, and these were independent of T_{Ramsey}, but did depend on the direction of rotation and even on the sense of the rotation! Clearly some other effect we did not originally consider was involved.

Finally we realized the cause for these unexpected phases (trivial effects may still be well disguised). As mentioned in section 2.5, the polarization of the MW field that couples between the two ground state hyperfine manifolds is generally not linear, but has some degree of ellipticity. This could be the case even if the antenna or horn used to radiate the MW into the cell is designed to emit linearly polarized MW radiation, because of reflections from nearby conductors. For our setup it was impossible to make sure that there isn't some MW reflected in a phase different than the emitted radiation and in the orthogonal polarization, mainly because the dimensions of our metallic vacuum chamber are comparable with the MW wavelength of $\approx$ 4cm. When the polarization isn't linear,

the direction of the quantization axis, determines the phase and magnitude of the matrix element of interaction Eq.(8) and Eq.(9). The matrix element amplitude determines the Rabi frequency and its phase. This has no consequence as long as the quantization axis remains constant during the length of a MW spectroscopy experiment, specifically between the two $\pi/2$ pulses in a Ramsey experiment. However, when several MW pulses are issued with the quantization axis different between the pulses this direction dependent phase must be taken into account. When designing the experiment we have thought of our MW source as being of linear polarization. Then it is expected for the Rabi frequency on the clock transition to change for different directions of the quantizing magnetic field, according to the projection of the MW oscillating field vector on the quantization axis, but for an elliptically polarized MW field the phase might also depend on the direction of the quantization axis. Moreover, for a linearly polarized MW field there exist a plane, perpendicular to the direction of the oscillating magnetic field, that by aligning the quantization axis anywhere in this plane the Rabi frequency vanishes. If the quantization axis crosses this plane the phase is inverted by 180°. For an elliptically polarized MW field this degenerate plane is reduced to a single line, perpendicular to the plane defined by the ellipse. It may be actually beneficial in some circumstances to use non linear polarization for the MW field, for example, when placing the quantization axis anywhere in the plane defined by the polarization axis, the MW field can be considered linear, but if a circularly polarized MW field is desired, one need to only point the quantization axis along a direction from which the polarization ellipse appears circular (or that the projection of the ellipse on the plane perpendicular to it is a circle). The relevant planes can be found by measurements of the kind described below.

We have preformed measurements of both phase and amplitude of the Rabi frequency as a function of the direction of the quantizing magnetic field. While the magnitude of the interaction can be measured in a static experiment, in which a long MW pulse is issued with the quantization axis fixed and frequency of the resulting Rabi oscillations is found, the phase, being a relative quantity, can only be detected in a transient experiment. This was achieved with the following experimental sequence: for some direction of the quantizing magnetic field (e.g. $\mathbf{x}$) a $\pi/2$ pulse is given. We then adiabatically rotate the magnetic field: $t_{rot} \gg \frac{1}{\mu_B B}$, by an angle θ, around the $\mathbf{z}$ or $\mathbf{y}$ axes. After a time $T/2$ in which the

rotation is completed and eddy currents have decayed (now the quantization axis is steady again), we apply a π pulse. Following another interval $T/2$ a second $\pi/2$ pulse is issued, with a phase ϕ w.r.t the first pulse. The durations of the different MW pulses are adjusted to account for the dependence of the Rabi frequency on the direction of the quantization axis, to insure the correct pulse area. The inclusion of an echo pulse guarantees that the phase at the end of the sequence is solely due to the change in quantization axis direction and not due to some detuning. It also allows us to make the rotations of the magnetic field slow, minimizing the transient eddy currents that accompany rapidly changing magnetic fields and wait for these currents to die out, while undoing decoherence due to inhomogeneous broadening. The results of such scans are shown in Fig.37 and data extracted from these raw measurements is shown in Fig.39 and Fig.38. The measurements for the Rabi frequency phase and amplitude can be combined to get a trace showing the projection of the MW field on the plane on which $\mathbf{B}$ was scanned, as in Fig.40. This can be thought of as a projection of the polarization ellipse on the plane of rotation. By repeating this experiment with the quantization axis rotated around three orthogonal axes (and confined to the corresponding planes), complete information regarding the MW polarization at the location of the trapped atoms can be obtained.

We noted that for rotations of the quantization axis on the **y**-**z** plane (around the **x** axis) the phase exhibits a sharp transition, almost 45° in only 9° rotation of the quantization axis. This is due to the **y** axes being almost parallel to the major axis of the ellipse. We can increase the sharpness of the transition while keeping the Rabi frequency non-zero by choosing an adequate rotation plane, close to being perpendicular to the polarization ellipse itself. The increased sharpness of the feature comes with a cost of reduced Rabi frequency close to it, with infinitely sharp transition (with zero Rabi frequency at the same angle) when the planes are exactly perpendicular, or alternatively, for an almost linear MW field. Generally a sharp transition of a measurable quantity with respect to variation in some experimental parameter is a desired property of a system, since it enables measuring small changes in the parameter. For example, a change of 1° in the direction of the quantization axis in the experiment described in Fig.38 will result in almost 5° change in the measured phase. By choosing correctly the relative directions of the magnetic quantization and the MW fields an even sharper transition can be engineered and even smaller fluctuations of

the quantization axis measured. The problem of a lower Rabi frequency near a sharp transition is not really a limiting factor since the power of the MW signal can be increased by orders of magnitude (by using a powerful enough MW amplifier). With our system we could extend the coherence time to the $\approx$ 100ms using a single echo pulse. This is far from being state of the art and other similar experiments has achieved much longer coherences by better controlling the noise sources in the experiment. Combining a long coherence time with a large sensitivity to changes in the direction of the magnetic field, we should be able to measure very slow rotations of the magnetic field. This is amusing when recalling that this sensitivity is achieved by using a magnetic *insensitive* transition!. Indeed - the large susceptibility to magnetic field noise of the magnetic sensitive transitions render them useless for the measurement of slow magnetic field variations, since without an extremely well controlled magnetic environment, these states will decohere in a short time scale. As an example, typical magnetic noise of one mG at 50 Hz would dephase magnetic sensitive transitions after a millisecond or so [25].

As an example, consider a the following situation. Usually when doing MW spectroscopy a bias magnetic field, $\vec{B}_0$, is applied, to create a well defined quantization axis and introduce some separation, due to Zeeman splitting, between the different magnetic levels m. Now, suppose you want to measure another field, $\vec{B}_1$, which is much smaller in magnitude than the applied bias $\left|\vec{B}_1\right| \approx \left|\vec{B}_0\right|/100$, and is turned on slowly in a time τ_{on}, starting at $t = 0$. Suppose we can arrange things such that the two fields are orthogonal $\vec{B}_1 \perp \vec{B}_0$, and that the MW is of nearly linear polarization (a very elongated polarization ellipse) so that a plane with a sharp phase transition exist. We also arrange that $\vec{B}_0$ is parallel to the minor axis of the polarization ellipse and $\vec{B}_1$ is parallel to the major axis. Then, by turning on the field $\vec{B}_1$ the magnetic quantization axis is rotated by an angle $\theta \approx \frac{B_1}{B_0} = 0.01\text{rad} \approx 0.6^\circ$. By performing a Ramsey sequence with an echo pulse included we can detect this slight rotation, for our system this rotation will translate into 3° phase difference, but this can be improved by an order of magnitude by making the MW polarization more linear and increasing the MW intensity to compensate for the reduced Rabi frequency (we want the pulse to be short w.r.t. to other timescales in the problem). While turning on $\vec{B}_1$ results in a significant rotation of the quantization axis, the change in the magnetic field magnitude is negligible: $\left|\vec{B}_0 + \vec{B}_1\right| = B_0\sqrt{1 + 0.01^2} = 1.00005$. We

can estimate the sensitivity of this method, using the numbers from our experiments. We used a bias magnetic field of B_0 =40kHz (57mG). Therefore an orthogonal field of only 400Hz (0.6mG) will cause a phase shift of 3° in our system, or as much as 30° in an improved system. From other, unrelated, calibration measurements (Fig.41), we estimate the detectable phase shift to be of order 2.3° (assuming detection noise of $\approx 2\%$ of the population at the maximal slope of the fringe, assuming 50% contrast $\Delta\phi = \frac{\Delta p}{0.5\times\frac{d}{d\phi}\cos(\phi)|_{\phi=\pi/2}}$). The sensitivity improves linearly with the fringe contrast or the detection noise. With a fringe contrast of 50% we could measure as slowly as 40ms (limited by loss of coherence), so rotations as slow as $60°/s$ can be measured, or orthogonal field variation as small as 35mG/s (at the specified applied bias field).

While a similar experiments were conducted by [48] with the same conclusion, i.e. that the phase observed when rotating the magnetic quantization axis is just the phase of the driving field, they used a linearly polarized drive field and could only observe a phase of π. We on the other hand, by using elliptically polarized MW field, could observe a smooth dependence of the phase of the Ramsey fringe on the the direction of the magnetic field. It is nice to think of the quantization axis as a "needle" that can read the phase difference between two directions, or projections, of the MW field driving the transition.

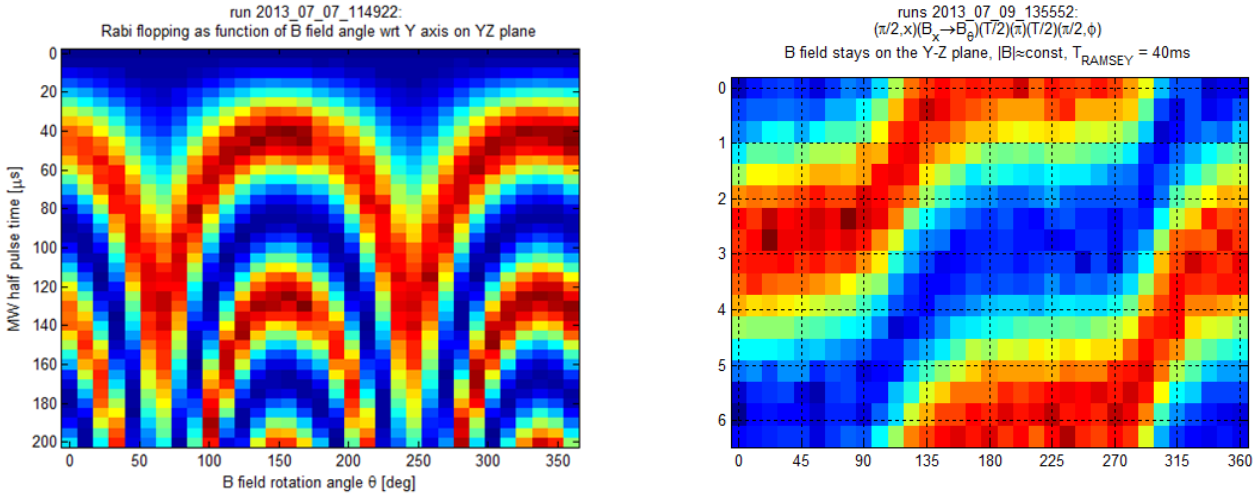

(a) (b)

Figure 37: Here the direction of **B** is scanned in the ZY plane (a) Raw data from Rabi flopping measurement (b) Raw data from a fringe phase scan

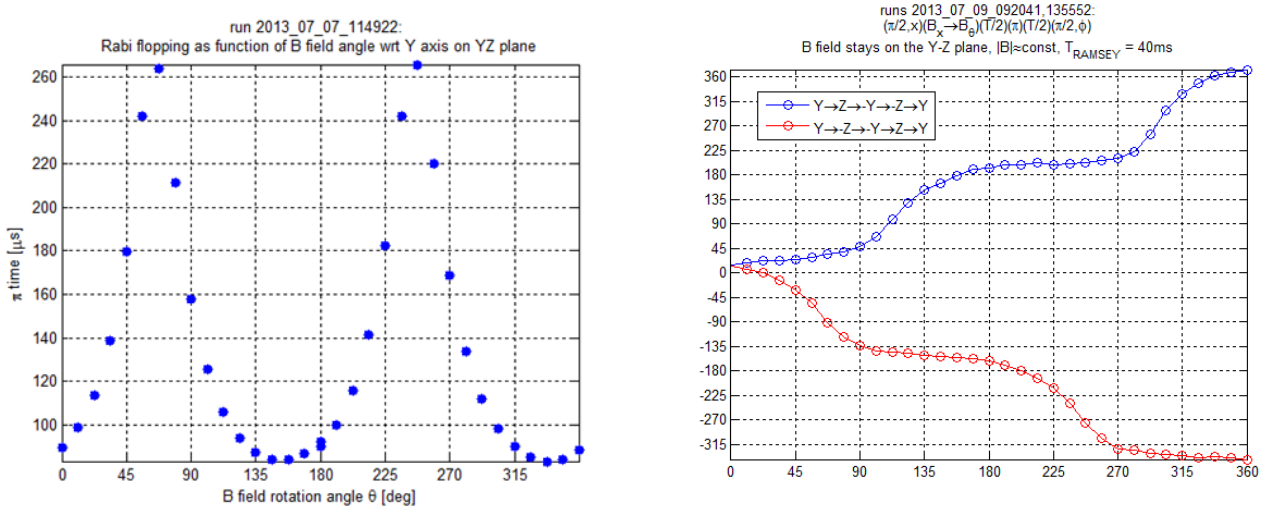

(a) (b)

Figure 38: The direction of **B** is scanned in the YZ plane. (a) π time extracted from a fit to the raw data. It varies from about 86us to over 260us when going through 90 deg: a factor of 3 in the Rabi frequency indicates that the projection of the MW on the YZ plane is an ellipse with aspect ration of 3, close to being linear. (b) fringe phase extracted from the raw data demonstrates almost staircase form with π phase jumps.

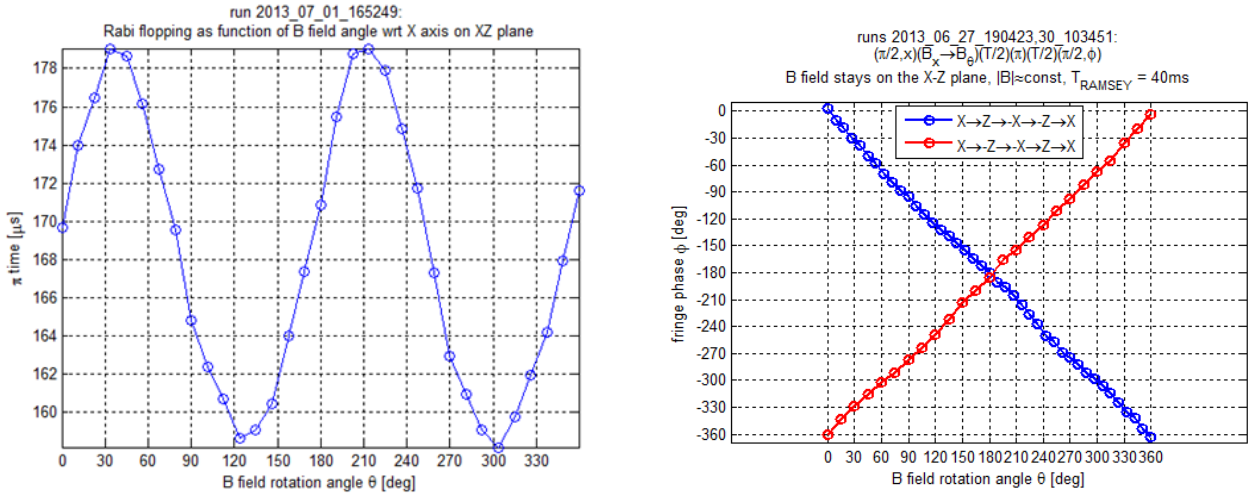

(a) (b)

Figure 39: The direction of **B** is scanned in the XZ plane. (a) π time extracted from a fit to the raw data. The Rabi frequency hardly changes indicating that the projection of the MW ellipse on this plane is nearly circular. (b) fringe phase with **B** scanned in the XZ plane showing nearly linear dependence on the relative direction of **B** between the two Ramsey pulse

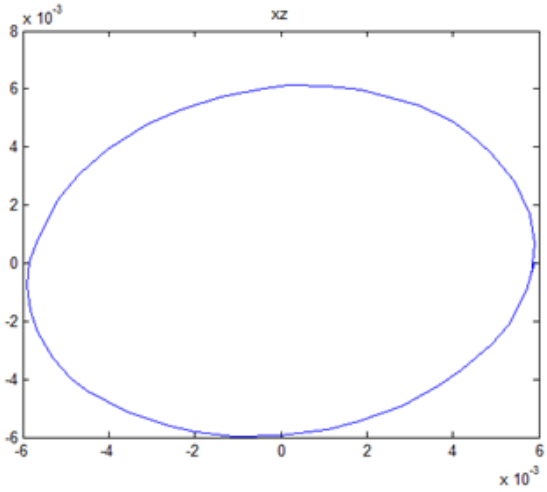

Figure 40: Rabi freq in MHz on the XZ plane. The projection is indeed nearly circular

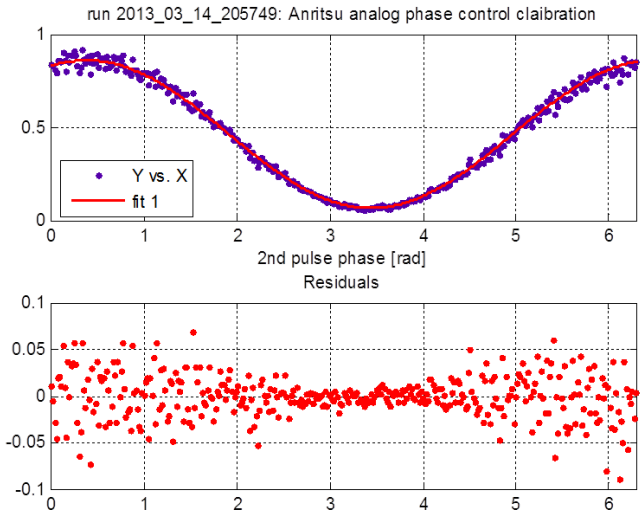

Figure 41: A calibration measurement showing the experimental sensitivity for Ramsey fringe phase.

7 Conclusions and prospects

This project was only the first part in a long and complicated journey, and even now, almost five years after work has begun, the goal of studying the interactions between ultracold, optically trapped, ^{87}Rb atoms and trapped, ground state cooled, $^{88}Sr^{+}$ ions, is still not within reach. But still, enormous progress was made. Five years ago the project has begun with the mechanical design of a complicated vacuum system, consisting of two chambers connected together, one for collecting and cooling atoms, the other housing a Paul trap for the trapping of ions. Many constraints had to be considered, together with decisions that were made regarding the technologies that will be used, for example, by deciding to use an optical conveyor belt (a running-standing wave trap) to transport the atoms from the neutral chamber into the ions chamber, we have constraint the system to be in a vertical configuration, rather than perhaps a more convenient planar arrangement. The choice of optical transport was again a result of our concern with magnetically trapping and transporting the atoms, in an environment infested with uncontrolled oscillating RF fields of the Paul trap. Optical transport demands that the center of both traps is

connected by line of sight, and not too far apart, since the distance is determined by the diffraction of the transport beam. The choice of a CO_2 trap for the atoms was due to its relatively simple, single beam configuration, and the promise of a robust system having the minimal number of variables. It was also assisted by the availability of industrial CO_2 lasers of very good beam quality, high powers and convenient prices. By choosing a CO_2 laser we had to go with a stainless-steel vacuum chamber with viewports for 10μm radiation, and wanting to have a decent optical access to the atoms we used a chamber with 10 viewports, thereby increasing the chance for leaks. I could go on, but the idea is clear - there are many constraints and the design of such a system is not a walk in the park. Nevertheless, today, after the addition of a second Ph.D student to the project, that took on himself the design on an ion trap and the construction of the second half of the vacuum system we are finally at a point where the two chambers are connected, each one is operating with its own cold species, neutral or charged, and work is underway to construct the optical transport system and bring the two together.

While the atoms chamber was not originally designed with any specific, standalone, experiment in mind, It have realized that a unique opportunity has presented itself. As far as we knew, this was the only system possessing both quasi-electrostaticaly trapped atoms, with MW spectroscopy capabilities (originally added to solve an annoying magnetic bias). With the atoms subjected to the strong fields created by the trapping laser, we had hoped to be able to measure, besides the obvious stark shift of the ground state, responsible for the trapping, a more subtle effect, that of the differential stark shift between the hyperfine states of the ground state. Moreover, we thought, we should be able to observe the even smaller tensor contribution of this differential shift, recently calculated by Dzuba et al. [ref]. By this, we were hoping to show that value of a CO_2 trap, not only as a convenient micro-scale "jar" for atoms, but also at a more fundamental level, that of a strong field that can perturb the atoms and reveal their inner structure. I should be noted that we did not use the maximal power available for the trap, only reaching fields of order 10^6V/m with a 3W beam. A modest 100W laser (CO_2 lasers are available up to the kW range) focused to a spot of 30μm can reach an RMS field of 5×10^6V/m. This is equivalent to the field between two plate electrodes at a distance of 1cm, charged to 50kV, but the problem with the latter setup is that discharges are bound to happen and surface roughness, as well as mechanical

vibrations of the plates will appear as noise in the experiment. The use of pulsed, rather than CW lasers for forming a trap could also be considered. A pulsed laser operating at several hundreds of kHz with an average power of few watts can form a trap, just as well as a CW laser, since the time scales related to the atomic motion in the trap are much longer, and only the time averaged light shift determines the trapping potential. Nevertheless, such a laser can deliver very high peak powers, allowing to perform experiments with very high fields on trapped atoms. For example - the linear dependence between the intensity and the shift is a very good approximation at low fields, but a departure from it can be experimentally studied by using the large fields of a pulsed laser. This requires a light shift of the order of the hyperfine interaction $\frac{1}{2}\alpha_0 E^2 \sim h \times 6.8\text{GHz}$, then the dipole energy can no longer be treated as a perturbation to the Hamiltonian and must be taken into account together with the hyperfine interaction, and a dressed states approach will be more appropriate. Such fields could be reached with a 5kW peak power laser focused to a 30μm waist, not far from what can be obtained from commercially available lasers such as the Coherent E-1000, a pulsed CO_2 laser operating at 200kHz with a peak power of 2.5kW. Trapping the atoms using a pulsed laser may have some technical advantages as well. For example, the light shift is only active during the short pulse, leaving the atoms essentially free in between pulses, with no inhomogeneous broadening effects. Therefore laser cooling methods optimized for free atoms, such as polarization gradient or sisyphus cooling , can used in between pulses, with an appropriate synchronization scheme. Finally, laser spectroscopy experiments that can be done in short pulses, shorter than the interval between the trap laser pulses, will greatly benefit from the use of pulsed laser trap. An experimental sequence for performing laser spectroscopy on cold trapped atoms while having no inhomogeneous broadening due to the trap could be suggested as follows, with all the cooling, pumping and spectroscopic pulses operated only in between trap pulses: after collecting atoms in the trap, issue a strong pumping pulse to the F=2, in the next dark interval issue a weak spectroscopy pulse on the depumping transition, similar to the experiment described in section 5, then on the next "free atoms" window issue a detection pulse resonant with only the F=2 atoms. The sequence can then be completed with few cycles of laser cooling, to return to situation before the spectroscopy pulses were issued. This could be repeated for many many times allowing for averaging and integration of the

signal, also for scanning the spectroscopy laser frequency, all done without releasing the atoms from the trap.

Referring to the "effects of a dynamic quantization axis" experiment, this was quite a detour that originated with the effort perfect our control over the applied magnetic field. Our cold, trapped, atoms were not the subject of this experiment, but were rather just used as probes of the MW phase and the angle through which the magnetic field was rotated. This represents a second face of cold atoms experiments, that of utilizing cold atoms as probes that are used to measure some physical quantity, such as atomic magnetometers or atomic gravitometers. We have made extended use of this approach, for example, when using the atoms as magnetic field probe, enabling us to apply an accurate magnetic bias, exactly in the location were it mattered - the location of the trapped atoms themselves. This approach is extended in the measurement of the tensor shift versus the scalar shift. In effect we have used the light shift experienced by the very same atoms on which the tensor shift was to be measured to measure the field of the trapping laser, instead of attempting to measure the field using some method external to the atoms, e.g. by a calibrated power detector or a thermal camera.

Declaration of Independent Research

I hereby declare that all the experimental results presented in this thesis were obtained by my own independent research.

APPENDIX A

Matlab code used in the fringe removal algorithm of section 3.8:

```
function [OD_F12,OD_F2] = RemoveFringesNormAbsV1(I_ref_F12,I_ref_F2,I_data_F12,I_data_F2,atoms_subsX,atoms_subsY)
%OD_F12: optical density image of the total population
%OD_F1 : OD image of the F=2 pop
%I_ref_F12: matrix of dimensions [n_pixel_y,n_pixel_x,n_images]. stack of references images for the total populations
%I_ref_F12: matrix of dimensions [n_pixel_y,n_pixel_x,n_images]. stack of references images for the F=2
%I_data_F12: matrix of dimensions [n_pixel_y,n_pixel_x,n_images]. stack of absorption images for the total populations
%I_data_F2: matrix of dimensions [n_pixel_y,n_pixel_x,n_images]. stack of absorption images for the F=2
%atoms_subsX: columns containing atoms
%atoms_subsY: rows containing atoms
%the image of the atom cloud is confined to the region (atoms_subsY,atoms_subsX). the rest is considered to be
     background

N = 30; %using only 30 adjacant photos to reconstruct fringes. much more distant photos are irrelevant and compromises
     performance.

sz = size(I_ref_F2);

[XX,YY] = meshgrid(atoms_subsX,atoms_subsY);

indatoms = sub2ind(sz(1:2),YY(:),XX(:));
allind = [1:sz(1)*sz(2)];
allind(indatoms) = 0;
ind_bg = find(allind>0);

mat_OD12 = zeros(sz);
mat_OD2 = zeros(sz);

R2  = (reshape(I_ref_F2   ,[sz(1)*sz(2),sz(3)]));
D2  = (reshape(I_data_F2  ,[sz(1)*sz(2),sz(3)]));
R12  = (reshape(I_ref_F12   ,[sz(1)*sz(2),sz(3)]));
D12  = (reshape(I_data_F12  ,[sz(1)*sz(2),sz(3)]));

for ii = 1:sz(3)
    ind_first = max(1,ii-N/2);
    ind_last  = min(ind_first+N,sz(3));
    if sz(3)>N
        ind_first = min(ind_first,ind_last-N);
    end
    ind = ind_first:ind_last;

    mf_R2_  = mean([R2(:,ind)],2);
    mf_R2 = repmat(mf_R2_,[1 length(ind)]);

    mf_R12_  = mean([R12(:,ind)],2);
    mf_R12 = repmat(mf_R12_,[1 length(ind)]);

    cntR12 = R12(:,ind) -mf_R12;
    cntR12 = cntR12./(ones(sz(1)*sz(2),1)*std(cntR12));

    cntR2 = R2(:,ind) -mf_R2;
    cntR2 = cntR2./(ones(sz(1)*sz(2),1)*std(cntR2));

    cntD2= D2(:,ii) - mf_R2_;
    cntD12= D12(:,ii) - mf_R12_;
    %first: treat the fringes in the F=2 images.
    C2 = cntR2'*cntR2;
    [VV2,DD2] = eig(C2);
    EE2 = diag(DD2);
    validvecs2  = EE2>1;

    efv2 = cntR2*VV2;
    efv2 = efv2(:,validvecs2)*sqrt(diag(1./EE2(validvecs2)));
    proj02 = mf_R2_'*efv2; %this is the projection of the mean face on the eigenfaces found.
    mf_R2_orth = mf_R2_ - efv2*proj02';%we find one extra eigenface which is orthogonal to the others. This contains
         information about noise in the direction of the mean face.
    efv2 =  [efv2 mf_R2_orth/sqrt(sum(mf_R2_orth.^2))];

    %now for the fringes in "toatal population" images
    C12 = cntR12'*cntR12;
    [VV12,DD12] = eig(C12);
    EE12 = diag(DD12);
```

```
    validvecs12  = EE12>1;

    efv12 = cntR12*VV12;
    efv12 = efv12(:,validvecs12)*sqrt(diag(1./EE12(validvecs12)));
    proj012 = mf_R12_'*efv12; %this is the projection of the mean face on the eigenfaces found.
    mf_R12_orth = mf_R12_ - efv12*proj012';%we find one extra eigenface which is orthogonal to the others.
    efv12 =  [efv12 mf_R12_orth/sqrt(sum(mf_R12_orth.^2))];
    %final step: reconstruct fringes for each image using only the area which does not contain the atoms (ind_bg)
    proj2 = cntD2(ind_bg)'*(efv2(ind_bg,:));
    newR2 = efv2*proj2'+mf_R2_;
    vec_OD2 = log(newR2)-log(D2(:,ii));
    mat_OD2(:,:,ii) = reshape(vec_OD2,sz(1:2));

    proj12 = cntD12(ind_bg)'*(efv12(ind_bg,:));
    newR12 = efv12*proj12'+mf_R12_;
    vec_OD12 = log(newR12)-log(D12(:,ii));
    mat_OD12(:,:,ii) = reshape(vec_OD12,sz(1:2));

    disp(['fringe removal on image #' num2str(ii)])
end

OD_F12 = mat_OD12;
OD_F2 = mat_OD2;
toc
```

References

[1] Ido Almog, Yoav Sagi, Goren Gordon, Guy Bensky, Gershon Kurizki, and Nir Davidson. Direct measurement of the system -environment coupling as a tool for understanding decoherence and dynamical decoupling. *Journal of Physics B: Atomic, Molecular and Optical Physics*, 44(15):154006, 2011.

[2] B. P. Anderson and M. A. Kasevich. Loading a vapor-cell magneto-optic trap using light-induced atom desorption. *Phys. Rev. A*, 63:023404, Jan 2001.

[3] M. H. Anderson, W. Petrich, J. R. Ensher, and E. A. Cornell. Reduction of light-assisted collisional loss rate from a low-pressure vapor-cell trap. *Phys. Rev. A*, 50:R3597–R3600, Nov 1994.

[4] J. R. P. Angel and P. G. H. Sandars. The hyperfine structure stark effect. i. theory. *Proceedings of the Royal Society of London. Series A. Mathematical and Physical Sciences*, 305(1480):125–138, 1968.

[5] George B. Arfken and Hans J. Weber. *Mathematical Methods For Physicists International Student Edition, Sixth Edition*. Academic Press, 2005.

[6] M. D. Barrett, J. A. Sauer, and M. S. Chapman. All-optical formation of an atomic bose-einstein condensate. *Phys. Rev. Lett.*, 87:010404, Jun 2001.

[7] Murray Barrett. *A QUEST for BEC : An all optical alternative*. PhD thesis, Georgia Institute of Technology, 2002.

[8] G. Cennini, G. Ritt, C. Geckeler, and M. Weitz. Bose-einstein condensation in a co2-laser optical dipole trap. *Applied Physics B: Lasers and Optics*, 77:773–779, 2003. 10.1007/s00340-003-1333-1.

[9] Andrei Derevianko. Theory of magic optical traps for zeeman-insensitive clock transitions in alkali-metal atoms. *Phys. Rev. A*, 81:051606, May 2010.

[10] Y. O. Dudin, R. Zhao, T. A. B. Kennedy, and A. Kuzmich. Light storage in a magnetically dressed optical lattice. *Phys. Rev. A*, 81:041805, Apr 2010.

[11] V. A. Dzuba, V. V. Flambaum, K. Beloy, and A. Derevianko. Hyperfine-mediated static polarizabilities of monovalent atoms and ions. *Phys. Rev. A*, 82:062513, Dec 2010.

[12] Chad Fertig and Kurt Gibble. Measurement and cancellation of the cold collision frequency shift in an ^{87}Rb fountain clock. *Phys. Rev. Lett.*, 85:1622–1625, Aug 2000.

[13] B. Fröhlich, T. Lahaye, B. Kaltenhäuser, H. Kübler, S. Müller, T. Koch, M. Fattori, and T. Pfau. Two-frequency acousto-optic modulator driver to improve the beam pointing stability during intensity ramps. *Review of Scientific Instruments*, 78(4):043101, 2007.

[14] T. Gericke, P. Wurtz, D. Reitz, C. Utfeld, and H. Ott. All-optical formation of a bose einstein condensate for applications in scanning electron microscopy. *Applied Physics B: Lasers and Optics*, 89:447–451, 2007. 10.1007/s00340-007-2862-9.

[15] H. Gould, E. Lipworth, and M. C. Weisskopf. Quadratic stark shift between zeeman substates in ^{133}Cs, ^{87}Rb, ^{85}Rb, ^{39}K, and ^{23}Na. *Phys. Rev.*, 188:24–29, Dec 1969.

[16] R. Grimm, M. Weidemüller, and Y. B. Ovchinnikov. Optical Dipole Traps for Neutral Atoms. *Advances in Atomic Molecular and Optical Physics*, 42:95–170, 2000.

[17] J. Guena, P. Rosenbusch, P. Laurent, M. Abgrall, D. Rovera, G. Santarelli, M.E. Tobar, S. Bize, and C. Clairon. Demonstration of a dual alkali rb/cs fountain clock. *Ultrasonics, Ferroelectrics and Frequency Control, IEEE Transactions on*, 57(3):647–653, 2010.

[18] E. L. Hahn. Spin echoes. *Phys. Rev.*, 80:580–594, Nov 1950.

[19] D. M. Harber, H. J. Lewandowski, J. M. McGuirk, and E. A. Cornell. Effect of cold collisions on spin coherence and resonance shifts in a magnetically trapped ultracold gas. *Phys. Rev. A*, 66:053616, Nov 2002.

[20] D. W. Hogg, J. Bovy, and D. Lang. Data analysis recipes: Fitting a model to data. *ArXiv e-prints*, August 2010.

[21] Joshua Hughes and Chad Fertig. A widely tunable laser frequency offset lock with digital counting. *Review of Scientific Instruments*, 79(10):–, 2008.

[22] A Kaplan, M F Andersen, T Grünzweig, and N Davidson. Hyperfine spectroscopy of optically trapped atoms. *Journal of Optics B: Quantum and Semiclassical Optics*, 7(8):R103, 2005.

[23] Wolfgang Ketterle, Kendall B. Davis, Michael A. Joffe, Alex Martin, and David E. Pritchard. High densities of cold atoms in a *dark* spontaneous-force optical trap. *Phys. Rev. Lett.*, 70:2253–2256, Apr 1993.

[24] Shlomi Kotler, Nitzan Akerman, Yinnon Glickman, Anna Keselman, and Roee Ozeri. Single-ion quantum lock-in amplifier. *Nature*, 473(7345):61–65, May 2011.

[25] Shlomi Kotler, Nitzan Akerman, Yinnon Glickman, and Roee Ozeri. Nonlinear single-spin spectrum analyzer. *Phys. Rev. Lett.*, 110:110503, Mar 2013.

[26] S. Kuhr, W. Alt, D. Schrader, I. Dotsenko, Y. Miroshnychenko, A. Rauschenbeutel, and D. Meschede. Analysis of dephasing mechanisms in a standing-wave dipole trap. *Phys. Rev. A*, 72:023406, Aug 2005.

[27] Xiaolin Li, Min Ke, Bo Yan, and Yuzhu Wang. Reduction of interference fringes in absorption imaging of cold atom cloud using eigenface method. *Chin. Opt. Lett.*, 5(3):128–130, Mar 2007.

[28] N. Lundblad, M. Schlosser, and J. V. Porto. Experimental observation of magic-wavelength behavior of ^{87}rb atoms in an optical lattice. *Phys. Rev. A*, 81:031611, Mar 2010.

[29] HaroldJ. Metcalf and Peter Straten. Graduate Texts in Contemporary Physics. Springer New York, 1999.

[30] J. Richard Mowat. Stark effect in alkali-metal ground-state hyperfine structure. *Phys. Rev. A*, 5:1059–1062, Mar 1972.

[31] N. R. Newbury, C. J. Myatt, and C. E. Wieman. s-wave elastic collisions between cold ground-state ^{87}Rb atoms. *Phys. Rev. A*, 51:R2680–R2683, Apr 1995.

[32] C. F. Ockeloen, A. F. Tauschinsky, R. J. C. Spreeuw, and S. Whitlock. Detection of small atom numbers through image processing. *Phys. Rev. A*, 82:061606, Dec 2010.

[33] C. Ospelkaus, U. Rasbach, and A. Weis. Measurement of the forbidden tensor polarizability of cs using an all-optical ramsey resonance technique. *Phys. Rev. A*, 67:011402, Jan 2003.

[34] William H. Press, Brian P. Flannery, Saul A. Teukolsky, and William T. Vetterling. *Numerical Recipes in C: The Art of Scientific Computing, Second Edition*. Cambridge University Press, 1992.

[35] Norman F. Ramsey. Experiments with separated oscillatory fields and hydrogen masers. *Rev. Mod. Phys.*, 62:541–552, Jul 1990.

[36] G. Ritt, G. Cennini, C. Geckeler, and M. Weitz. Laser frequency offset locking using a side of filter technique. *Applied Physics B*, 79(3):363–365, 2004.

[37] M. S. Safronova, Dansha Jiang, and U. I. Safronova. Blackbody radiation shift in the ^{87}Rb frequency standard. *Phys. Rev. A*, 82:022510, Aug 2010.

[38] Yoav Sagi, Ido Almog, and Nir Davidson. Universal scaling of collisional spectral narrowing in an ensemble of cold atoms. *Phys. Rev. Lett.*, 105:093001, Aug 2010.

[39] Yoav Sagi, Rami Pugatch, Ido Almog, and Nir Davidson. Spectrum of two-level systems with discrete frequency fluctuations. *Phys. Rev. Lett.*, 104:253003, Jun 2010.

[40] J. J. Sakurai. *Modern Quantum Mechanics (Revised Edition).* Addison Wesley, 1993.

[41] Stefan Schmid, Arne Härter, and Johannes Hecker Denschlag. Dynamics of a cold trapped ion in a bose-einstein condensate. *Phys. Rev. Lett.*, 105:133202, Sep 2010.

[42] Stefan Schmid, Arne Härter, Albert Frisch, Sascha Hoinka, and Johannes Hecker Denschlag. An apparatus for immersing trapped ions into an ultracold gas of neutral atoms. *Review of Scientific Instruments*, 83(5):053108, 2012.

[43] R. Shankar. *Principles of Quantum Mechanics, 2nd Edition.* Plenum Press, 1994.

[44] E. Simon, P. Laurent, and A. Clairon. Measurement of the stark shift of the cs hyperfine splitting in an atomic fountain. *Phys. Rev. A*, 57:436–439, Jan 1998.

[45] L. Sirovich and M. Kirby. Low-dimensional procedure for the characterization of human faces. *J. Opt. Soc. Am. A*, 4(3):519–524, Mar 1987.

[46] T Stace, A N Luiten, and R P Kovacich. Laser offset-frequency locking using a frequency-to-voltage converter. *Measurement Science and Technology*, 9(9):1635, 1998.

[47] Daniel A. Steck. Rubidium 87 d line data. *available online at "http://steck.us/alkalidata" (revision 2.0.1 2 May 2008)*, 2008.

[48] Atsushi Takahashi, Hiromitsu Imai, Kazuya Numazaki, and Atsuo Morinaga. Phase shift of an adiabatic rotating magnetic field in ramsey atom interferometry for $m = 0$ sodium-atom spin states. *Phys. Rev. A*, 80:050102, Nov 2009.

[49] T. Takekoshi, J. R. Yeh, and R. J. Knize. Quasi-electrostatic trap for neutral atoms. *Optics Communications*, 114(5-6):421 – 424, 1995.

[50] S. Ulzega, A. Hofer, P. Moroshkin, and A. Weis. Reconciliation of experimental and theoretical electric tensor polarizabilities of the cesium ground state. *EPL (Europhysics Letters)*, 76(6):1074, 2006.

[51] Simone Ulzega. *Theoretical and experimental study of the Stark effect in the ground state of alkali atoms in helium crystals*. PhD thesis, Université de Fribourg, 2006.

[52] Christoph Zipkes, Stefan Palzer, Carlo Sias, and Michael Köhl. A trapped single ion inside a bose-einstein condensate. *Nature*, 464(7287):388–391, March 2010.

[53] Christoph Zipkes, Lothar Ratschbacher, Carlo Sias, and Michael Köhl. Kinetics of a single trapped ion in an ultracold buffer gas. *New Journal of Physics*, 13(5):053020, 2011.